Title

The source of infrasound associated with long-period events at Mount St. Helens

Journal

Journal of Geophysical Research, 114(B4)

ISSN

0148-0227

Authors

Matoza, Robin S

Garcés, Milton A

Chouet, Bernard A

et al.

Publication Date

2009-04-24

DOI

10.1029/2008JB006128

Peer reviewed

JOURNAL OF GEOPHYSICAL RESEARCH, VOL. 114, B04305, doi:10.1029/2008JB006128, 2009

The source of infrasound associated with long-period events at Mount St. Helens

Robin S. Matoza,[1] Milton A. Garcés,[2] Bernard A. Chouet,[3] Luca D'Auria,[4] Michael A. H. Hedlin,[1] Catherine De Groot-Hedlin,[1] and Gregory P. Waite,[3,5]

Received 30 September 2008; revised 28 January 2009; accepted 16 February 2009; published 24 April 2009.

[1] During the early stages of the 2004–2008 Mount St. Helens eruption, the source process that produced a sustained sequence of repetitive long-period (LP) seismic events also produced impulsive broadband infrasonic signals in the atmosphere. To assess whether the signals could be generated simply by seismic-acoustic coupling from the shallow LP events, we perform finite difference simulation of the seismo-acoustic wavefield using a single numerical scheme for the elastic ground and atmosphere. The effects of topography, velocity structure, wind, and source configuration are considered. The simulations show that a shallow source buried in a homogeneous elastic solid produces a complex wave train in the atmosphere consisting of *P*/*SV* and Rayleigh wave energy converted locally along the propagation path, and acoustic energy originating from the source epicenter. Although the horizontal acoustic velocity of the latter is consistent with our data, the modeled amplitude ratios of pressure to vertical seismic velocity are too low in comparison with observations, and the characteristic differences in seismic and acoustic waveforms and spectra cannot be reproduced from a common point source. The observations therefore require a more complex source process in which the infrasonic signals are a record of only the broadband pressure excitation mechanism of the seismic LP events. The observations and numerical results can be explained by a model involving the repeated rapid pressure loss from a hydrothermal crack by venting into a shallow layer of loosely consolidated, highly permeable material. Heating by magmatic activity causes pressure to rise, periodically reaching the pressure threshold for rupture of the "valve" sealing the crack. Sudden opening of the valve generates the broadband infrasonic signal and simultaneously triggers the collapse of the crack, initiating resonance of the remaining fluid. Subtle waveform and amplitude variability of the infrasonic signals as recorded at an array 13.4 km to the NW of the volcano are attributed primarily to atmospheric boundary layer propagation effects, superimposed upon amplitude changes at the source.

Citation: Matoza, R. S., M. A. Garcés, B. A. Chouet, L. D'Auria, M. A. H. Hedlin, C. De Groot-Hedlin, and G. P. Waite (2009), The source of infrasound associated with long-period events at Mount St. Helens, *J. Geophys. Res.*, *114*, B04305, doi:10.1029/2008JB006128.

1. Introduction

[2] Shallow (<2 km) long-period (0.5–5 Hz) seismicity at volcanoes, including individual long-period (LP) events and tremor, is often attributed to the activity of magmatic and hydrothermal fluids in subsurface conduits and cracks [e.g., *Chouet*, 1985, 1988, 1992; *Garcés*, 1997; *Neuberg et al.*, 2000; *Kumagai et al.*, 2005]. LP events are transient, volumetric signals, with a broadband onset lasting ~10 s, followed by a decaying harmonic coda lasting tens of seconds to a few minutes and containing pronounced spectral peaks that are independent of azimuth and distance to the source [*Chouet*, 1996a]. This is usually interpreted as a broadband pressure excitation mechanism, followed by the resonant response of a fluid-filled cavity. Although the fluid response is understood quantitatively in terms of solid-fluid interface waves or "crack waves" [*Chouet*, 1986, 1988; *Ferrazzini and Aki*, 1987], the physics of the driving mechanism initiating LP resonance remains a major challenge [*Chouet*, 2003].

[3] The 2004–2008 eruption at Mount St. Helens was accompanied by a sustained sequence of shallow, repetitive

[1]Laboratory for Atmospheric Acoustics, Institute of Geophysics and Planetary Physics, Scripps Institution of Oceanography, University of California, San Diego, La Jolla, California, USA.
[2]Infrasound Laboratory, Hawai'i Institute of Geophysics and Planetology, University of Hawai'i at Manoa, Kailua-Kona, Hawaii, USA.
[3]U.S. Geological Survey, Menlo Park, California, USA.
[4]Istituto Nazionale di Geofisica e Vulcanologia, Osservatorio Vesuviano, Naples, Italy.
[5]Now at Department of Geological and Mining Engineering and Sciences, Michigan Technological University, Houghton, Michigan, USA.

0148-0227/09/2008JB006128$09.00

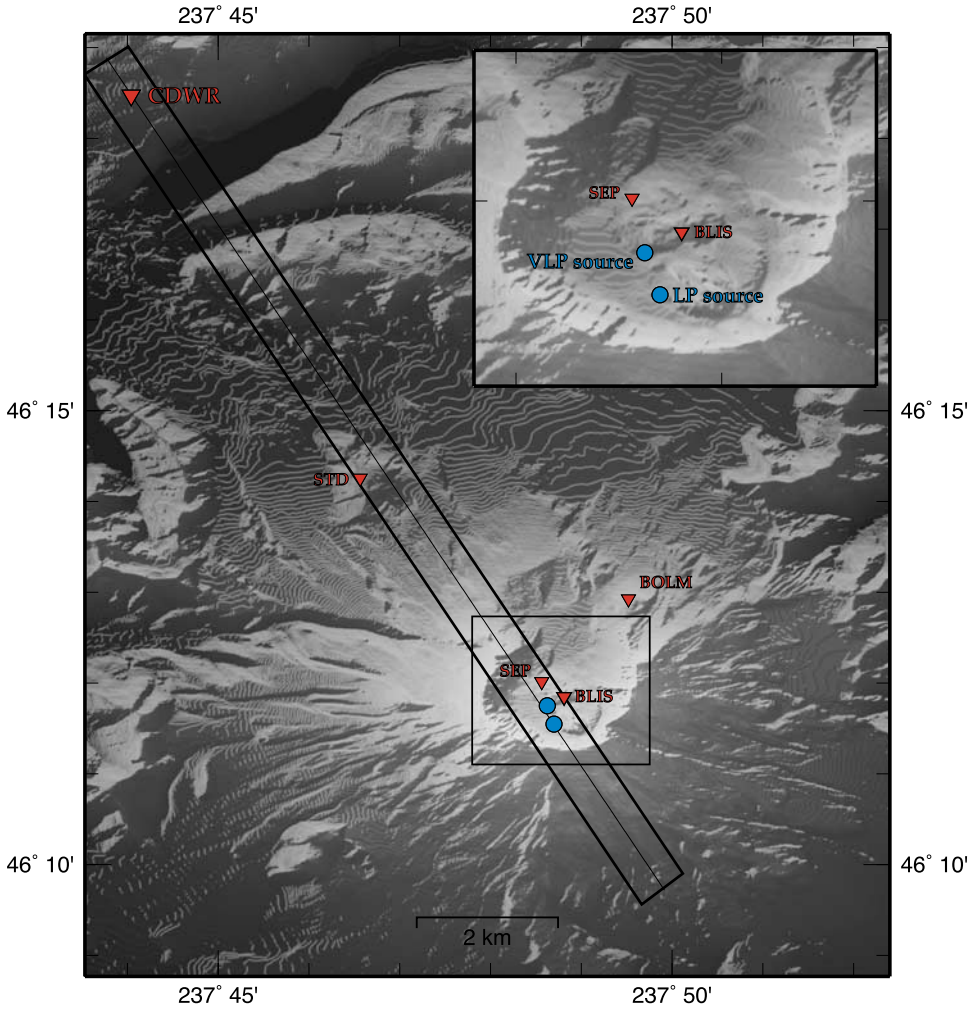

Figure 1. Location of CDWR, in a forest 13.4 km to the NW of Mount St. Helens (MSH). Microphones operated by CVO (BLIS, SEP, BOLM, STD) are also shown. The long box trending NW is 750 m wide, and represents the region of the 2.5-D FD calculations described in section 4. The line down the center of this box intersects the LP source location and CDWR and represents the profile used in the 2-D FD simulations. The box centered on the MSH crater indicates the area of the inset, which shows the LP and VLP point source locations obtained by *Waite et al.* [2008]. The topography data in the crater are from 19 April 2005 [*Schilling et al.*, 2009].

LP events that were also named "drumbeats" owing to their precise regularity and high degree of waveform similarity [*Moran et al.*, 2009a]. Although initially ascribed to stick-slip motion along the margins of the solid lava extrusion [*Iverson et al.*, 2006; *Harrington and Brodsky*, 2007], these earthquakes were shown to have all-dilatational first motions where distinguishable, common spectral peaks observed on multiple stations, long-duration oscillatory source time functions, and a volumetric moment tensor, which are all characteristic of LP events [*Waite et al.*, 2008]. The moment tensor inversions of a subset of these LP events were found consistent with a subhorizontal, steam-filled crack located at the elevation of the old 1980s crater floor and directly below the new lava dome (Figure 1). Inversion of very long period (VLP) events that accompanied some of the LPs also pointed to reaction forces in a dike-sill composite located ~400 m to the NW of the LP source (underneath the old 1980s lava dome), and ~250 m deeper [*Waite et al.*, 2008]. *Waite et al.* [2008] proposed that the LP source may consist of a shallow hydrothermal crack, filled with a mixture of meteoric and juvenile steam, and pressurized by the magmatic activity. Periodically, pressure is lost, causing the crack to partially collapse and resonate (LP events), and triggering a response in the magmatic system (VLP events).

[4] In addition, *Matoza et al.* [2007] reported infrasound signals (acoustic waves <20 Hz) associated with LP events at Mount St. Helens during November 2004 to March 2005, radiating away from the volcano through the atmosphere at acoustic velocity. Whenever present, the infrasonic LP events were more impulsive than the seismic LP events and lacked a prominent long-period coda. It was also observed that not all seismic LP events had a clear infrasonic arrival because the infrasonic signal amplitude faded in and out over timescales of hours to days without a change in the background noise levels.

[5] In this study, we attempt to understand (1) the source process generating the infrasonic signals and (2) the intermittency of the infrasonic signals. Since the seismic and infrasonic signals from LP events are sourced simultaneously, an understanding of the first point would yield additional information on the source process of seismic LP events. The simplest explanation for the infrasonic signals is that they are sourced by seismic-acoustic conversion at the ground-air interface. It is known that infrasound and acoustic gravity waves are generated by large tectonic earthquakes both from strong ground displacement and deformation near the source epicenter [e.g., *Bolt*, 1964; *Mikumo*, 1968], and interaction of surface waves with topography [*Le Pichon et al.*, 2002, 2003, 2006; *Mutschlecner and Whitaker*, 2005, and references therein]. In addition, *P*/*SV* and Rayleigh wave energy can be locally radiated into the atmosphere for even relatively small magnitude earthquakes [e.g., *Press and Ewing*, 1951; *Kitov et al.*, 1997; *Mutschlecner and Whitaker*, 2005; *Sylvander et al.*, 2007], providing an explanation for reports of low-frequency sounds accompanying earthquakes [*Benioff et al.*, 1951]. Seismic-acoustic conversion is expected for LPs at Mount St. Helens because the source is very shallow ($\sim$200 m below the topography surface used in the moment tensor inversion), extended horizontally, and consists of a moment tensor with diagonal elements in the ratio M_{xx}:M_{yy}:M_{zz} $\sim$ 1:1:3 [*Waite et al.*, 2008], which propagates proportionally more energy vertically than horizontally. Furthermore, *Waite et al.* [2008] imaged a strong ($\sim$9 GN) oscillatory vertical single-force component (F_z) to the LP source. This was attributed to the vertical elastic oscillations of the rock mass perched above the crack, and could be a significant source of acoustic energy by analogy with a piston.

[6] However, if these elastodynamic processes cannot explain the observed infrasonic signals, other mechanisms may be invoked for the source. The "trigger" [*Chouet*, 1985], or pressure excitation mechanism initiating LP resonance, may be propagated directly into the atmosphere through shallow porous material, or a secondary process such as rapid gas release from the LP source may generate the acoustic signals [*Matoza et al.*, 2007].

[7] When infrasound has been observed in relation to LP events at other volcanoes [*Iguchi and Ishihara*, 1990; *Yamasato*, 1998; *Garcés et al.*, 1999; *Petersen and McNutt*, 2007], it has typically been attributed to gas release. *Yamasato* [1998] analyzed impulsive infrasonic signals associated with hybrid long-period events (LPs with mixed first motions and pronounced broadband onsets [*Lahr et al.*, 1994]) at Unzen Volcano, Japan. The observed infrasonic amplitude could not be explained by a simple volume change (acoustic monopole source) due to ground displacement above the seismic source, so it was concluded that the infrasound was generated by the emission of volcanic gas during seismic rupture and fracture of the gas-charged lava dome material. *Petersen and McNutt,* [2007] also observed impulsive infrasonic signals associated with LP events at Shishaldin Volcano, Alaska. In this case, the seismo-acoustic events were correlated with visual observations of discrete "gas puffing" from the open-conduit system, so were attributed to degassing explosions in a shallow hydrothermal conduit system.

[8] Before invoking such a mechanism for LPs at Mount St. Helens, we investigate whether seismic-acoustic conversion can produce the observed amplitude ratio of acoustic pressure to seismic vertical velocity (P/V_z) and replicate the general characteristics of the observed waveforms and spectra. Since influence from strong topographic heterogeneity is unavoidable in volcanic settings [*Ohminato and Chouet*, 1997; *Neuberg and Pointer*, 2000], we use a 3-D staggered grid finite differences representation of the velocity-stress elastodynamics equations, which allows for heterogeneous medium properties, arbitrary moment tensor and single-force sources with an arbitrary source time function, and implicit modeling of wave propagation across solid-fluid boundaries without the use of explicit boundary conditions [*D'Auria and Martini*, 2007].

[9] Interpretation of the infrasound source mechanism is further complicated by the intermittency of the signals (2, above). This intermittency may be caused by acoustic propagation effects in a time-varying atmosphere, and/or time-varying source effects. To gain more understanding of the relative contributions from these effects, we consider infrasonic propagation in a time-varying atmosphere at the range of interest (13.4 km) using ray tracing and finite difference methods. We also track the observed time evolution of both seismic and infrasonic waveforms using waveform cross correlation, providing additional insights into source and propagation effects.

2. Data

[10] *Matoza et al.* [2007] describe the broadband infrasound array deployment at Mount St. Helens (MSH). In this study, we use data from the Coldwater (CDWR) array located in a forest 13.4 km to the NW of the volcano, with direct line of sight to the open crater (Figure 1). This array consisted of four DASE/Tekelec MB2000 broadband aneroid microbarometers (flat response 0.01–17 Hz with antialiasing filter) arranged in a centered triangle with an aperture of $\sim$100 m. Four 15 m porous hoses were attached to each microbarometer for spatial wind filtering [*Hedlin et al.*, 2003]. The central element was collocated with a Güralp CMG-40T broadband seismometer (0.033–17 Hz with antialiasing filter) and a weather station (wind speed, direction, and temperature). The data were digitized at 40 Hz using a 24-bit Nanometrics Polaris Trident digitizer, and transmitted to the Geological Survey of Canada, Ottawa using a VSAT antenna. The array configuration permits evaluation of wavefront properties of recorded signals. Azimuth is used to discriminate between signals of interest and coherent background noise, while horizontal velocity is used to separate infrasonic signals from coseismic shaking.

[11] The U.S. Geological Survey Cascades Volcano Observatory (CVO) also operated a network of short-period (1 Hz) infrasonic microphones at distances of 400 m to 4 km from the LP source region (BLIS, SEP, BOLM, STD; Figure 1), with some overlap in data coverage with the CDWR array [*McChesney et al.*, 2009; *Moran et al.*, 2009b]. Noise conditions at these wind-exposed sites and strong coseismic shaking hinder unambiguous identification of infrasonic LP events in these data. Nevertheless, infrasound signals associated with M_d 2 – 3 earthquakes were

recorded at STD during the vent-clearing phase prior to 5 October 2004 [*Moran et al.*, 2009b], and impulsive signals resembling the infrasonic LP events observed at CDWR were recorded at BLIS in November 2004. However, BLIS was deployed on a "spider" platform [*McChesney et al.*, 2009] prone to coseismic shaking, and the signals were not recorded at the other microphone stations due to noise conditions, so care must be taken to identify these as true infrasonic signals (S. C. Moran, CVO, personal communication, 2006). The STD microphone telemetry was disconnected on 12 October 2004 [*McChesney et al.*, 2009].

2.1. Observations at CDWR

[12] Infrasonic signals associated with LP events were observed intermittently at CDWR throughout the time period 1 November 2004 to 27 March 2005 (first CDWR deployment), and much less frequently from 13 August 2005 to 8 July 2008 (second CDWR deployment). The time periods with the clearest, largest signal-to-noise ratio events were November 2004 and late February to March 2005. These time periods correspond to the largest seismic amplitudes during the CDWR data coverage [*Moran et al.*, 2009a], indicating that clear observation of the infrasonic signals depends to a first order on a seismic amplitude "threshold" (see section 3). CDWR was deployed at a range optimized for large amplitude eruption signals. Since infrasonic LP events are relatively weak signals, it is not surprising that only the largest amplitude examples are clearly detected above noise.

2.1.1. Waveforms

[13] When the infrasonic signals were clearly observed, their waveform and spectral features were distinct from those of the seismic signals. Figure 2 shows the waveforms for a typical LP event recorded by CDWR at 0818:35 UTC, 4 March 2005. An acoustic signal is seen to arrive ~38 s after the onset of the seismic signal, consistent with the 13.4 km source-receiver range. No coincident seismo-acoustic arrival is observed in the infrasonic pressure data (also true when beam forming at seismic velocity), indicating that local seismic-acoustic conversion [*Press and Ewing*, 1951] or mechanical sensitivity of the MB2000 sensor is not significant in this study. When filtered in the band 1–15 Hz, the infrasonic waveforms have duration ~10 s, with the dominant portion of energy lasting ~5 s. This duration corresponds to the duration of the broadband pressure excitation mechanism or LP "trigger" observed in the seismic records. After 5 s, the infrasonic amplitudes decay rapidly, while in the seismic records the resonant oscillations of the crack become increasingly dominant. This is further exemplified by considering data filtered at 5–15 Hz, which effectively filters out the crack resonance signature from the seismic data and leaves only the higher frequency components of the broadband trigger. In this band, the seismic and acoustic waveforms have the same duration. We also note that (1) the seismic first motion is dilatational, consistent with the work by *Waite et al.* [2008], and (2) the infrasound signal is apparently seen in the 5–15 Hz filtered seismic record, which may represent shaking of the seismic sensor by the passing infrasonic wave or local air-ground coupling. While dispersion may add to the length of the seismic waveform at this range (see section 4.2.1), a long-duration source time function (>20 s [*Waite et al.*, 2008]) is required to produce such a long-duration seismic signal. The observed waveform differences require a mechanism to separate the trigger and resonance components at the source (sections 5 and 7.1).

[14] The waveforms in Figure 2 are shown with normalized amplitudes.[1] In Figure S1, the same waveforms are shown with their correct amplitudes. Figure S1 illustrates that the 5–15 Hz infrasonic waveforms have amplitudes lower by a factor of ~3 than the 1–15 Hz filtered infrasonic waveforms, demonstrating that the majority of energy in the impulsive infrasonic signals is in the 1–5 Hz band. This is the same band in which the seismic signals have the majority of their energy, and indicates that the observed differences in waveform cannot be attributed simply to a difference in frequency content and attenuation effects (see sections 5 and 7.1).

2.1.2. Power Spectra

[15] Figure 3 shows power spectral density (PSD) estimates for infrasonic and seismic LPs. Only seismic LPs with a clear infrasonic arrival were included. Infrasound array data were beam formed at an azimuth of 153° and speed of 330 m/s using a conventional time delay (time domain) beam former, with the array gain due to beamforming set to 1.0 [*DeFatta et al.*, 1988]. The PSD estimates were formed by picking 1116 events on 11 November 2004 and 432 events on 4 March 2005 with a short-term average/long-term average (STA/LTA) detector (STA length, 3 s; LTA length, 10 s; STA/LTA ratio for detection, 2.0), isolating a 12 s window of unfiltered data around the pick (1 s pretrigger, 11 s posttrigger), and estimating the power spectrum of each using a multitaper method [*Riedel and Sidorenko*, 1995] (implemented in program PSD provided by R. L. Parker, IGPP, SIO). This method applies frequency-dependent minimization of the sum of variance and bias, making it particularly suitable for spectra with sharp peaks, such as LP resonance spectra. The same spectral parameters were used for infrasonic and seismic data, chosen to smooth the spectra and show only the grossest details. The individual event spectra were progressively stacked, emphasizing the repeatable spectral features, and reducing the influence of random noise. A transfer function was then obtained by dividing the final seismic stack by the infrasonic stack, which serves to illustrate the differences between the two spectra.

[16] The infrasonic signals have a relatively flat spectrum in the 1–5 Hz band, with noise from the ocean dominating below ~1 Hz [*Matoza et al.*, 2007]. The seismic signals have significant spectral peaks in the 1–5 Hz band, broadly consistent with the work by *Waite et al.* [2008]. The 11 November 2004 data have a dominant peak at 1.4 Hz, while the 4 March 2005 data have a dominant peak at 1.7 Hz (compare with *Waite et al.* [2008], who also observed a dominant peak at 1.7 Hz on multiple stations for events on 22 July 2005). Such a change over a timescale of months is expected for spectral features of the source process, but not for those due to propagation effects. The transfer functions for both November 2004 and March 2005 further indicate that the seismic data are enriched in the resonant oscillation signature of the crack, while the infrasonic data are not. The

[1] Auxiliary materials are available in the HTML. doi:10.1029/2008JB006128.

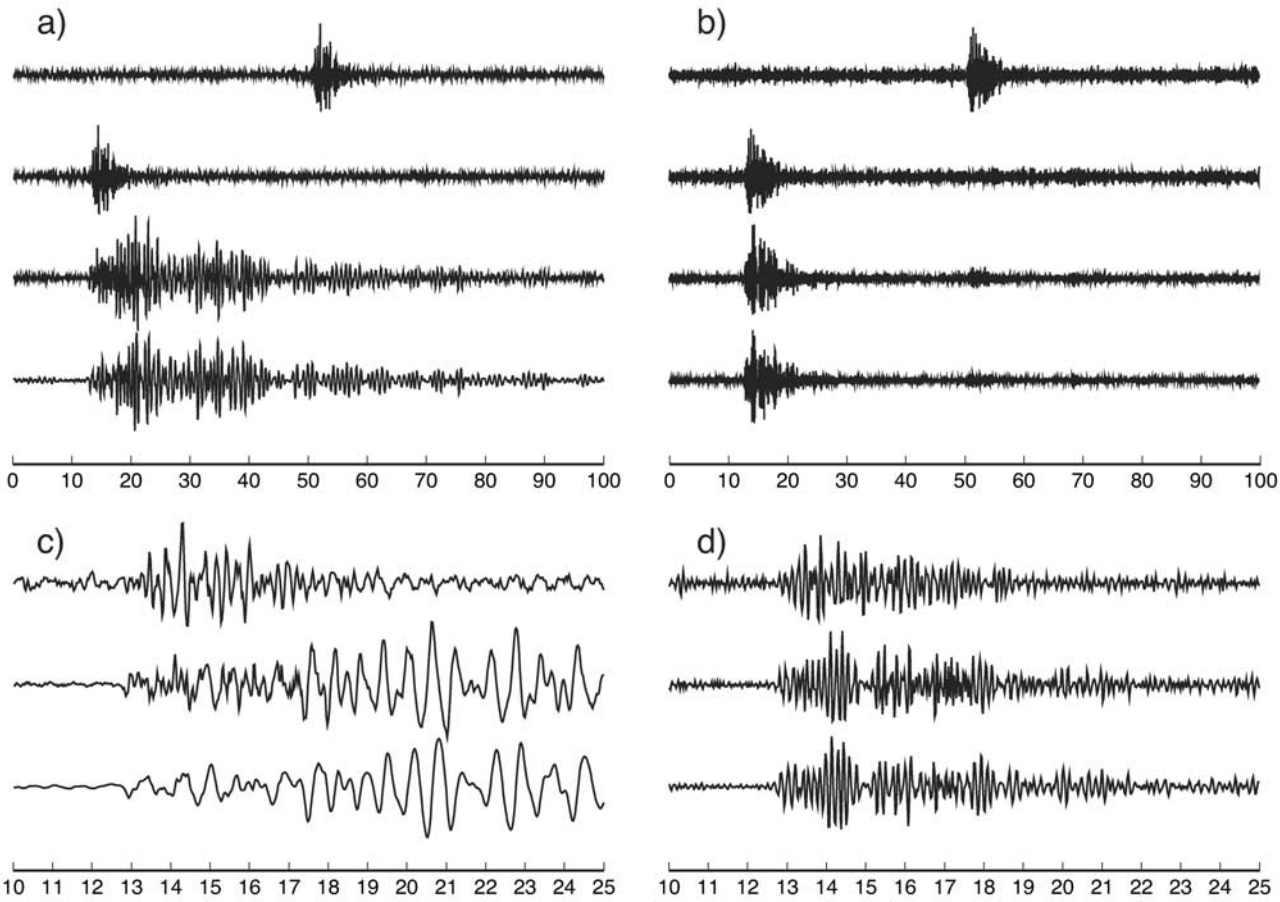

Figure 2. Infrasonic and seismic waveforms at CDWR for an LP event with high SNR. Origin time of plot is 0818:35 UTC, 4 March 2005, time in seconds. (a) All signals filtered 1–15 Hz, from top to bottom: (1) infrasonic beam (azimuth 153°, speed 330 m/s), (2) infrasonic beam time advanced by 38 s, (3) vertical seismic velocity, and (4) vertical seismic displacement (integrated velocity). (c) Lower three traces in Figure 2a expanded to show time from 10 to 25 s. (b and d) same as Figures 2a and 2c but filtered 5–15 Hz. Note the following features: (1) no coincident seismo-acoustic arrival observed in the infrasound data of upper trace in Figure 2a, (2) in band 1–15 Hz, infrasonic signal has the same duration as the broadband trigger onset in seismic LP event (Figure 2c), (3) in band 1–15 Hz, at ~17 s, infrasonic amplitude is decaying into noise while resonant oscillations of the crack are becoming dominant in seismic record (Figure 2c), (4) dilatational first motion observed in seismic displacement (Figure 2c), consistent with that of *Waite et al.* [2008], (5) in band 5–15 Hz, infrasonic and seismic waveforms have similar duration (Figures 2b and 2d), and (6) air-ground coupled energy observed in seismic data at ~50 s in Figure 2b. The waveforms have normalized amplitudes; see Figure S1 for the waveforms shown at their correct amplitudes.

roll-off at higher frequencies (>3 Hz) is more pronounced in the seismic data than infrasonic data, emphasizing that the infrasonic data may be more representative of the broadband trigger signal. This may also relate to frequency-dependent anelastic attenuation and scattering, which is more severe for seismic energy in the volcanic edifice than in the air [*Thelen et al.*, 2009; *Sutherland and Bass*, 2004].

2.1.3. Amplitudes

[17] Since the amplitudes of infrasonic LPs observed at CDWR vary significantly, we consider the distribution of infrasonic to vertical seismic amplitude (P/V_z) ratios for a

Figure 3. Power spectrum estimates for infrasonic and seismic LPs observed at CDWR on 11 November 2004 and 4 March 2005. Events were picked with an STA/LTA detector, and a multitaper method applied to a 12 s window surrounding the pick (1 s pretrigger, 11 s posttrigger). The spectra for the individual events were then progressively stacked (thick red line shows final stack). (a) The 1116 infrasonic LP events on 11 November 2004. (b) Vertical component seismic LP events corresponding to infrasonic events in Figure 3a. (c) Transfer function formed by dividing final seismic spectrum stack (Figure 3b) by final infrasonic spectrum stack (Figure 3a). (d–f) Same as Figures 3a–3c but for 432 events on 4 March 2005. The energy below ~1.2 Hz in Figures 3a and 3d and below ~0.5 Hz in Figures 3b and 3e is ambient noise, and not LP signal.

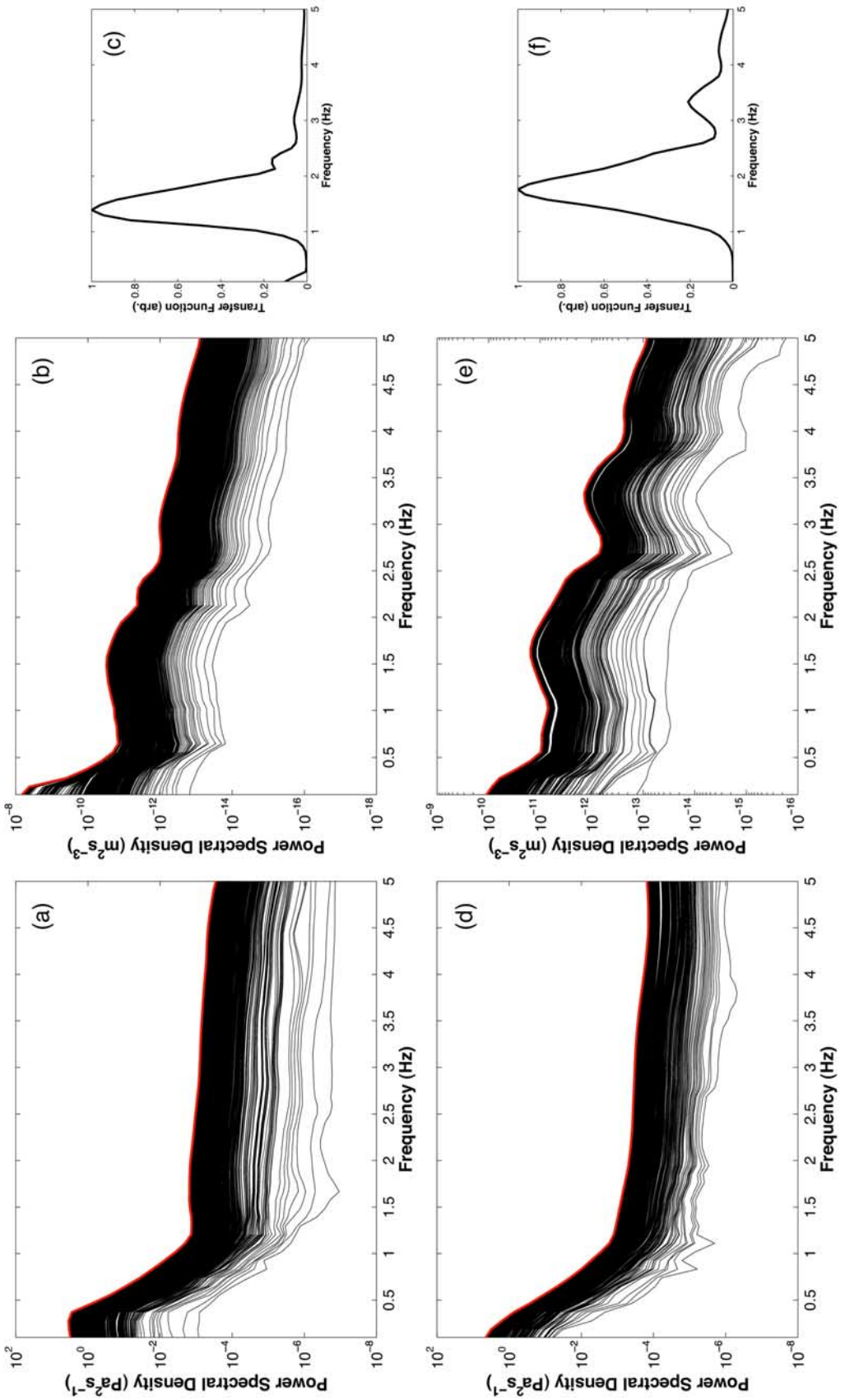
(a)
(b)
(c)
(d)
(e)
(f)
Power Spectral Density (Pa²s⁻¹)
Power Spectral Density (m²s⁻³)
Transfer Function (arb.)
Frequency (Hz)

Figure 3

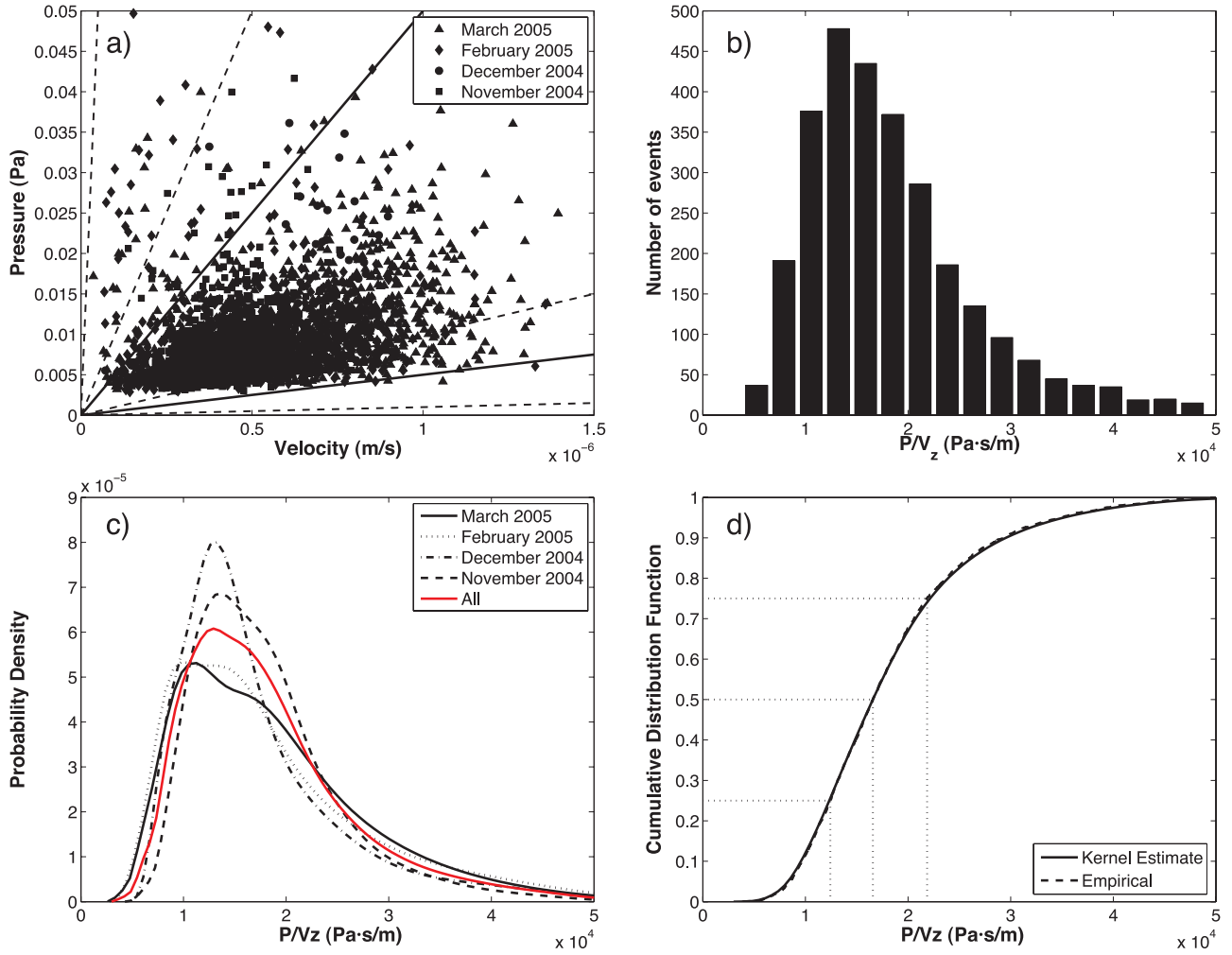

Figure 4. A comparison of infrasonic and seismic amplitudes for 2963 LP events observed during 1–16 November 2004, 16 December 2004, 1–10 and 24–28 February 2005, and 1–19 March 2005. (a) Scatterplot of infrasonic amplitude (Pa) versus vertical seismic amplitude (m/s). Dashed lines correspond to constant values of P/V_z, clockwise from top, 10^6, 10^5, 10^4, 10^3 Pa s/m. The vast majority of events have P/V_z between 5×10^3 and 5×10^4 Pa s/m (solid lines). (b) Histogram of P/V_z values for data shown in Figure 4a. Long tail of events with $P/V_z > 5 \times 10^4$ Pa s/m not shown. Note the unimodal distribution with a peak at 1.3×10^4 Pa s/m. (c) (Gaussian) kernel density estimate of the probability density function of P/V_z for the different time periods. (d) Kernel estimate and empirical cumulative distribution functions for all data. The median is: 1.7×10^4 Pa s/m, and the interquartile range is 9.4×10^3 Pa s/m.

large number of events sampling a wide range of atmospheric conditions. Figure 4a shows a scatterplot of peak infrasonic pressure amplitude (P) versus peak vertical seismic velocity amplitudes (V_z) for 2963 LP events from 1 to 16 November 2004, 16 December 2004, 1–10 and 24–28 February 2005, and 1–19 March 2005. The unit-gain beam-formed data were filtered at 2–4 Hz (found to be an optimal band for picking), and events were picked using the STA/LTA detector described in section 2.1.2. Subsequently, the beamed data were refiltered at 1–5 Hz, and the maximum absolute amplitude in a 20 s window following the pick was assigned to each event. Since the maximum seismic amplitude does not coincide with the time delayed maximum infrasonic amplitude but appears later in the waveform during the resonance coda (Figure 2), the P/V_z we measure should be considered a lower bound. In order to exclude spurious picks not associated with LP events at MSH, only events consisting of a seismic pick followed by an infrasonic pick 38 ± 4 s later were included. However, for the large quantity of data considered, picks related to transient noise occasionally match the selection criteria. This is responsible for the small number of detections with $P/V_z > 10^5$ Pa s/m. However, compared to the number of detections associated with LP events, these occurrences are insignificant.

[18] Figure 4a demonstrates that the vast majority of events have P/V_z between 5×10^3 and 5×10^4 Pa s/m. Figure 4b shows a histogram of P/V_z ratios for the events shown in Figure 4a, better illustrating the distribution of values. A smoother estimate of the underlying probability density function (PDF) was obtained using a kernel density estimator with a Gaussian kernel (Figure 4c). The PDF has a

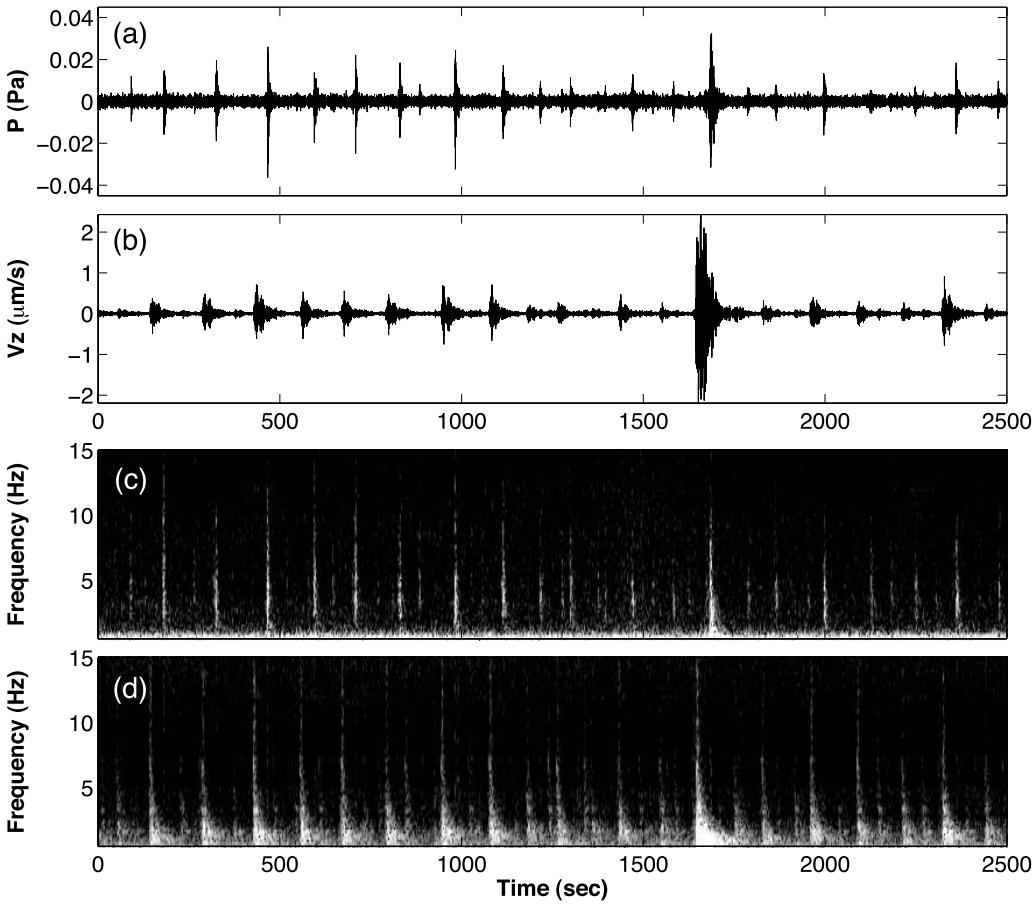

Figure 5. A sequence of LPs punctuated by a larger $M_d > 2$ seismic event observed at CDWR. The larger event is also accompanied by an impulsive infrasound signal. Origin time of plot is 0811:40 UTC, 4 March 2005. (a) Beam-formed CDWR infrasound data (azimuth 153°, speed 330 m/s, filtered 1–5 Hz). (b) CDWR vertical seismic data filtered 1–5 Hz. (c) Spectrogram of unfiltered infrasonic beam. (d) Spectrogram of unfiltered vertical seismic data. The large seismic event at 1645 s has an amplitude 2.4 times greater than the next largest event in the sequence, while the infrasonic arrival has an amplitude comparable to the preceding events. However, the P/V_z ratio varies only between 2.0×10^4 and 5.3×10^4 Pa s/m, consistent with the variability shown in Figure 4. Note in the spectrograms how the seismic events contain a long-duration resonant coda, while the infrasonic events consist of a short-lived broadband impulse.

long tail at high values and a shorter tail at lower values, likely caused by the artifact of the infrasonic amplitudes falling below the detection threshold of the STA/LTA detector. However, we note that the P/V_z values form a unimodal distribution with a maximum at 1.3×10^4 Pa s/m (Figure 4c). We take this mode as the P/V_z ratio that would be observed under "average" atmospheric conditions for which infrasonic signals associated with seismic LPs are detected. The mode differs from the median (1.7×10^4 Pa s/m) by a negligible amount (Figure 4d). We attribute the spread in values about this peak dominantly to random dynamic atmospheric propagation effects, i.e., random variations in the wind, temperature, and sound speed profiles, and scattering from atmospheric turbulence [*Bass*, 1991]. However, it remains possible that part of this spread is attributable to variable seismic-acoustic energy partitioning at the source (see section 7). Regardless of the physical cause of spread, a P/V_z of 1.3×10^4 Pa s/m at 13.4 km range is taken as the target in modeling the elastodynamic seismic-acoustic coupling for a static atmosphere (section 4).

2.1.4. Larger ($M_d > 2$) Events

[19] The sustained LP sequence at MSH has occasionally been punctuated by events with larger magnitude ($M_d > 2.0$) that often caused rockfalls and subsequent ash plumes rising above the crater rim [*Moran et al.*, 2009a]. These events have similar spectral content to the ordinary LPs, but in general have dissimilar waveforms [*Moran et al.*, 2009a; *Waite et al.*, 2008], so their relationship to the ordinary LPs is unclear. Here we show that, like the typical LP events, these larger events also produce infrasound. Figure 5 shows a sequence of LP events from 4 March 2005, which contains one event with much larger seismic amplitude (2.2 μm/s) than the others. The infrasound signal corresponding to this event has an amplitude of 32 mPa, comparable to some of the events seen earlier in the sequence. However, we note that for the time period shown, P/V_z varies between 2.0×10^4 Pa s/m (for the larger event)

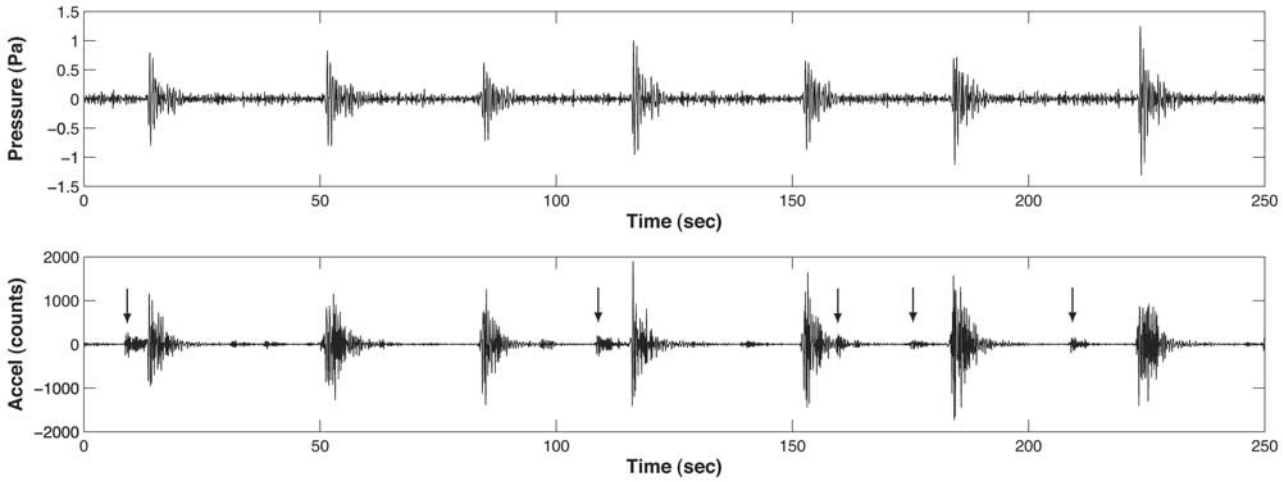

Figure 6. Waveforms (filtered 1–5 Hz) observed on the BLIS spider platform ~400 m from the LP source (origin time of plot is 1912:30 UTC, 11 November 2004). Impulsive signals appear in the microphone data approximately coincident with each typical LP event. However, smaller seismic events (some indicated by arrows) do not appear on the microphone channel, suggesting that coseismic shaking of the microphones is not significant. The lack of long-period coda for LP events in the accelerometer record is a result of instrument response.

and 5.3×10^5 Pa s/m, consistent with the variability illustrated in Figure 4 and discussed above. Like the infrasound from other LPs, the infrasonic signal from the larger event is impulsive, and lacks a prominent coda. This suggests that the larger events and ordinary LPs have a similar source mechanism.

2.2. Observations at BLIS

[20] The instruments deployed at station BLIS (Figure 1) consisted of an accelerometer and an 18-element electret infrasonic microphone deployed on a "spider" platform [*McChesney et al.*, 2009]. The predicted seismic-acoustic time delay at BLIS (400 m from LP source, Figure 1) is too short to provide clear separation of an acoustic arrival versus coseismic shaking. In addition, infrasound associated with LPs was not recorded at SEP or BOLM due to site noise conditions.

[21] However, Figure 6 shows data from the microphone and accelerometer at BLIS. The typical seismic LPs have coincident infrasonic signals. The amplitudes of these signals (~0.8 Pa at 400 m), and the amplitudes at CDWR (~0.01 Pa at 13.4 km) for the same time period, are broadly consistent with acoustic spherical spreading (amplitude $\sim 1/r$). In addition, small events are recorded on the seismic channel that are not mimicked in the acoustic record. These smaller events are recorded at other times, such as during the 8 March 2005 phreatic explosion [*Matoza et al.*, 2007] and do not occur with a constant delay time in relation to the typical LP events. Instead, the smaller events appear to be part of a separate random process loosely coupled to the LP generation (unlike at other volcanoes where the small event may be considered a coupled precursor with more consistent time delay [e.g., *Gil Cruz and Chouet*, 1997; *Caplan-Auerbach and Petersen*, 2005]). If each typical LP corresponds to the sudden loss of pressure and collapse in a hydrothermal crack, these smaller events may be related to the recharge of fluid pressure, or the fine-scale adjustments in the hydrothermal system in response to this sudden disturbance of the hydraulic pressure. The disruption of hydraulic pressure may induce cavitation inception [*Leighton*, 1994], perhaps producing signals via bubble collapse similar to those produced by hydrothermal boiling [*Leet*, 1988].

[22] Assuming a linear scaling between recorded apparent pressure and amplitude of microphone shaking, the small events should appear with amplitudes above noise on the acoustic channel. This suggests that microphone shaking is not significant, and the BLIS microphone was recording "true" infrasonic signals for the LPs like those recorded at CDWR. However, the possibility remains that an amplitude threshold for ground shaking is required to induce apparent signals on the microphones.

[23] Given the ambiguity associated with these data, we do not attempt a detailed data analysis. However, we determined amplitudes for 4811 LP events during 7–13 November 2004 using the method described in section 2.1.3. Acceleration data were integrated to velocity, both P and V_z data filtered at 1–3 Hz, and the nominal calibration values for 2 Hz applied. Only detections consisting of a seismic detection and an infrasonic detection ±2 s were included. At BLIS, P is clearly linearly related to V_z, with a modal P/V_z ratio of 5.3×10^3 Pa s/m in the 1–3 Hz band (Figure S2). Furthermore, the infrasonic LPs were continuously observed during this time at BLIS, with both infrasonic and seismic amplitudes gradually increasing in proportion such that the amplitude ratio remained relatively constant. This indicates that the amplitude variations at CDWR are related to atmospheric effects superimposed upon changes in the amplitude at the source. BLIS was destroyed in January 2005, so direct comparisons cannot be made for March 2005.

3. Waveform Cross Correlation

[24] Waveform cross correlation at a single station has been used previously on sequences of seismic LP events to

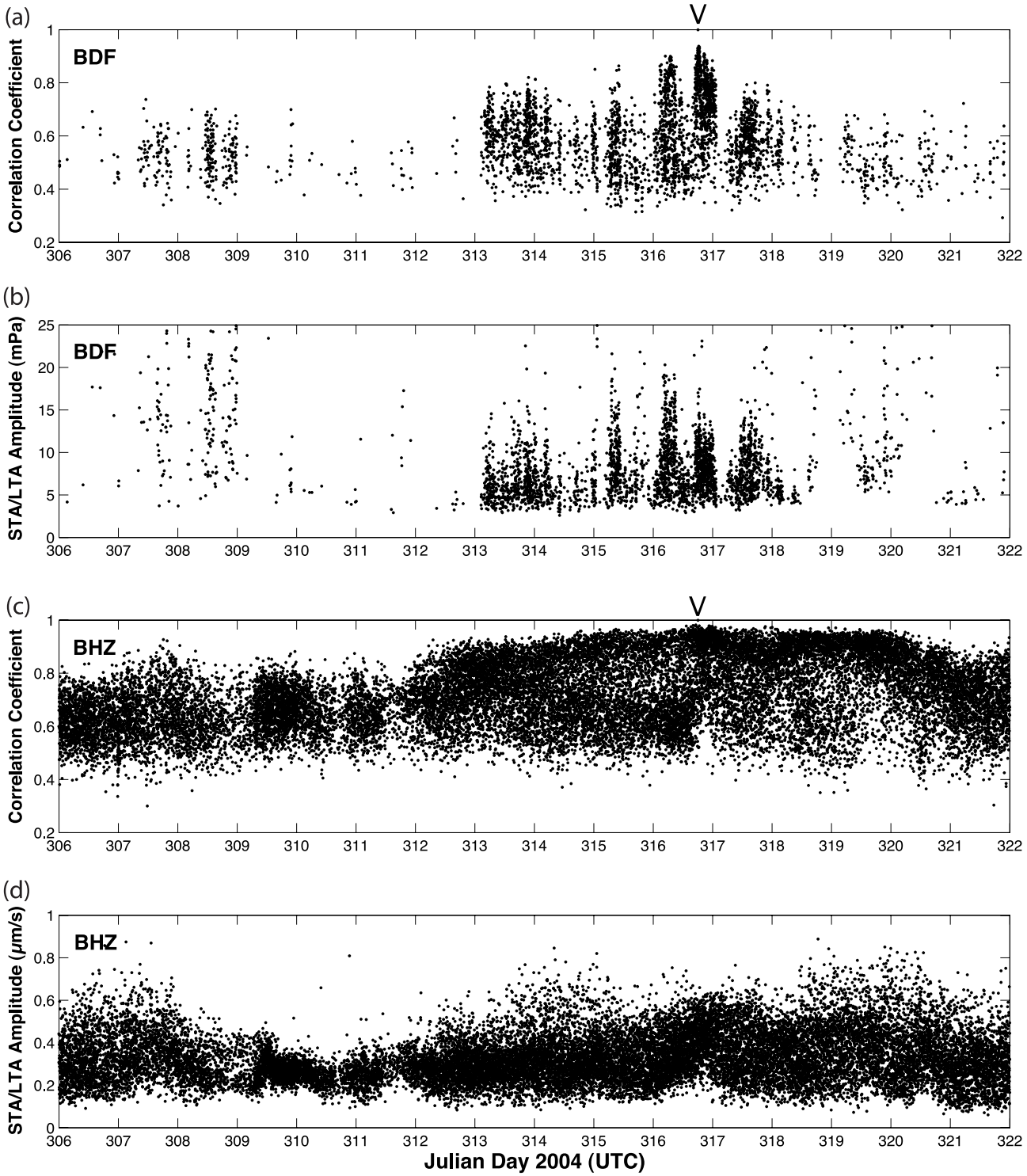

Figure 7. Waveform changes observed at CDWR 1–16 November (JD 306–322) 2004. (a and b) Infrasonic (BDF) correlation coefficient (CC) with master (location indicated by "V"), and event amplitude. (c and d) Seismic (BHZ) CC and amplitude. The seismic CC gradually evolves with time, peaking at the location of the master event, while the infrasonic events appear in discrete "bursts" of signal (especially JD 315–318). The occurrence of infrasonic detections depends to a first order on the seismic amplitude (infrasonic detections are more likely when the seismic amplitude is higher).

demonstrate the repetitive action of a nondestructive source [e.g., *Stephens and Chouet*, 2001; *Green and Neuberg*, 2006; *Thelen et al.*, 2009; *Waite et al.*, 2008; *Petersen*, 2007]. Gradual evolution of observed waveforms implies a change either in the Greens function describing all propagation from source to receiver, or in the source time function. For seismic data, a change in waveform correlation over time typically implies a change in the source

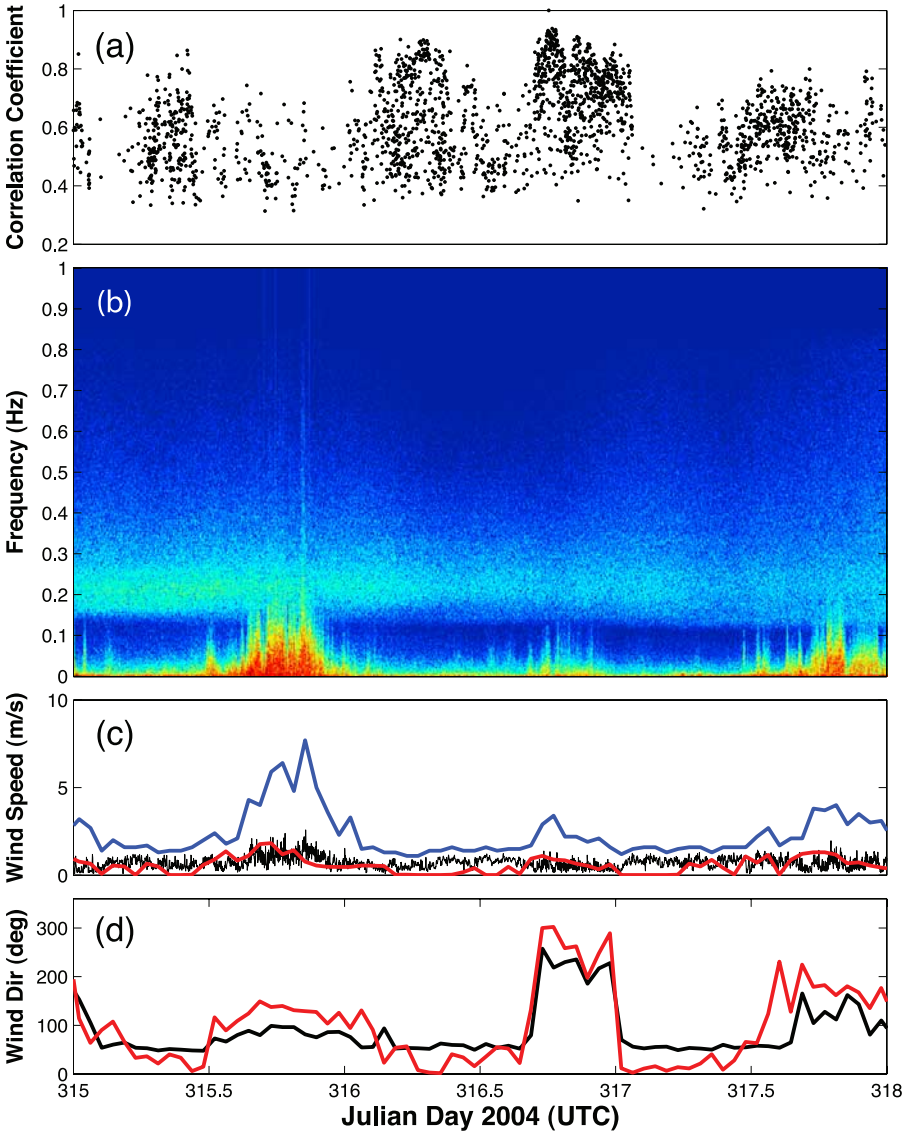

Figure 8. Comparison of infrasonic waveform correlation with available wind data 10–12 November (JD 315–318) 2004. (a) Infrasonic CC with master event (Figure 7). (b) Spectrogram of low-frequency (0–1 Hz) pressure at CDWR central infrasonic sensor element. (c) Black, 1-min wind speed average at CDWR; blue, hourly wind speed max at CDWR; red, hourly wind speed max at NWAC. (d) Black, hourly wind direction average at CDWR; red, hourly wind direction average at NWAC. At least one measured wind speed increase (JD 315.5–316) is associated with a loss in signal correlation. The diffuse peak at ~0.2 Hz in the spectrogram is the microbarom peak. Wind direction is defined as the direction from which wind is blowing.

location or source time function. Acoustic propagation is further subject to time-dependent variability in atmospheric conditions, especially changes in temperature and wind. In this case, a change in the waveform correlation with time can imply a change in the source location, source time function, or a change in the atmospheric conditions.

3.1. Waveform Changes: 1–16 November 2004

[25] We analyze CDWR data for 1–16 November, or Julian days (JD) 306–322, 2004 (Figure 7). This corresponds to the time period depicted by *Matoza et al.* [2007, Figure 3], where Progressive MultiChannel Correlation (PMCC) [*Cansi*, 1995] detection of infrasound from LPs was observed to switch on and off while the seismic LP events were continuously observed (see Figure S3). We also analyzed data from 1 to 19 March 2005 using the same method and obtained similar results. All data were bandpass filtered at 2–4 Hz and the infrasound data were beamformed (azimuth 153°, speed 330 m/s). Events were picked using the STA/LTA detector, then progressively selected for correlation with the master event using 11 s windows (3 s pretrigger, 8 s posttrigger). In Figure 7, the master event (seismic, 1803:38 UTC; infrasonic, 1804:16 UTC, 11 November 2004) was an event arbitrarily chosen from a time period of good seismic and infrasonic signal-to-noise

ratio. The maximum linear correlation coefficient (CC) between each event and the master is shown in Figure 7. For clarity, we emphasize that the infrasound and seismic data were considered separately. Correlation between infrasonic pressure and seismic velocity or displacement waveforms was always low (CC < 0.1).

[26] The seismic LP sequence during this time period is characterized by a gradually evolving waveform, with the CC values peaking at the time of the chosen master event, and sloping off before and after. We found that choosing a different master event simply caused the peak in CC values to occur at the location of the new master. This is reminiscent of the results of *Stephens and Chouet* [2001], who observed a gradual evolution in correlation between individual LP events comprising a 23-h swarm preceding the 14 December 1989 eruption of Redoubt (Alaska). Our results are also consistent with *Thelen et al.* [2009], who analyzed the same time period at MSH using station ELK (~17.3 km from MSH). *Thelen et al.* [2009] separated events with CC > 0.8 into "multiplets," and found that new multiplets continuously appeared during this time period, with the CC decreasing as a function of time during the lifespan of the multiplet.

[27] In contrast, the infrasonic LPs for the same time period occur in discrete "bursts" of signals. Generally, events within each burst are well correlated with one another, but poorly correlated with signals in bursts at other times. The correlation falls off more rapidly in time than in the seismic data. Of the 3530 infrasonic triggers in this 16-day time period, only 750 (21%) were correlated with the master with CC above 0.7. For the 24753 seismic triggers, 13317 (54%) were correlated with CC above 0.7. Considering only seismic LP events that had a detected infrasonic arrival, 2463 (70%) of the 3530 events had CC greater than 0.7. Therefore, we conclude that the infrasonic waveform is less stable than the seismic waveform, changing on fine timescales while the seismic waveform is stable for days to weeks. The cause of infrasonic waveform instability is most likely atmospheric variability.

3.2. Atmospheric Influence on Waveforms: 10–12 November 2004

[28] The influence of atmospheric effects is apparent in the data between 10 to 12 November (JD 315–318) 2004. Figure 8 shows the cross correlation results (Figure 7) for this time period, directly compared with the low-frequency (0–1 Hz) infrasonic spectrogram from the central element at CDWR, and wind data. The wind data are taken from CDWR, and from a meteorological station operated by the Northwest Weather and Avalanche Center (NWAC) located ~500 m south of CDWR. There is general agreement between the wind data for both sites, though the CDWR hourly maximum wind speed is higher than that for the NWAC data probably due to differences in data sampling rate (1 sample/sec for CDWR, 1 sample/10 s for NWAC). Noise in the low-frequency infrasound data (0.02–0.3 Hz) increases with the wind speed, and may be considered a proxy for wind speed in the boundary layer [*Fee and Garcés*, 2007].

[29] In Figure 8 there are four "bursts" of infrasonic signals characterized by an increase in number of events, amplitudes, and correlation between the events. Between JD 315.5 and 316 the wind speed increases, resulting in decorrelation of the infrasonic waveforms and a decline in the number of detected events. Once the wind speed decreases, the detections return and correlation is restored. Between JD 316.5 and 317, a sharp change in the wind direction is observed. This coincides with a time of increased infrasonic detection and waveform correlation, suggesting that atmospheric conditions are somehow adjusted for stable reception of signal. However, wind blowing from source to receiver should enhance signal detection, while wind blowing from receiver to source should hinder signal detection [*Reynolds*, 1873]. The fact that the measured wind direction is blowing approximately from receiver to source (~330°) during the increase in signal reception from JD 316.5 to 317 suggests that the wind conditions measured near CDWR are not representative of the wind conditions along the propagation path between the LP source and CDWR (see Figure S3 for the longer sequence of atmospheric data (1–16 November 2004)).

[30] The effect of atmospheric conditions on waveforms is illustrated in Figure 9. The 2042 infrasonic and 5897 seismic events during this time period are aligned by cross correlation in chronological order for comparison (filtered 1–5 Hz). To exclude spurious automatic picks, only events having CC > 0.2 with a time-evolving master event [*Stephens and Chouet*, 2001] have been included. A stacked master event is formed from the point-by-point 10% trimmed mean of the waveforms, and 95% confidence intervals on the mean were computed by bootstrapping with 1000 samples [*Rice*, 1995]. The point-by-point standard deviation and 5 and 95 percentiles of all waveforms are also shown, illustrating the observed variability in the waveforms. Individual events were not normalized by their maximum amplitude, so larger amplitude events contribute more significantly to the master than lower SNR events.

[31] Figure 9a demonstrates the similarity of seismic LP waveforms during these 3 days. The only variability is in minor changes in the amplitude of each waveform, as evidenced in the shaded percentile region of the master stack. In contrast, the infrasonic waveforms in Figure 9b show continuous fluctuation and variability. Apart from amplitude changes, individual peaks and troughs in the waveforms move relative to one another, indicative of fine changes in the atmospheric propagation path, while strong winds result in decorrelation and loss of the signals. However, on average, the basic waveform structure is unchanged, even after the signals have faded and reappeared. This suggests that subtle waveform changes and "switching on and off" of the infrasonic LP detections are a result of boundary layer dynamics [*Fee and Garcés*, 2007], rather than time-varying source effects. Also, infrasonic waveforms appear weakly correlated at low amplitude for as long as 30 s. This suggests that low-amplitude seismic-acoustic conversion from a long-duration source time function may be important for the later stages of the infrasonic waveforms.

4. Numerical Modeling of Seismic-Acoustic Conversion From a Point Source

[32] Seismic wave propagation in volcanic settings is influenced by topography and heterogeneity in material

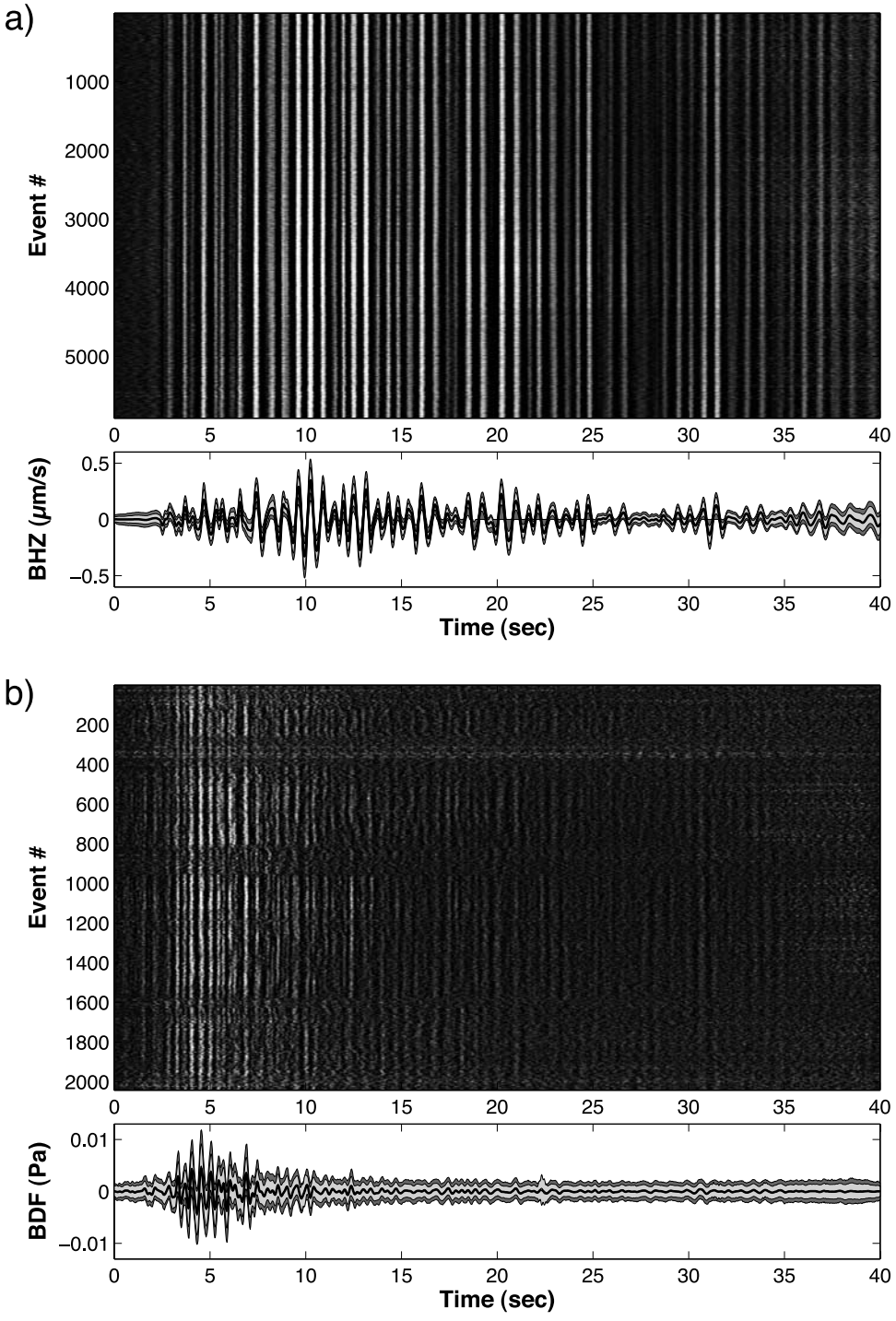

Figure 9. (top) Waveform variability at CDWR 10–12 November (JD 315–318) 2004. Individual detected events (filtered 1–5 Hz) are aligned by cross correlation in chronological order (from top to bottom). There are (a) 5897 seismic events and (b) 2042 infrasonic events. (bottom) A master waveform formed from the 10% trimmed mean of all waveforms (thick black line), standard deviation of all waveforms (light gray), and 5 and 95 percentiles of all waveforms (dark gray). The bootstrapped 95% confidence intervals on the mean master event are plot in white and are thinner than the black line used on this plot. Both data are characterized by highly repetitive waveforms, but the infrasonic data are subject to subtle waveform variations. Decorrelation of infrasonic waveforms is observed between events 250 to 400, 800 to 950, and 1550 to 1750.

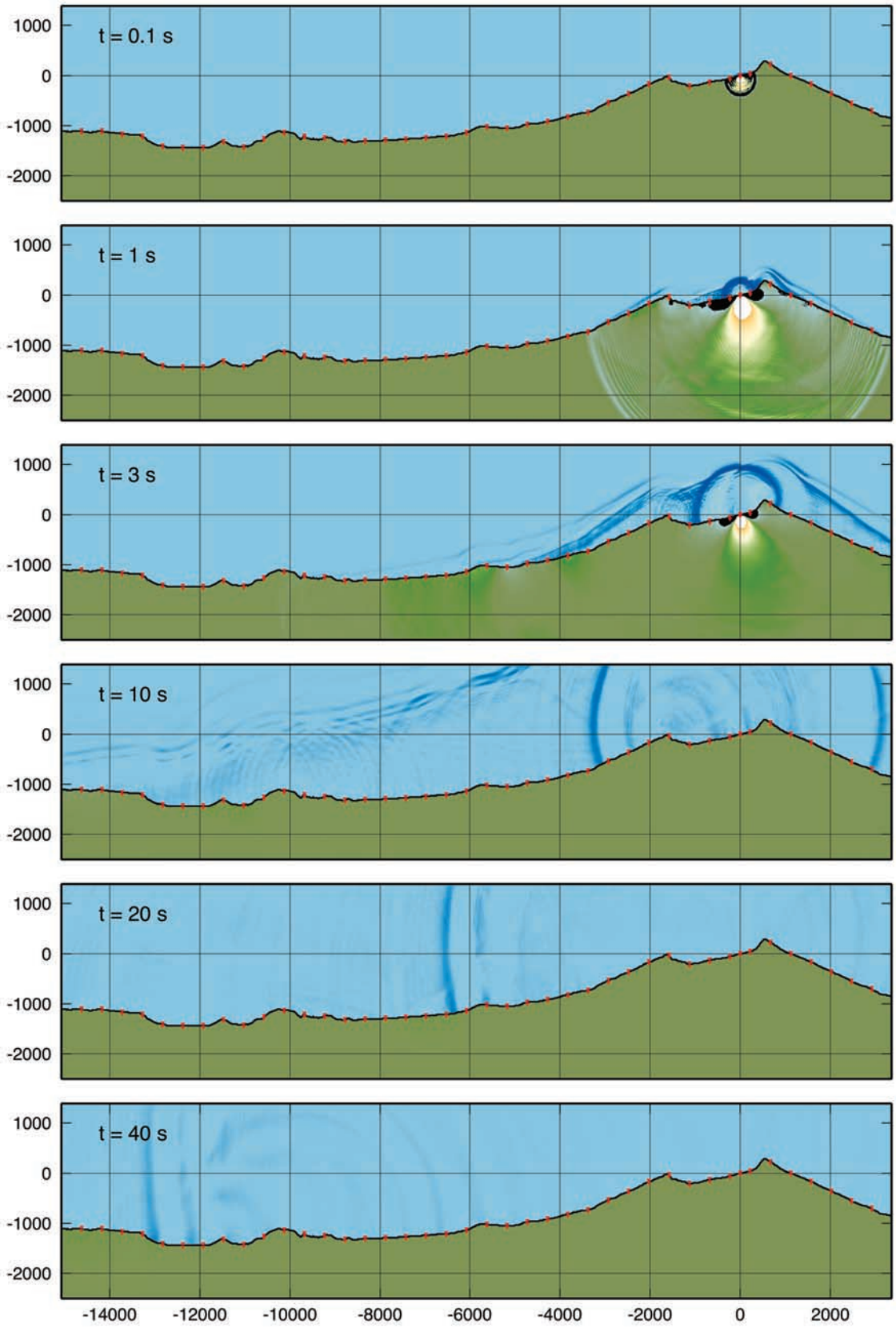
t = 0.1 s
t = 1 s
t = 3 s
t = 10 s
t = 20 s
t = 40 s
1000
0
-1000
-2000
-14000
-12000
-10000
-8000
-6000
-4000
-2000
0
2000

Figure 10

properties. Consequently, finite difference methods are usually used in volcano seismology to compute Greens functions for moment tensor inversions [*Chouet et al.*, 2003], or travel times for tomographic inversions [*Benz et al.*, 1996]. In this study, we use a finite difference code, ASTAROTH [*D'Auria and Martini*, 2007], to investigate seismic-acoustic wave conversion and coupling from a shallow buried source. Following *Virieux* [1986], seismic propagation in the elastic solid and acoustic propagation in the (inviscid) fluid atmosphere are solved simultaneously using a single velocity-stress computational scheme. The fluid is defined by a zero *S* wave velocity (V_s, $\mu = 0$), and appropriate values for the density and sound speed (*P* wave velocity, or V_p) of air. This approach does not require explicit free-surface boundary conditions to define the coupling at the topography surface between the solid earth and atmosphere. Seismic-acoustic conversion results from weak energy transmission controlled by effective material properties at the solid-fluid interface [*van Vossen et al.*, 2002].

[33] The governing equations are the equations of elastodynamics in 3-D Cartesian coordinates:

$$\begin{aligned} \partial_t \tau_{ij} &= \lambda(\partial_k v_k)\delta_{ij} + \mu\left(\partial_i v_j + \partial_j v_i\right) \\ \partial_t v_i &= \rho^{-1}\left(\partial_j \tau_{ij} + f_i\right) \end{aligned} \tag{1}$$

where τ_{ij} is the stress tensor, v_i is the (Lagrangian) particle velocity, δ_{ij} is the Kronecker delta, μ and λ are the Lamé parameters, ρ is the density, f_i is the body forces (source term), and the Einstein summation convention is assumed. Equations (1) are equivalent to the acoustics equations in the fluid when acoustic pressure $p = -\tau_{ii}/3$, $\mu = 0$, and $\lambda = \kappa$ (bulk modulus) $= \gamma p_0$ in an ideal gas (p_0 reference pressure, $\gamma = c_p/c_v$ ratio of specific heats) [*D'Auria and Martini*, 2007]. Since the acoustic wave equation is retrieved by linearizing Euler's equation [*Landau and Lifshitz*, 1987], static wind fields (wind speeds that vary as a function of position but not time) can be considered simply by adding advective terms [*D'Auria and Martini*, 2007]:

$$\begin{aligned} \partial_t \tau_{ij} &= \lambda(\partial_k v_k)\delta_{ij} + \mu\left(\partial_i v_j + \partial_j v_i\right) - (w_l \partial_k \tau_{kl})\delta_{ij} \\ \partial_t v_i &= \rho^{-1}\left(\partial_j \tau_{ij} + f_i\right) - \left(w_j \partial_j v_i\right) \end{aligned} \tag{2}$$

where w_i is the wind velocity ($w_i = 0$ in the elastic nodes).

[34] Equations (2) are solved using a staggered grid finite differences scheme that is second order in space and time. Arbitrary moment tensor and single-force sources are implemented as distributions of body forces f_i on velocity nodes [*Graves*, 1996] with an arbitrary source time function, and perfectly matched layer (PML) absorbing boundary conditions are imposed around the edge of the computational volume [*Berenger*, 1996; *Festa and Nielsen*, 2003]. The parallel code is written in C++/MPI, and proceeds by dividing the computational volume into equal subvolumes during each time step (master-slave implementation).

4.1. Model Configuration

[35] The strong velocity contrast considered leads to some practical limitations. To limit numerical dispersion, 10 grid points per minimum wavelength are required. For an atmospheric sound speed of 330 m/s, a denser grid sampling is required than in typical seismic applications. We restricted our models to frequencies <2 Hz by choosing a grid spacing of 15 m for all spatial dimensions. For this grid spacing and maximum velocity ($V_{\max} = V_p = 3500$ m/s) we found empirically that a time step of 1×10^{-4} s was required for stability. Considering the 14 km source-receiver distance, this grid spacing and time step result in a significant computational effort. Hence, our model geometry was chosen to minimize the computational volume.

4.1.1. Model Geometry

[36] Initial calculations were performed for a 2-D profile connecting the LP source location and CDWR location (Figure 1). Although capturing the basic properties of wave propagation (section 4.2.1), this does not correctly predict the geometrical spreading loss. Rather than extending to a fully 3-D geometry, we use a 2.5-D geometry where the *x* axis runs along the 2-D profile described above, and the *y* dimension is restricted to 51 grid points centered on this line (Figure 1). The wave propagation is 2.5-D in the sense that backscattering from topography outside this narrow strip is neglected. Tests showed that the PML absorbing boundaries sufficiently reduced edge reflections for this geometry. The final computational volume was NX × NZ = 1250 × 261 = 326,250 nodes for the 2-D model, and NX × NY × NZ = 1250 × 51 × 261 = 16,638,750 nodes for the 2.5-D model. The topography data are the same as used by *Waite et al.* [2008], consisting of USGS topographic map data outside the crater, and a DEM constructed from aerial photographs taken on 19 April 2005 [*Schilling et al.*, 2009] inside the crater. The topography data were interpolated onto the regular 15 m grid (staircase approximation for topography). Discretization of the staircase boundary was sufficient to limit nonphysical scattering for the topography gradients considered [*de Groot-Hedlin*, 2004]. Synthetic sensors were positioned at 450 m spacing along the *x* axis (Figure 10), with one sensor positioned 2 grid points above the topography surface (synthetic acoustic sensor), and one sensor positioned 2 grid points below the topography

Figure 10. Pressure wavefield snapshots for a 2-D simulation. From top to bottom, snapshot times of 0.1 s, 1 s, 3 s, 10 s, 20 s, and 40 s. An isotropic point source with an arbitrary impulsive source time function is located 60 m below the crater floor at the position (0, 0, −60). Homogeneous material properties are assumed for the solid earth ($V_p = 3500$ m/s, $V_s = 2020$ m/s, and $\rho = 2650$ kg/m^3) and atmosphere ($V_p = 330$ m/s, $V_s = 0$ m/s, and $\rho = 1.2$ kg/m^3). Synthetic sensors are located two grid points away from either side of the ground surface (red triangles, see Figure 13). Two distinct atmospheric pressure waves result from the buried source: (1) locally converted or "leaky" *P*/*SV* and Rayleigh wave energy that travels along the ground surface at seismic velocity and radiates energy continuously into the overlying atmosphere and (2) hemispherical wavefronts traveling at acoustic velocity (330 m/s) resulting from strong ground shaking in a finite region surrounding the source epicenter. See the auxiliary material Movie S1 for an animation sequence of this simulation.

Table 1. Model Configuration

Run	Figures	Geometry	Solid Properties	Atmosphere Properties	M_{xx}:M_{yy}:M_{zz}	F_z	STF	Source Depth (m)
1	10, 12, 13	2-D	Homogeneous	Homogeneous	1:1:1	0	Impulse	60
2	14	2.5-D	Homogeneous	Homogeneous	1:1:1	0	Impulse	60
3	15	2.5-D	Homogeneous	Homogeneous	1:1:1	0	Impulse	195
4	16, 18	2.5-D	Homogeneous	Homogeneous	1:1:3	0	Crack M_{ii}	195
5	17, 18	2.5-D	Homogeneous	Homogeneous	0	1	F_z	195
6, 7	19	2.5-D	Comparison between homogeneous and 500 m weathered layer	Homogeneous	1:1:1	0	Impulse	60
8, 9	21	2-D	Homogeneous, flat topography	Homogeneous	equation (6)	0	WETC3D	50
10, 11	22	2-D	Homogeneous, crater topography	Homogeneous	equation (6)	0	WETC3D	30
12	24a	2-D	None	G2S 1 Nov 2004 0600 UTC no wind	1:1:1	0	Impulse	−160
13	24b	2-D	None	G2S 1 Nov 2004 0600 UTC with wind	1:1:1	0	Impulse	−160
14	24c	2-D	None	G2S 1 Nov 2004 1800 UTC no wind	1:1:1	0	Impulse	−160
15	24d	2-D	None	G2S 1 Nov 2004 1800 UTC with wind	1:1:1	0	Impulse	−160
16	24e	2-D	Homogeneous	G2S 1 Nov 2004 0600 UTC no wind	1:1:1	0	Impulse	60
17	24f	2-D	Homogeneous	G2S 1 Nov 2004 0600 UTC with wind	1:1:1	0	Impulse	60
18	24g	2-D	Homogeneous	G2S 1 Nov 2004 1800 UTC no wind	1:1:1	0	Impulse	60
19	24h	2-D	Homogeneous	G2S 1 Nov 2004 1800 UTC with wind	1:1:1	0	Impulse	60

surface (synthetic seismic sensor). The coordinate system is centered on the epicenter of the LP source.

4.1.2. Material Properties

[37] In the initial 2-D and 2.5-D simulations (runs 1–5, Table 1) we used homogeneous medium properties in the solid earth and atmosphere. For the solid, V_p = 3500 m/s, V_s = 2020 m/s, and ρ = 2650 kg/m^3, and for the fluid, V_p = 330 m/s, V_s = 0 m/s, and ρ = 1.2 kg/m^3. *Waite et al.* [2008] did not find an appreciable difference between results obtained with a homogeneous velocity model and those derived from the best available 3-D velocity model [*Waite and Moran*, 2006], in part because low frequencies (<2 Hz) were considered.

[38] We also use a homogeneous atmosphere free from density and sound velocity variation. In section 2.1.3 we showed that statistical averaging of waveform and amplitude properties for thousands of events sampling a wide range of atmospheric conditions removes much of the variability in the atmosphere, leaving the ''average'' atmosphere case. This ''average'' atmosphere may be interpreted in two ways. In one scenario, no particular atmospheric condition (e.g., a specific wind direction) favors detection of the signals. In this case the ''average'' P/V_z ratio determined in section 2.1.3 would correspond to acoustic propagation in a homogeneous atmosphere as considered in our numerical modeling. However, in a second scenario, a specific atmospheric condition (e.g., wind direction) could be the cause of stable signal reception. In this case, the PDFs shown in Figure 4c would be biased toward these conditions, and our numerical modeling with a homogeneous atmosphere may underestimate the P/V_z ratio as determined in section 2.1.3, as focusing by wind or temperature has been neglected. Since we do not have detailed specifications of the atmospheric conditions between the LP source and CDWR, the role of atmospheric effects are considered separately in section 6 where we investigate more realistic temperature, density, and wind speed profiles.

[39] In a second set of 2.5-D simulations using a smaller computational volume (runs 6–7, Table 1, section 4.2.5), we include a near-surface weathered layer of thickness 495 m, with V_p = 2000 m/s, V_s = 1155 m/s, and ρ = 2000 kg/m^3 based on material properties used and evaluated by *Virieux* [1986], *Thelen et al.* [2009], and *Scheu et al.* [2006]. Because of the low frequencies (<2 Hz) and relatively short ranges (<15 km) considered, we do not introduce intrinsic attenuation into any of our models.

4.1.3. Point Sources

[40] Of concern in our study are (1) the sensitivity of the amplitude ratio (P/V_z) observed at CDWR to changes in the source depth and moment tensor/single-force configuration and (2) the predicted infrasonic waveform duration at 13.4 km range from a buried impulsive and long-duration source time function (STF). Because of computational requirements, only a small set of models could be run to investigate these effects. Therefore, only four runs (runs 2–5) were performed with the full 2.5-D model, each with a different source configuration (Table 1 and Figure 11). In runs 1–2, a source was placed 4 nodes (60 m) below the topography surface (as close to the surface as possible without the source body force nodes interacting with the free surface directly). In these runs, an arbitrary pulse-like STF was used with an isotropic moment tensor: $M_{xx} = M_{yy} = M_{zz}$ = 1 (off-diagonal elements equal 0). In runs 3–5 the source was moved to 195 m depth (13 grid points) below the topography surface. This is the source location obtained by *Waite et al.* [2008] using the same topography. Runs 3–5 differ in the STF used. Run 3 used the arbitrary pulse STF with isotropic moment tensor (same as runs 1–2). Run 4 used the STF and moment tensor obtained by *Waite et al.* [2008] by full waveform inversion, with the moment tensor rotated into our coordinate system. This source can be interpreted as the volumetric oscillations of a crack in a Poisson solid ($\lambda = \mu$), so this run gives an indication of how crack resonance at the given source location would couple into the atmosphere. In run 5, the same source location was used, but with a source corresponding to the vertical single-force component (F_z) imaged in the moment tensor and single-force inversions. In the runs using the impulsive STF, time stepping was performed until t = 50 s. In runs using the crack STF (~30 s duration), time stepping was performed until t = 90 s to capture the full duration of the signal. In our representation of moment tensor and single force, the source is a point source. Hence, the horizontal extent of the fluid-filled crack is neglected. In section 5 we consider the

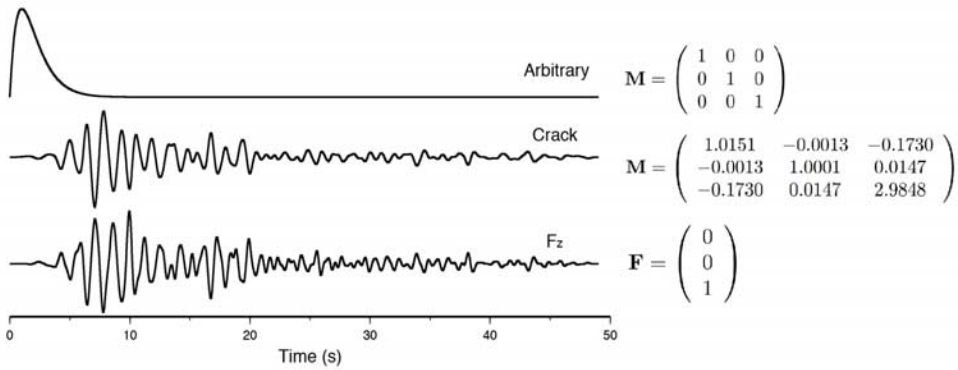

Figure 11. Source time functions used in this study. (top) Arbitrary pulse-like source time function used with an isotropic moment tensor. (middle) Crack source time function from *Waite et al.* [2008] and corresponding moment tensor components rotated into our coordinate system. (bottom) Vertical single-force component from *Waite et al.* [2008].

limitations of this assumption by considering the seismo-acoustic wavefield resulting from an extended fluid-filled crack source.

4.2. Results

4.2.1. Wavefield Structure From 2-D Simulation

[41] The acoustic wavefield structure resulting from an impulsive shallow buried source is best illustrated in the 2-D simulation results of Figures 10, 12, and 13 (see also Movie S1). Two distinct acoustic arrivals result from this source configuration, in general agreement with the observations of *Le Pichon et al.* [2002, 2003], *Mutschlecner and Whitaker* [2005], and *Sylvander et al.* [2007]. The first corresponds to locally converted *P*/*SV* and Rayleigh wave energy (identified by particle motion analysis, see Figure S4), and travels along the ground surface at seismic velocity, arriving at the infrasonic sensor coincident with the seismic energy. Note in Figure 10 how the wavefronts in the atmosphere form at a shallow angle (dependent on elastic wave speed) to the topography surface and that amplitude increases along the wavefront in the direction away from the solid-fluid boundary, as this energy has left the solid at a later time. These properties are the same as those of "leaky waves" [*Brekhovskikh*, 1980; *Viktorov*, 1967] that form at a solid-fluid boundary when the elastic wave speed is higher than the sound speed in the fluid.

[42] The second arrival corresponds to energy converted in the vicinity of the source epicenter, and travels along the

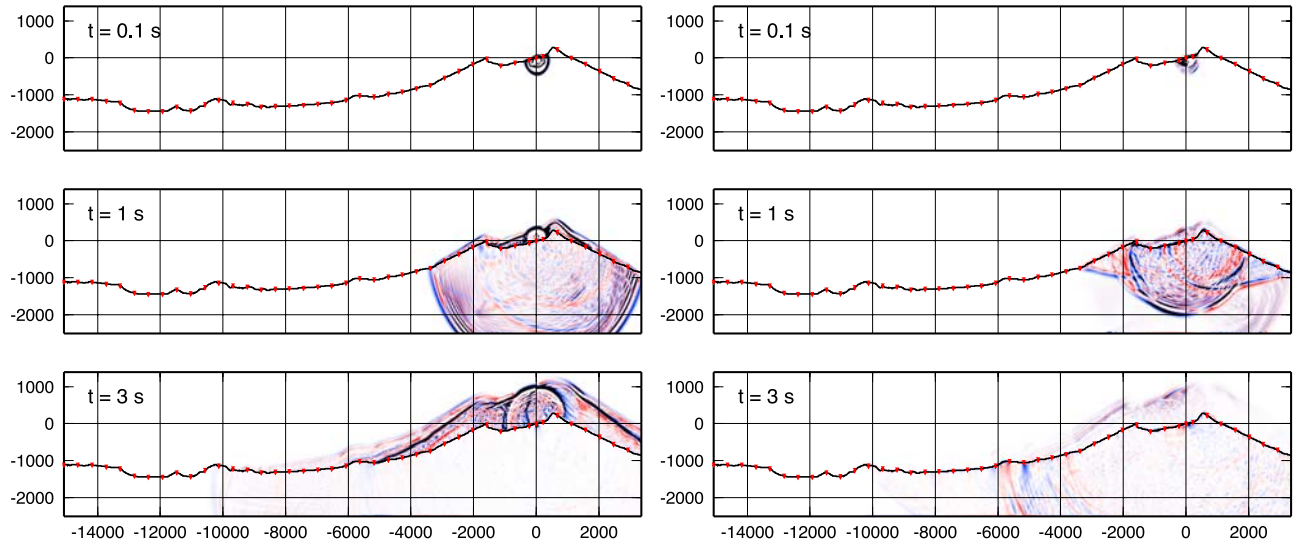

Figure 12. (left) $\nabla \cdot v$ and (right) $(\nabla \times v)_y$ of the vector velocity field v for the simulation shown in Figure 10. From top to bottom, snapshots times are 0.1 s, 1 s, and 3 s. $\nabla \cdot v$ illustrates *P* and Rayleigh wave propagation, while $(\nabla \times v)_y$ illustrates *S* and Rayleigh waves. Conversion of upward *P* to downward *SV* is seen at the free surface, while local seismic-acoustic conversion is seen for both *P* and Rayleigh waves leaving the source. Apparent rotational components traveling at acoustic velocity in the atmosphere and *P* velocity in the elastic solid for $(\nabla \times v)_y$ (right) are artifacts of high-frequency numerical noise (curl does not precisely vanish).

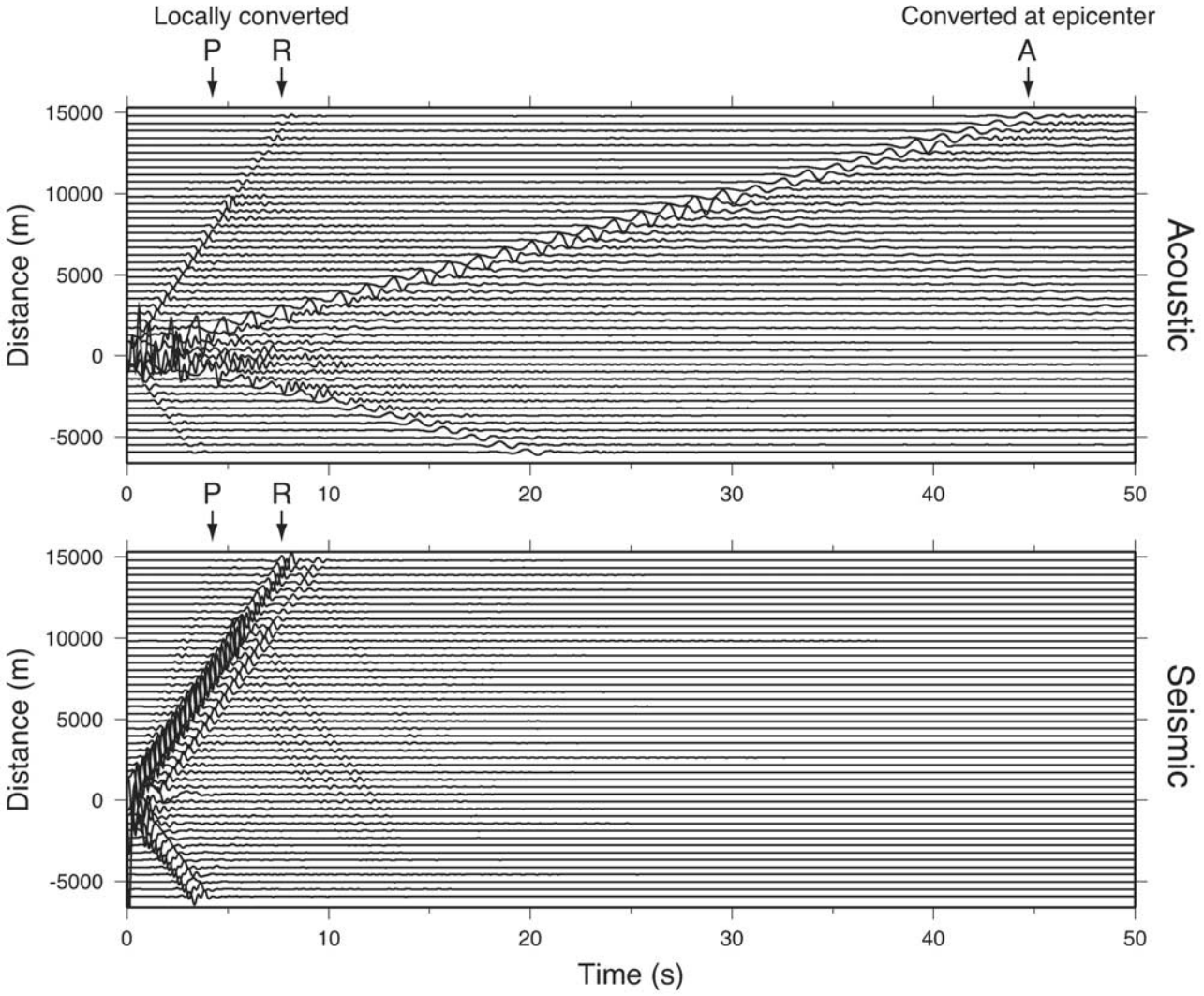

Figure 13. Synthetic record sections for (top) acoustic pressure and (bottom) seismic vertical velocity for a 2-D simulation from an isotropic impulse point source (Figures 10 and 12). The synthetic seismograms show a faint *P* arrival followed by the dominant Rayleigh wave train (*R*). Note the backscattering from topography at ~10 km (see Movie S1). The synthetic acoustic data show the arrival of two distinct packets of energy. The first corresponds to locally converted *P* and Rayleigh wave energy and travels in the atmosphere along the ground surface at seismic velocity. The second corresponds to energy converted from strong ground shaking near the source epicenter and travels through the atmosphere at acoustic velocity (A). Note the asymmetry in amplitudes of A with respect to range, resulting from asymmetry in topography. Although useful for identifying the principal acoustic arrivals from a buried source, 2-D simulations do not adequately predict the amplitude loss due to geometrical spreading.

ground surface at the much slower acoustic velocity, arriving time delayed from the seismic-acoustic coupled (first) arrival (Figure 13). The wavefronts for this second arrival are much steeper, and are hemispherical in the absence of topography (confirmed by calculation not shown here). The lateral extent of this infrasound source is restricted to a radius at which the peak vertical seismic velocity reaches a limiting value for effective infrasound generation, which in turn depends on the amplitude and depth of the seismic source [*Mutschlecner and Whitaker*, 2005]. We note that there is an asymmetry in the amplitude of this second arrival observed in Figures 10 and 13. The acoustic signal propagating to the SE is weaker than the signal propagating to the NW. This appears to result from the asymmetry in topography. The topography in the crater is dipping to the NW (toward CDWR, left in Figure 10), while to the SE the wavefront must diffract over the SE crater wall, which is immediately adjacent to the epicenter of the source where the energy conversion is taking place. This illustrates the importance of topography in the immediate vicinity of the source epicenter for the radiated far-field acoustic amplitude from a buried source.

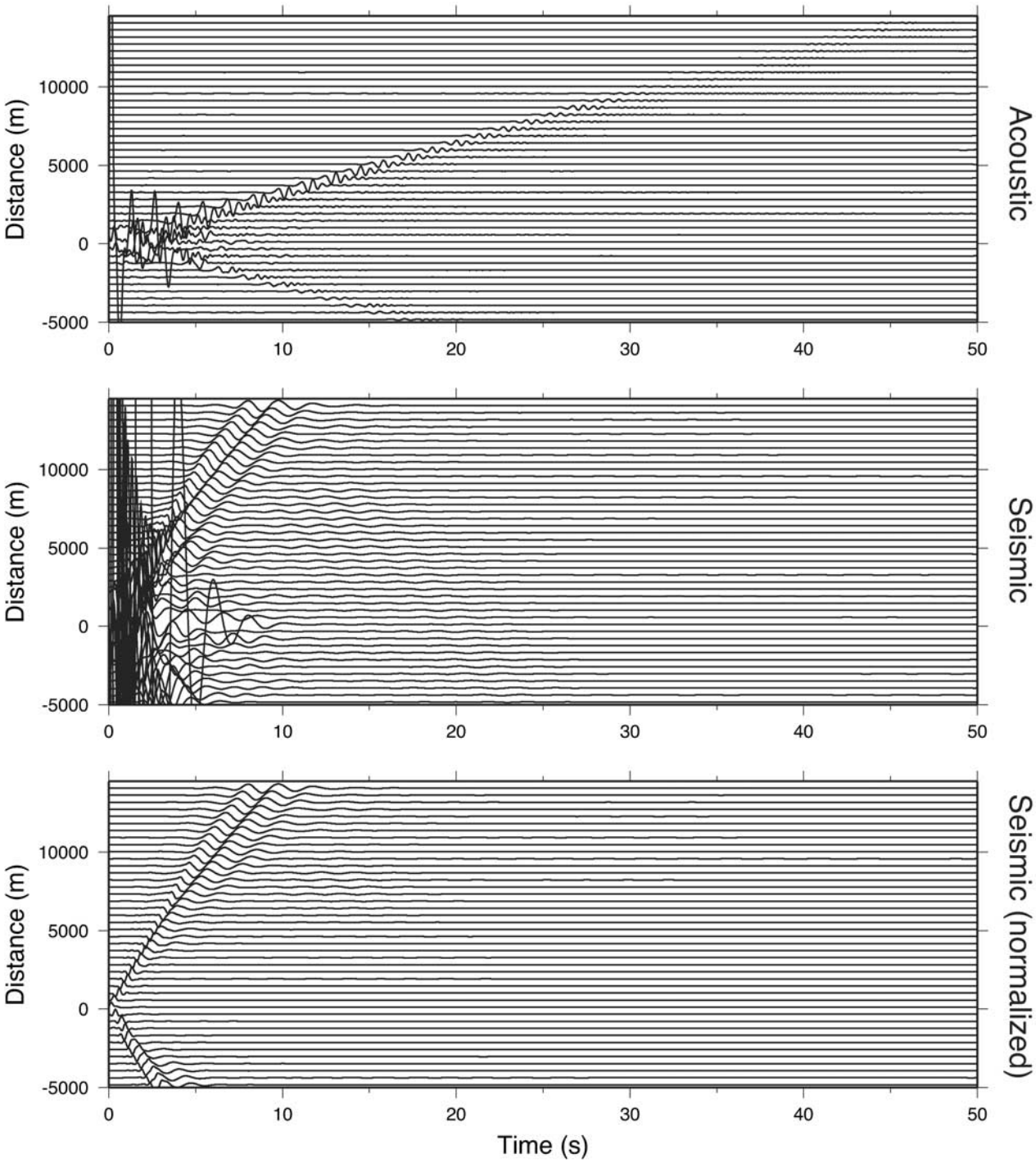

Figure 14. (top and middle) Same as Figure 13 but for a 2.5-D simulation in which the model domain is extended by 51 grid points in the *y* direction (see Figure 1). The same seismic and acoustic arrivals are present, but the geometrical spreading effects are now included. The first clear packet of energy corresponds to the Rayleigh wave propagating in the solid, as the *P* wave is not visible at this scale. The strong ground shaking in the vicinity of the source epicenter is more significant in 2.5-D than 2-D and becomes the dominant source of energy in the atmosphere within a range of ~10 km from the source. However, pressure amplitudes at ~13.4 km are very low. (bottom) Same as Figure 14 (middle) except amplitude of each trace is normalized. Note how dispersion occurs because of interaction with topography and losses into the overlying fluid.

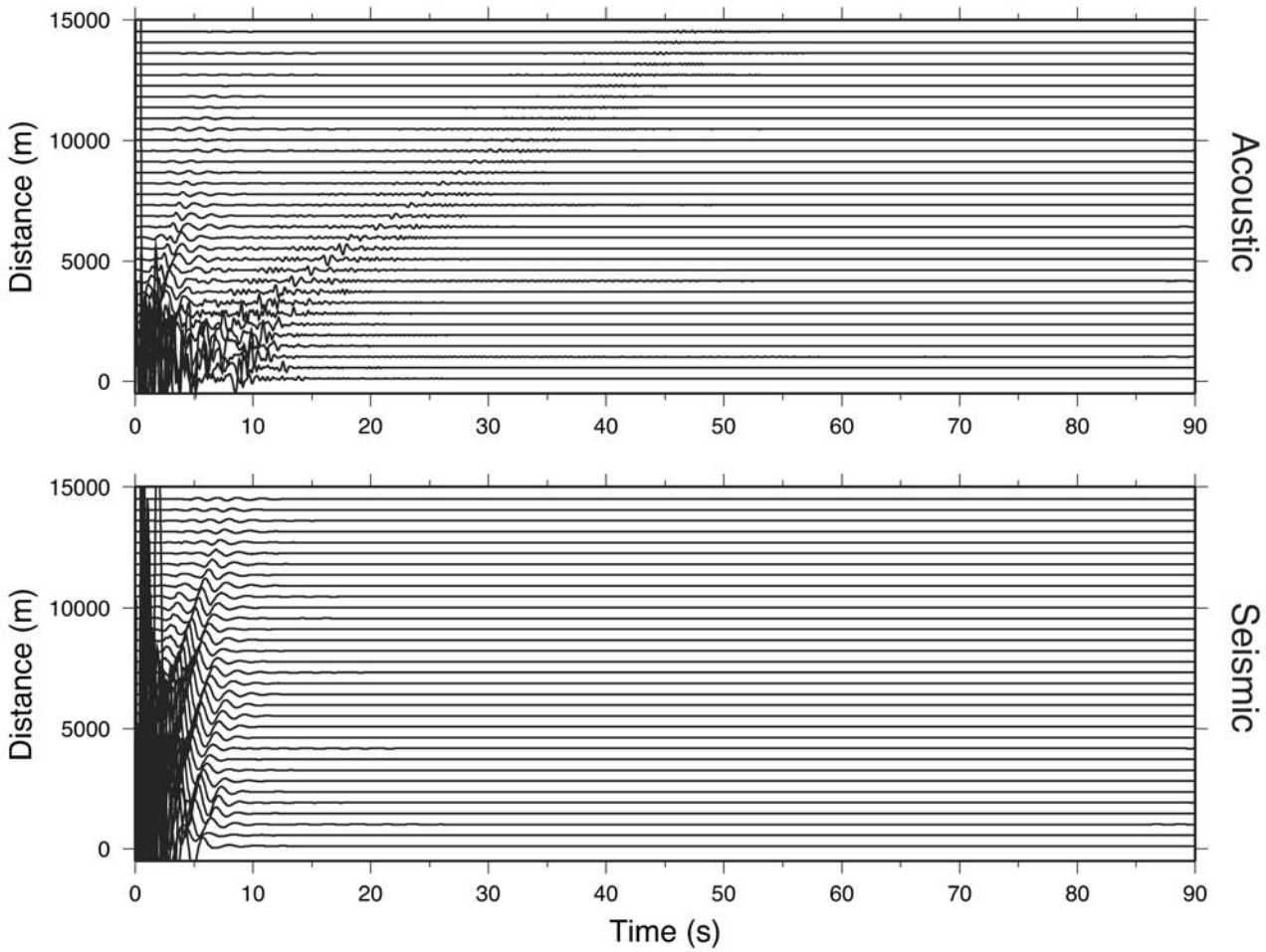

Figure 15. A 2.5-D simulation using a point source at 195 m depth below the ground surface. The source location and DEM used in the simulations are from *Waite et al.* [2008]. An isotropic source (diagonal moment tensor with M_{xx}:M_{yy}:M_{zz} = 1:1:1) with arbitrary impulse source time function is used as in Figures 10, 12, 13, and 14. The traces have not been normalized to illustrate the amplitude decay with distance. Note how the slight increase in source depth from 60 to 195 m results in locally converted seismic-acoustic coupled arrivals having amplitudes comparable to the acoustic energy originating from the source epicenter at all ranges (compare with Figure 14). The acoustic energy at ~13.4 km is very weak.

[43] The seismic wavefield structure is better illustrated in Figure 12. Here, the divergence

$$\nabla \cdot v = \frac{\partial v_x}{\partial x} + \frac{\partial v_z}{\partial z}$$

and y component of curl

$$(\nabla \times v)_y = \frac{\partial v_x}{\partial z} - \frac{\partial v_z}{\partial x}$$

of the vector particle velocity field are shown. The divergence illustrates P and Rayleigh wave propagation, while the curl illustrates S and Rayleigh waves [*Ohminato and Chouet*, 1997]. These plots show clearly the conversion of upward P to downward SV at the free surface, and acoustic waves in the atmosphere locally radiating from P and Rayleigh waves. There are no S waves directly radiated from the volumetric source. A weak reflection from the south crater wall (right in plot) is also apparent in the divergence and pressure field (Figure 10) plots.

4.2.2. The 2.5-D Simulations

[44] Moving from 2-D to 2.5-D simulation for an identical source configuration results in the same basic wavefield structure, but geometrical spreading effects are correctly accounted for. In particular, we find that the acoustic energy originating from the source epicenter becomes more dominant in amplitude for the 60 m depth source within ~10 km of the source, but both locally converted and acoustic arrivals have very low amplitudes at ~13.4 km (Figure 14). We note that the first clear arrival in Figure 14 corresponds to the Rayleigh wave propagating in the solid, as the P arrival is not visible at this scale. Moving the source depth to 195 m results in equal amplitudes for the seismic-acoustic coupled waves and acoustic waves from the source epicenter at all ranges (Figure 15). Thus, the acoustic waveforms generated by a buried source are very sensitive to source depth. In general, we found in test 2.5-D simulations that

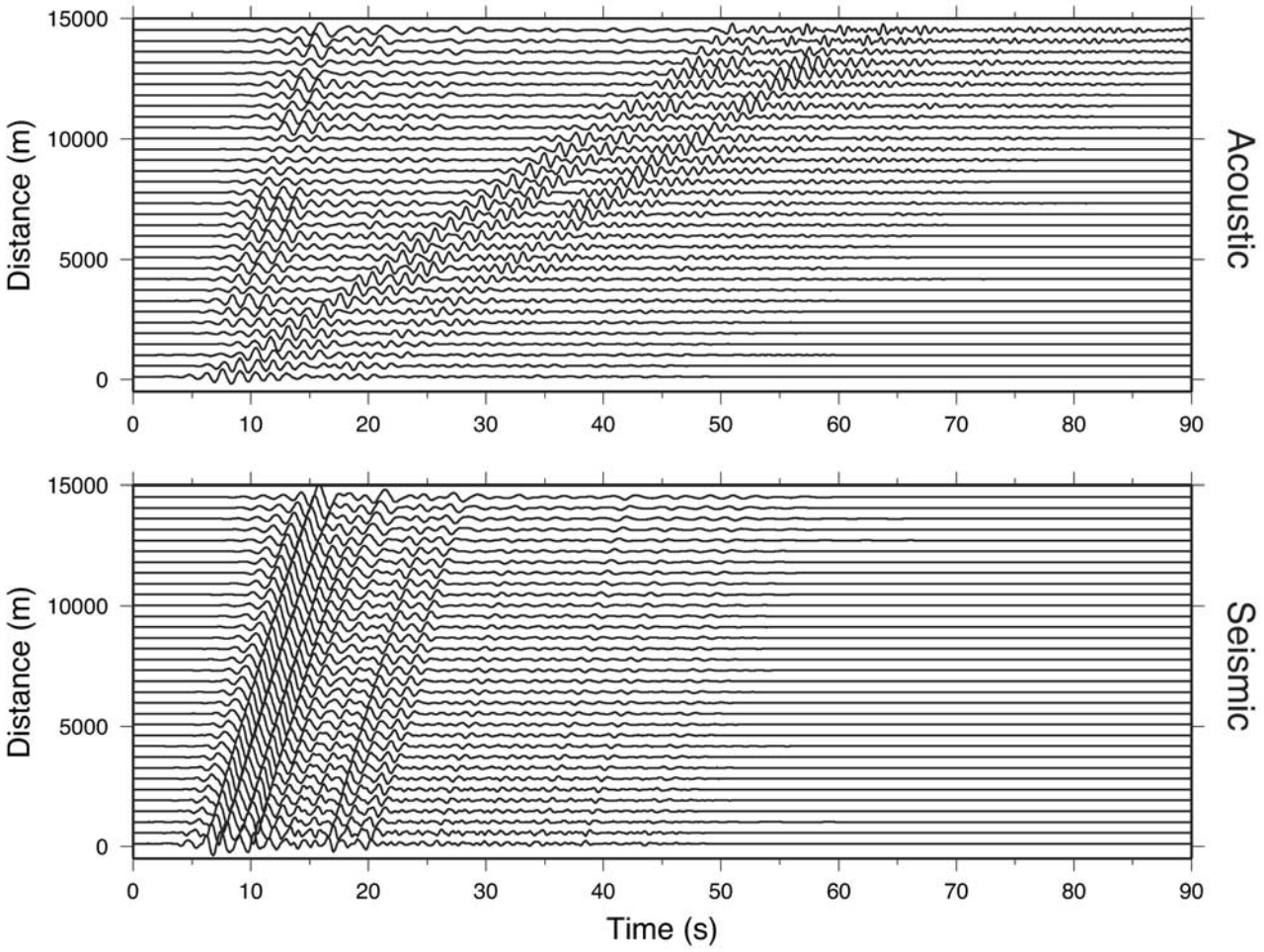

Figure 16. Same as Figure 15 but with subhorizontal crack source (diagonal moment tensor with M_{xx}:M_{yy}:M_{zz} = ∼1:1:3) and long-duration resonant source time function determined from moment tensor inversion [*Waite et al.*, 2008]. Traces have been normalized to clearly show the waveforms. The long-duration source time function generates a long-duration infrasonic signal in the atmosphere, inconsistent with our observations.

increasing the source depth caused the amplitude of the second acoustic arrival to decrease dramatically. At depths on the order of an acoustic wavelength (∼330 m), the energy from the source epicenter is mostly directed vertically upward, with very little horizontal component. We note that all of our simulations predict that at 13.4 km, seismic-acoustic coupled energy and acoustic energy originating from conversion near the source epicenter have comparable amplitudes.

[45] Figures 16 and 17 show the results of using the source parameters obtained from inversion of seismic data [*Waite et al.*, 2008]. Here the changes are (1) the moment tensor and single-force contributions to the source and (2) the long-duration source time function. The effects of these parameters on the amplitude ratio and observed waveform duration are presented below.

4.2.3. P/V_z Ratios

[46] The P/V_z amplitude ratio was found to vary smoothly with range, superimposed by small local perturbations due to topography. Local topography causes focusing and defocusing of seismic energy, which affects V_z [*Ohminato and Chouet*, 1997]. Consequently, only order of magnitude values are considered here. We measured the P/V_z amplitude ratio at 13.4 km distance as the peak synthetic pressure amplitude to synthetic vertical velocity amplitude. Only the atmospheric waves traveling at acoustic velocity (from the source epicenter) are considered. For the 2-D simulation of Figure 13, the P/V_z ratio is $\sim 10^4$ Pa s/m. Moving to 2.5-D and keeping the same source parameters (Figure 14), the P/V_z ratio decreases to 10^3 Pa s/m. Staying in 2.5-D but moving to a source depth of 195 m (the source depth obtained by waveform inversion, Figure 15), the P/V_z ratio drops to $\sim 10^2$ Pa s/m. Changing the moment tensor from isotropic (M_{xx}:M_{yy}:M_{zz} ∼ 1:1:1) to that of a volumetric crack (M_{xx}:M_{yy}:M_{zz} ∼ 1:1:3) and using the long-duration STF (Figure 16) causes an increase in the P/V_z ratio to $\sim 10^3$ Pa s/m, while the vertical single-force component (Figure 17) leads to a P/V_z of $\sim 10^2$ Pa s/m. Figures 16 and 17 show that the F_z source component contributes less to the acoustic pressure waveforms than the volumetric components of the crack. This can be understood by comparing the pressure wavefield structure of these two sources (Figure 18). The

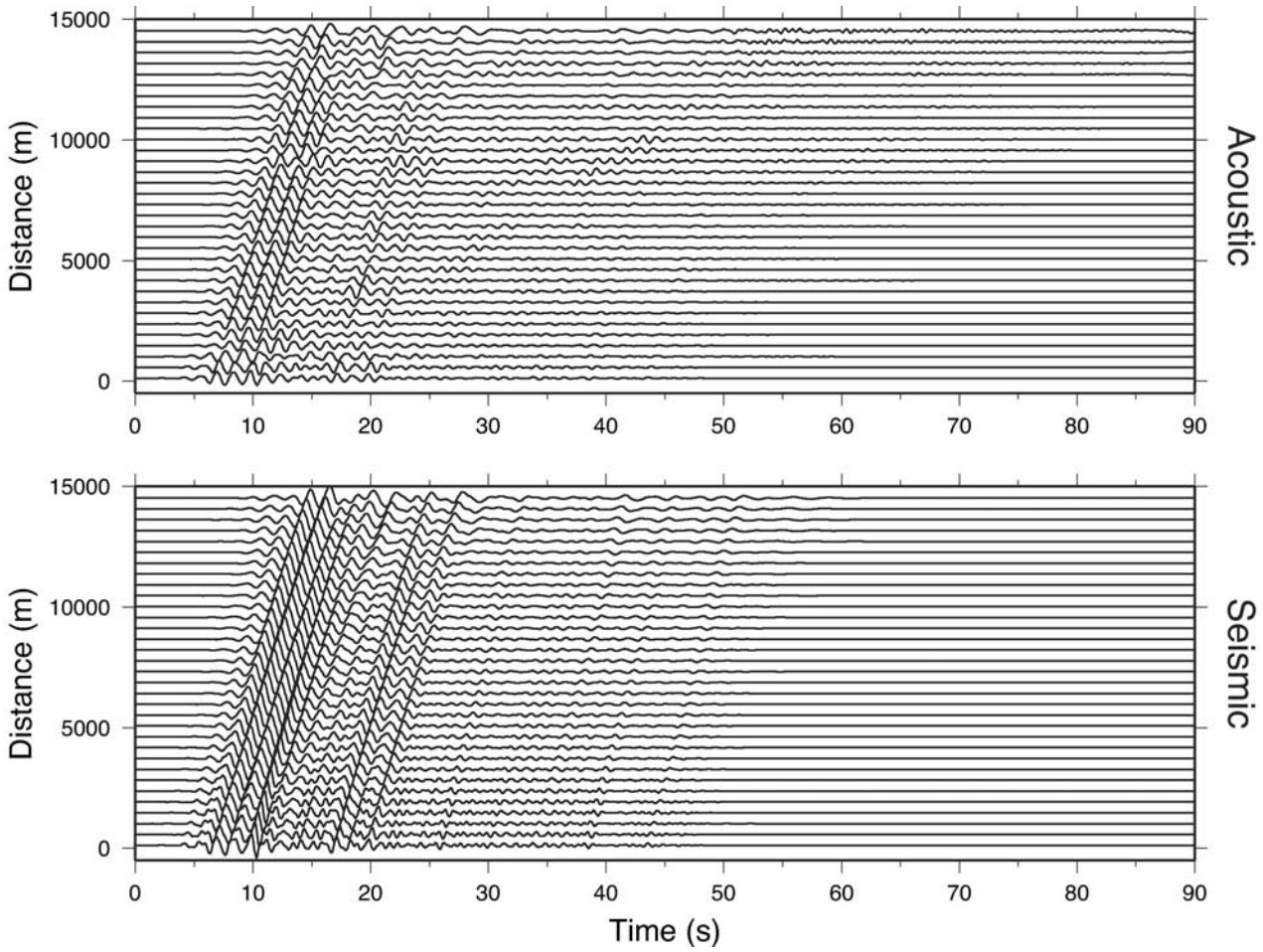

Figure 17. Same as Figures 15 and 16 but with vertical single-force component (F_z) and long-duration source time function obtained by *Waite et al.* [2008]. The results are similar to the volumetric crack source (Figure 16), but the predicted P/V_z ratio at CDWR is smaller. Therefore, we conclude that the F_z component is less significant for horizontally propagating infrasound than the volumetric moment tensor component of the source.

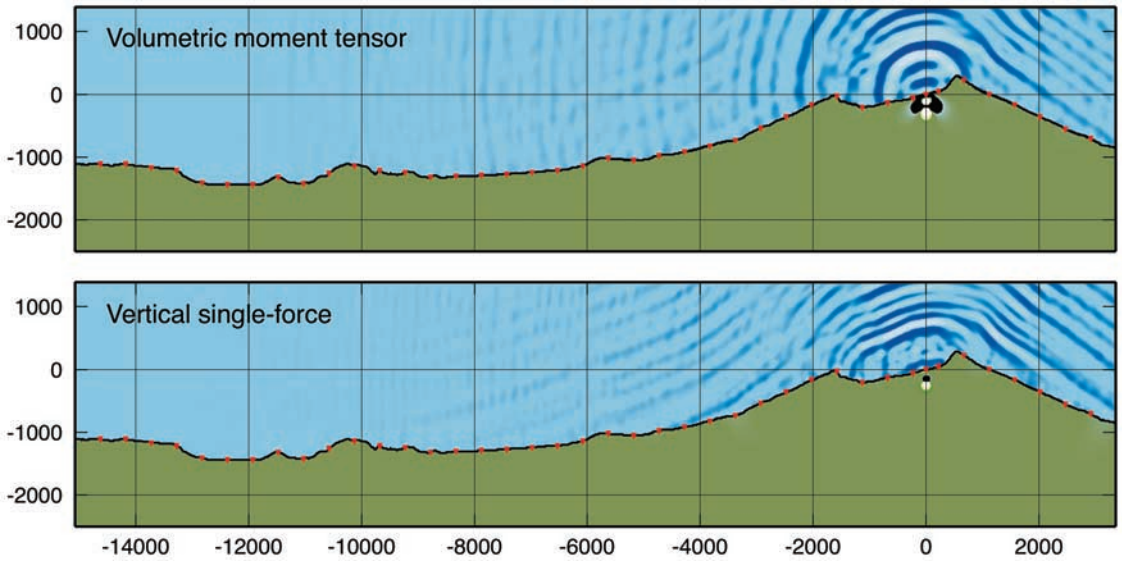

Figure 18. Pressure wavefield structure from (top) volumetric moment tensor and (bottom) vertical single-force components of the LP source (195 m below ground surface) at t = 40 s. Note how the volumetric source results in more hemispherical wavefronts, whereas the vertical single-force component results in vertically directed energy, and weaker signals at long range.

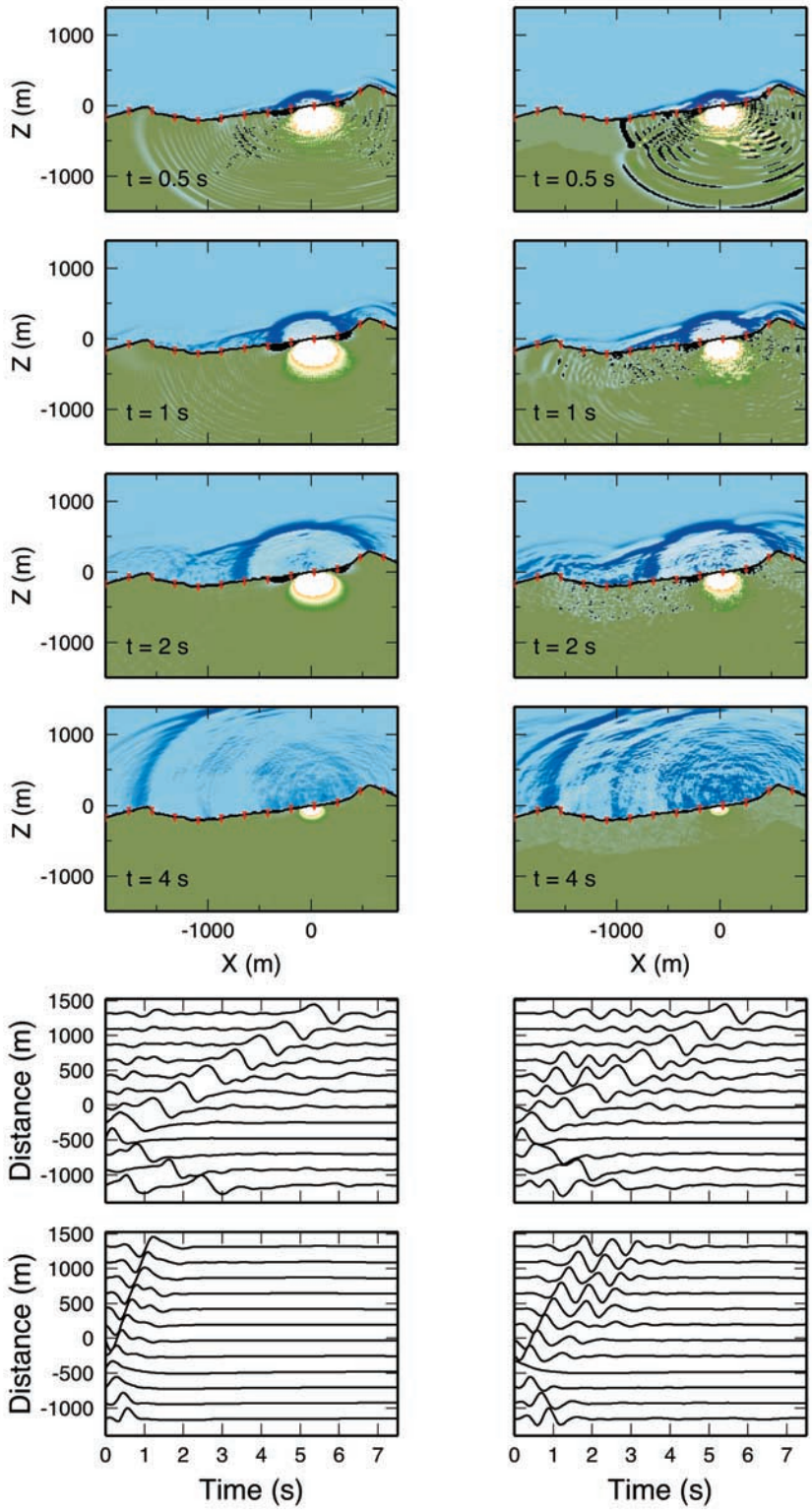

Figure 19. Wavefield snapshots and synthetic record sections for (right) the 2.5-D conceptual weathered layer model compared to (left) a homogeneous solid model. For the 495-m-thick surface weathered layer, V_p = 2000 m/s, V_s = 1155 m/s, and ρ = 2000 kg/m^3; for the homogeneous solid beneath the weathered layer, V_p = 3500 m/s, V_s = 2020 m/s, and ρ = 2650 kg/m^3; and for the atmosphere, V_p = 330 m/s, V_s = 0 m/s, and ρ = 1.2 kg/m^3. (left) (top) From top to bottom, pressure wavefield snapshots at t = 0.5, 1, 2, and 4 s, synthetic acoustic and (bottom) seismic record sections for the homogeneous solid model. (right) Same as Figure 19 (left) but for the weathered layer model. The source is placed at (0, 0, −60) in each case.

vertical single-force component results in energy directed vertically upward, while the volumetric moment tensor components result in more hemispherical wavefronts with a stronger horizontally traveling component.

4.2.4. Long-Duration Source Time Function

[47] Figures 16–18 demonstrate that using a long-duration STF in the ground leads to a long-duration infrasonic waveform in the atmosphere. The seismic-acoustic conversion does not result in an impulsive infrasonic signal from some component of the long-duration seismic source time function. Furthermore, Figures 15–17 show that the amplitudes of the locally radiating P and Rayleigh wave energy should be comparable to that of the energy originating from the source epicenter for this source depth, resulting in even longer-duration and highly complex infrasonic signals. This is at odds with our observations, as we have instead recorded a simple impulsive infrasonic signal, and a more complex, longer-duration seismic LP. This suggests that the impulsive trigger and resonant crack components of the LP event are separated into infrasonic and seismic components at the source by a more complex mechanism not captured in our numerical modeling using a single point source representation (sections 5 and 7.1).

4.2.5. Effects of a Near-Surface Weathered Layer

[48] Here we briefly consider the effects of a near-surface weathered layer on the seismic-acoustic conversion near the source epicenter. A shallow lower velocity layer acts to match the impedance between the subsurface and the overlying atmosphere, having potentially significant effects on the ground-atmosphere wave transmission. Given lack of knowledge of the shallow subsurface materials at MSH, we specified a conceptual 495 m thick weathered layer using nominal values of V_p = 2000 m/s, V_s = 1155 m/s, and ρ = 2000 kg/m^3 [*Virieux*, 1986; *Thelen et al.*, 2009; *Scheu et al.*, 2006]. Figure 19 shows the results of including the weathered layer compared to the homogeneous solid used in previous simulations. These simulations use the 2.5-D geometry, but a smaller subset of the computational volume extending to just 2 km from the source in the x direction. The impulsive isotropic source is at 60 m depth below the surface. The low-impedance layer enhances the amplitude of the air pressure wave by a factor of 5 at 2 km but increases the seismic amplitude in approximately the same proportion, leading to the same P/V_z amplitude ratio. Also, short-lived reverberation in this layer leads to more complex seismic and acoustic signals. The locally converted seismic-acoustic energy contributes more to the waveforms for the weathered layer model.

5. Seismic-Acoustic Conversion From a Shallow Buried, Fluid-Filled Crack

[49] So far our consideration of the airborne acoustic field from a buried, fluid-filled crack has been restricted to frequencies <2 Hz according to the STF obtained by *Waite et al.* [2008]. This STF (Figure 11) captures the resonant coda of the LP waveform but does not adequately include the broadband trigger component initiating the resonance. *Chouet* [1986] calculated waveforms for the normal component of velocity at the wall of a fluid-filled crack resulting from its response to a step function in pressure applied to a small patch of the crack (the ''trigger patch''). The waveforms near the trigger patch have a highly broadband onset with amplitude an order of magnitude higher than the resonance component, resulting from the pressure step function [*Chouet*, 1986]. This high-amplitude broadband trigger component dissipates rapidly in the crack due to radiation into the elastic solid and viscous attenuation in the fluid, such that the resonant fluid response becomes the dominant motion in the crack. Furthermore, once the elastic energy leaves the crack, attenuation in the elastic solid erases more of the higher frequency trigger components. The end result is that far-field seismic LP waveforms have a relatively low-amplitude broadband trigger component, and a dominant resonance component (see Figure 2).

[50] The modeling results of section 4 indicate that infrasonic signals may be generated by seismic-acoustic conversion in the immediate vicinity of the source epicenter. In the epicentral region of a shallow (depth ~200 m) fluid-filled crack, the trigger component of the seismic waveform may still have amplitude an order of magnitude higher than the resonance component, as the attenuation through ~200 m of elastic solid may be negligible. This offers a potential explanation for why the infrasonic signals observed at CDWR are dominantly a record of the broadband trigger, while the seismic waveforms consist primarily of the resonance signal.

[51] However, the broadband trigger component is only an order of magnitude higher in amplitude than the resonance component on a small area of the crack wall close to the trigger patch (see Figure 20). Crack resonance is the dominant motion in the remainder of the crack. Another limitation of our modeling so far has been the restriction to a

Figure 20. Waveforms at the wall of a fluid-filled crack with α/a = 17.5, b/μ = 0.0018, W/L = 0.5, and C = 7.5. (a) Geometry of the fluid-filled crack. Dashed line represents the centerline of the crack in the y direction and is an axis of symmetry exploited in the computation. In this case, the trigger patch (T) is located at the central position along the centerline and extends one grid point in both positive and negative directions along the x axis. (b) Normal component velocity record section along full length of crack centerline in y direction, x = 0 (dashed line in Figure 20a). Arrows indicate position of waveforms shown in Figure 20c. (c) From top to bottom, trace 1, normal component of velocity at the central position of the crack (trigger patch, x = 0, $y = L/2$); trace 2, normal component of velocity at the crack tip (x = 0, $y = L$); trace 3, normal component of displacement at central position of the crack; and trace 4, normal component of displacement at the crack tip. Note that the trigger component of the velocity and displacement waveforms at the location of the trigger patch is an order of magnitude larger in amplitude than the resonance component. At the crack tip ($y = L$), the trigger and resonance components have the same amplitude in the velocity waveform, while the resonance component is dominant in the displacement waveform.

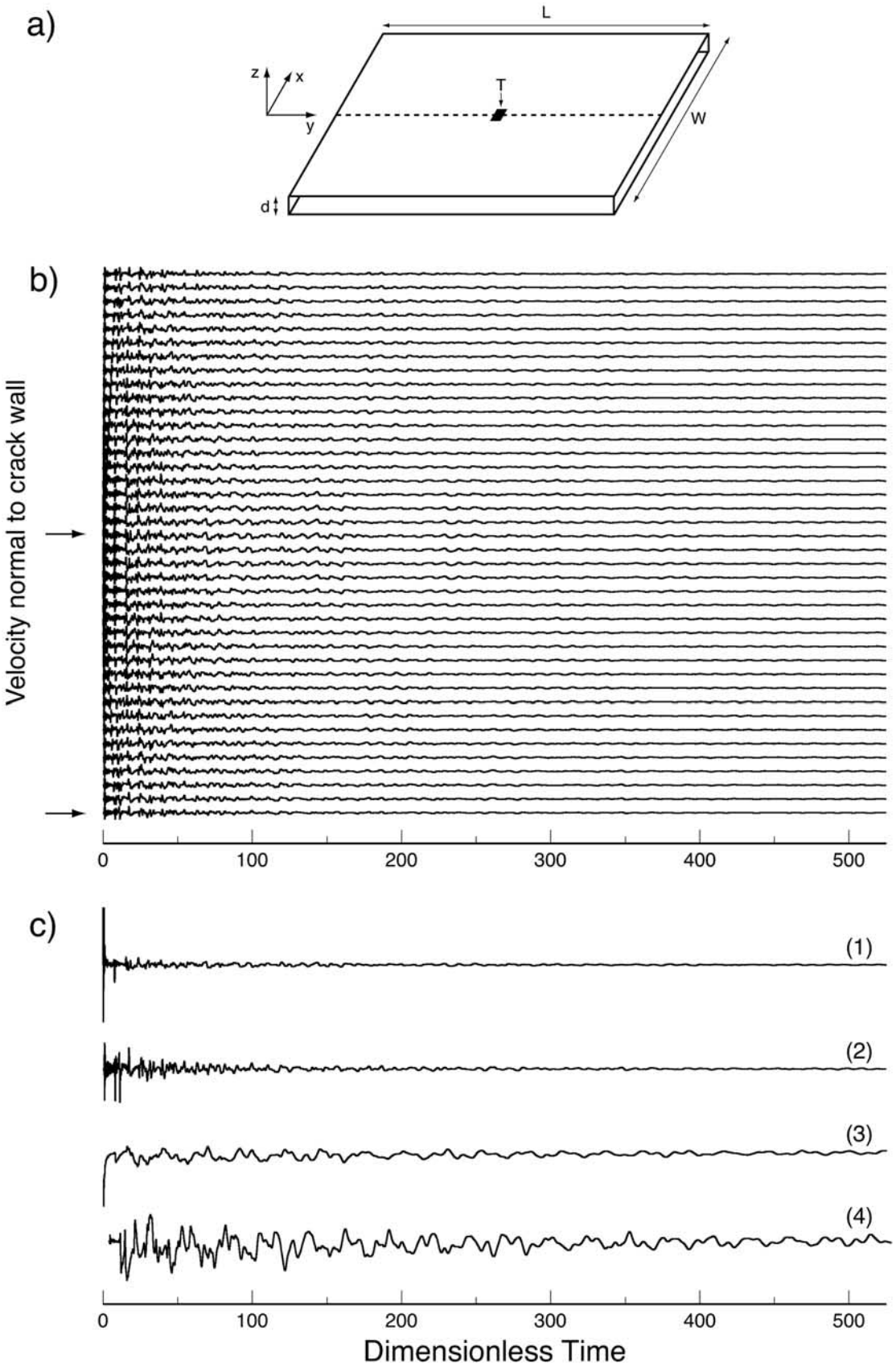
a)
L
z
x
y
T
W
d
b)
Velocity normal to crack wall
0
100
200
300
400
500
c)
(1)
(2)
(3)
(4)
0
100
200
300
400
500
Dimensionless Time

Figure 20

point source representation, where the geometry of the trigger patch with respect to vibrations of the extended crack were not taken into account. The observed infrasonic signals have the majority of their energy in the same frequency band (1–5 Hz) as the observed seismic signals (Figure S1) yet have only a very low amplitude contribution that could be attributed to crack resonance (Figure 9). Thus, for seismic-acoustic coupling to generate the infrasonic signals, and account for the differences in infrasonic and seismic waveforms, the contribution of the small trigger patch on the crack would have to outweigh the net contribution from the remainder of the crack where resonance is the dominant motion. This might be achieved by variations in crater topography across the extent of the crack, which may allow the motion at shallower parts of the crack to couple well into the atmosphere while keeping the remainder of the crack buried deep enough that coupling to the atmosphere is negligible. In this section, we investigate these additional complexities in 2-D by using the finite difference fluid-filled crack code WETC3D of *Chouet* [1986] to generate a distributed line source, which is then input into ASTAROTH [*D'Auria and Martini*, 2007] for calculation of the seismic-infrasonic coupling. A smaller grid spacing is used to allow modeling of frequencies up to 5 Hz, while the effects of trigger patch position, and variations in crater topography above the extended line source are considered.

5.1. Model Configuration

5.1.1. Acoustic Properties of the Fluid-Filled Crack

[52] The fluid-filled crack is specified by the parameters α/a, b/μ, W/L, and the crack stiffness:

$$C = \frac{bL}{\mu d}, \tag{3}$$

where $\alpha = V_p$ is the P wave velocity of the elastic solid, μ is the shear modulus of the elastic solid, a is the sound speed of the fluid in the crack, b is the bulk modulus of this fluid, and L, W, and d, are the length, width, and aperture of the crack, respectively [*Chouet*, 1986]. Assuming a Poisson solid ($\lambda = \mu$), the ratios α/a and b/μ are related to the density of the fluid ρ_f and density of the solid ρ_s by

$$\frac{\rho_f}{\rho_s} = \left(\frac{\alpha}{a}\right)^2 \left(\frac{b}{3\mu}\right). \tag{4}$$

For the solid, we use $\alpha = 3500$ m/s and $\rho_s = 2650$ kg/m^3 as in section 4, which fixes μ to ~10 GPa. For the crack dimensions we assume $L = 200$ m, $W = 100$ m, and $d = 5$ cm as postulated by *Waite et al.* [2008]. The acoustic properties of the fluid are given values of $a = 200$ m/s and $\rho_f = 500$ kg/m^3, corresponding to a water-steam foam at a pressure of 5 MPa (lithostatic pressure for the shallow source depth of ~200 m) and temperature $T = 537$ K [*Kumagai and Chouet*, 2000]. Accordingly, the model fluid-filled crack is specified by $\alpha/a = 17.5$, $b/\mu = 0.0018$, $W/L = 0.5$, and $C = 7.5$.

5.1.2. Waveforms at the Wall of the Fluid-Filled Crack

[53] Since we are interested in the contribution of the broadband trigger component to infrasonic waveforms in the band 1–5 Hz, our modeling in this section includes frequencies up to 5 Hz. The finite difference calculations for the fluid-filled crack were performed for a physical grid spacing of 5 m, satisfying the minimum of five grid points per smallest wavelength (based on $a = 200$ m/s) required for stability in WETC3D. Time stepping was performed until $t = 30$ s to capture the long-duration oscillations of the crack.

[54] Figure 20 shows waveforms at the wall of the fluid-filled crack in the y direction along the centerline of the crack, $x = 0$ (dashed line in Figure 20a), where a trigger patch is located at the center of the crack ($x = 0$, $y = L/2$). Velocity and displacement waveforms at the trigger patch (center of the crack) have trigger components with amplitude an order of magnitude higher than the resonance component (Figure 20c, curves 1 and 3). In contrast, velocity and displacement waveforms at the crack tip have a much weaker contribution from the trigger, and the resonance component is more dominant here (Figure 20c, curves 2 and 4).

5.1.3. Moment Tensor Representation of the Crack

[55] The moment tensor for the volumetric opening of a horizontal crack is given by

$$\boldsymbol{M} = \Delta V \begin{pmatrix} \lambda & 0 & 0 \\ 0 & \lambda & 0 \\ 0 & 0 & \lambda + 2\mu \end{pmatrix}, \tag{5}$$

where $\boldsymbol{M}$ is the moment tensor, ΔV is the volume change, and λ, μ are the Lamé parameters [*Chouet*, 1996b]. For a horizontal crack in a Poisson solid ($\lambda = \mu$), the time-dependent moment tensor is therefore given by

$$\boldsymbol{M}(t) = 2\mu LWu(t) \begin{pmatrix} 1 & 0 & 0 \\ 0 & 1 & 0 \\ 0 & 0 & 3 \end{pmatrix}, \tag{6}$$

where $\mathbf{M}(t)$ is the moment tensor as a function of time, L and W are the length and width of the crack, and $u(t)$ is the normal component of displacement at the crack wall; $u(t)$ was obtained by a cumulative integral of the normal component of velocity at the crack wall using the trapezium rule. Note that the factor of 2 comes from the full opening of the crack with two opposite walls. The time and velocity output from WETC3D were converted to dimensional form using the relations:

$$v(t) = \left(\frac{4n\alpha\Delta P}{\mu}\right) v'(t) \tag{7}$$

$$dt = \left(\frac{L}{\alpha}\right) dt', \tag{8}$$

where n is the number of grid points used to discretize the length of the crack ($n = 40$), ΔP is the magnitude of pressure step applied at the trigger patch ($= 1 \times 10^5$ Pa), and primed quantities represent nondimensional form in WETC3D.

[56] The extended line source in 2-D is represented by a series of 40 point sources sampling the crack centerline (Figure 20b). Each point source has the moment tensor

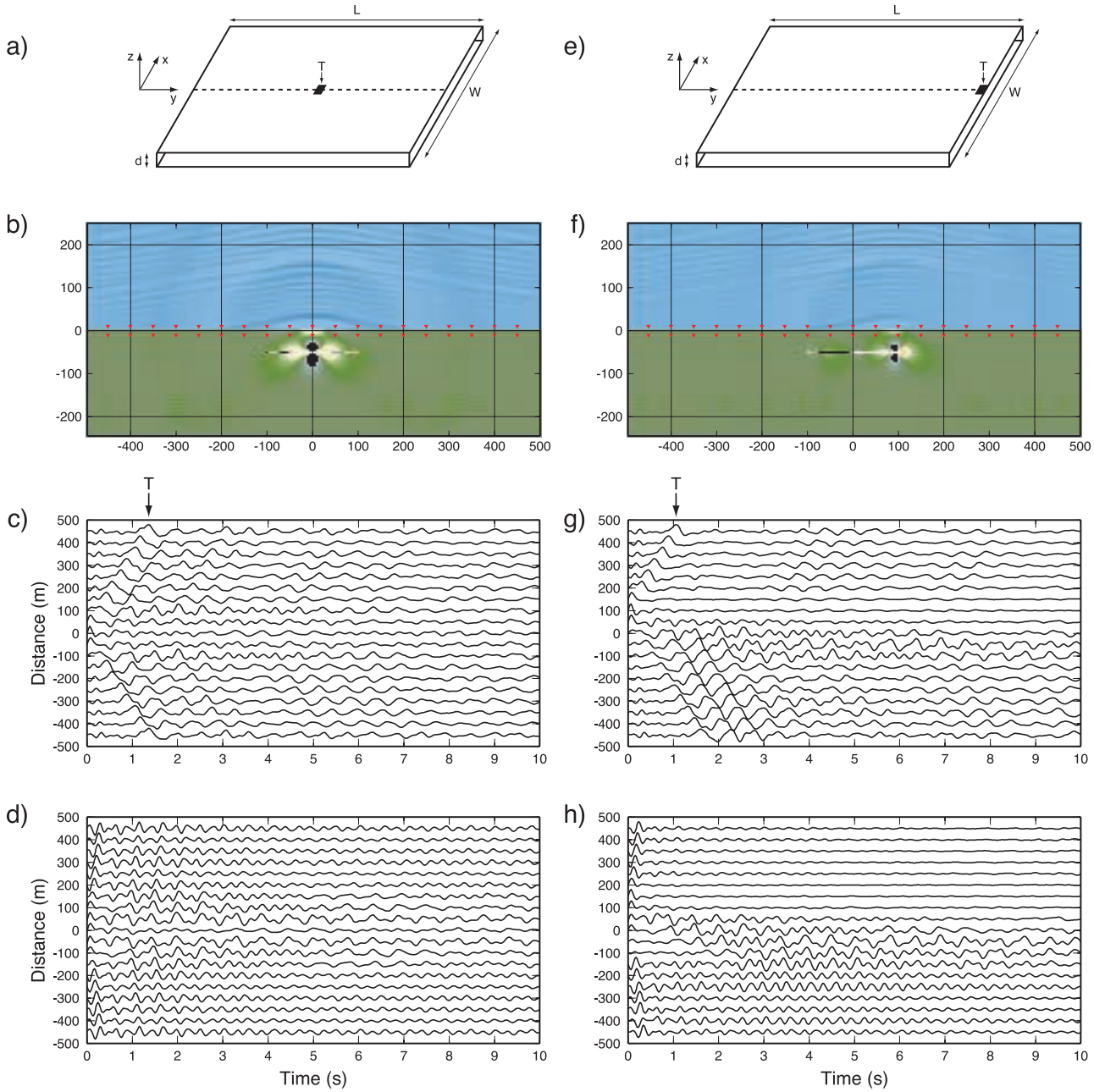

Figure 21. Seismo-acoustic wavefield from a fluid-filled crack buried at 50 m depth in a homogeneous elastic half-space, overlain by a homogeneous atmosphere. (a) Geometry of the fluid-filled crack for the simulation results shown in Figures 21b–21d. In this run, the trigger patch is located at the crack center. (b) Pressure wavefield snapshot at $t = 1$ s for the crack geometry of Figure 21a centered at (0, −50). Position of synthetic sensors is indicated by red inverted triangles. (c) Pressure record section for sensors in the atmosphere layer. The acoustic arrival corresponding to the trigger component of the LP source is indicated by a "T," all subsequent waveform features correspond to the 'resonance' component. (d) Vertical component velocity record section for sensors in the elastic layer. Note that the resonance component dominates the velocity waveforms. (e–h) Same as Figures 21a–21d but for a trigger patch located at the crack tip. Note the asymmetry in the wavefield for this source configuration (Figures 21f and 21g). The trigger component is dominant in pressure waveforms to the right-hand side of the crack, while the resonance component is dominant to the left-hand side of the crack.

representation of equation (6), with the appropriate function $u(t)$ corresponding to that location on the crack, length element $L = 5$ m, and width $W = 100$ m corresponding to the entire width of the crack. The difference in source depth (∼18 m) along the ∼200 m length of a crack dipping ∼5° as postulated by *Waite et al.* [2008] is small, justifying our assumption of a horizontal crack in these calculations.

5.1.4. Geometry of the Seismo-Acoustic Medium

[57] In each case, the geometry of the seismo-acoustic medium in ASTAROTH is 2-D, extending 1 km in the y direction and 500 m in the z direction. The solid is homogeneous with V_p = 3500 m/s, V_s = 2020 m/s, and ρ_s = 2650 kg/m^3, and is overlain by a homogeneous atmosphere with V_p = 330 m/s, V_s = 0 m/s, and ρ_a = 1.2 kg/m^3. As in WETC3D, a physical grid spacing of 5 m was used in ASTAROTH, therefore avoiding spatial aliasing problems. Time stepping was performed until t = 10 s, enough to compare the contribution from the initial trigger component (t < 0.5 s, see Figures 20 and 21) to the resonance component of the STF (t > 0.5 s). We note that the instantaneous pressure-step function used in WETC3D produces a very short duration trigger component (<0.5 s) with amplitude an order of magnitude higher than the resonance component. In reality, the trigger may be longer in duration, and the model results would be convolved with this longer-duration trigger STF. However, the short-duration trigger is more practical for investigating trigger-resonance separation with shorter computations. The first set of runs (Figure 21) correspond to flat topography, while the second set of runs include variations in crater topography above the shallow buried crack (Figure 22 and Table 1).

5.2. Results

5.2.1. Crack in a Homogeneous Half-Space

[58] Figure 21 shows the results for a crack line source buried in a homogeneous elastic half-space. In Figures 21a–21d the trigger patch is located at the crack center, while in Figures 21e–21h the trigger patch is located at the crack tip. In both cases, the horizontal crack is placed at 50 m depth below the ground surface. As seen in Figures 21c and 21g, seismic-acoustic conversion takes place near the epicenter of the trigger patch, resulting in propagation of the trigger signal through the atmosphere at acoustic velocity ("T"in Figures 21c and 21g). However, for a trigger patch located at the crack center, this energy is focused in the vertical direction (Figure 21b), and the acoustic waveforms at ground level consist of a trigger and resonance component with approximately the same amplitude except directly above the crack (Figure 21c). For a trigger patch at the crack tip, horizontal source directionality is observed. Pressure waveforms to the right of the crack (y > 100 m) in Figure 21f have a stronger trigger component than resonance component, while waveforms to the left of the crack (y < −100 m) are dominated by the resonance component (Figure 21g). However, the amplitude ratio of trigger to resonance component for y > 100 m is only ∼2, not the order of magnitude required to explain the observed signals (Figures 2 and 9b). In additional calculations not presented here, we increased the size of the trigger patch and found that this resulted in stronger resonance of the crack, and a reduction in the amplitude ratio of trigger to resonance components for the atmospheric signals. Although limited to a 2-D geometry, these calculations suggest that the contribution of the trigger patch cannot outweigh the net contribution of the resonance component for a horizontal crack buried in a homogeneous elastic half-space. Remaining possible ways to enhance the trigger component in the atmosphere relative to the resonance component are variable topography over the crack, or a localized increase in acoustic transmission immediately above the trigger patch by permeable/porous material. In section 5.2.2, we investigate the role of variable topography above the crack.

5.2.2. Crack Overlain by Variable Topography

[59] Figure 22a shows a 5 m interpolated DEM of the southern April 2005 crater [*Schilling et al.*, 2009]. In this region, the crater wall and 2005 lava dome have the greatest topographic gradients. Accordingly, we sample two profiles along (P1) and across (P2) the 2005 lava dome, extending to the south crater wall. The fluid-filled crack source with trigger patch at the crack tip (see section 5.2.1) is located directly beneath the 2005 lava dome, with the trigger patch located 30 m below the topography surface at that location (Figures 22b and 22e). The acoustic signal resulting from this source for profile P1 has a trigger-resonance amplitude ratio of ∼3 for profile P1 (Figure 22c). For profile P2, the acoustic trigger amplitude is about the same as the resonance amplitude (Figure 22f), even though the topography gradient is stronger along the length of the crack for P2. The reason for this is that P2 includes strong gradients in topography in the immediate vicinity of the trigger epicenter, while P1 has relatively flat topography in the vicinity of the trigger epicenter. This indicates that not only is crater topography important for controlling variable seismic-acoustic coupling along the length of a shallow crack in a homogeneous elastic medium, but the topography structure in the immediate vicinity of the source epicenter is also critical for effective infrasound generation.

[60] In a separate calculation, we found that decreasing the depth of the crack to 15 m below the topography surface at the trigger patch increased the acoustic trigger-resonance amplitude ratio by a factor of 2, still too small to explain the observed signals (Figure 2 and Figure 9). This indicates that an extremely shallow trigger source (<10 m) would be required to explain the observed signals by simple elastodynamic coupling in homogeneous media. For the LP source depth of ∼200 m obtained by *Waite et al.* [2008], simple elastodynamic coupling is therefore not a feasible source for the observed infrasonic signals. For a crack at a depth ∼200 m, variations in topography above the crack would be negligible (see Figures 22b and 22e) and would not cause separation of the trigger and resonance components in the acoustic pressure waves. The shallowest materials in the 2004–2005 crater of Mount St. Helens most likely consisted of a lava dome complex made up of core blocks of dense dacite with large-scale fractures, covered by a loosely consolidated talus pile, and partially by glacier ice [*Cashman et al.*, 2009; *Pallister et al.*, 2009; *Schilling et al.*, 2009; *Vallance et al.*, 2009]. Since our models indicate that an extremely shallow source is required, this implies that the trigger would be located within this material (see section 7.1).

6. Atmospheric Propagation Effects and Signal Intermittency

[61] The most significant time-dependent factors influencing sound propagation outdoors are (1) refraction from vertical gradients in temperature and wind, (2) classical and molecular absorption (dependent on temperature, ambient pressure, and relative humidity), (3) effects of the ground impedance (affected by snow cover and vegetation), and (4) scattering from turbulence [*Reynolds*, 1873; *Piercy et al.*,

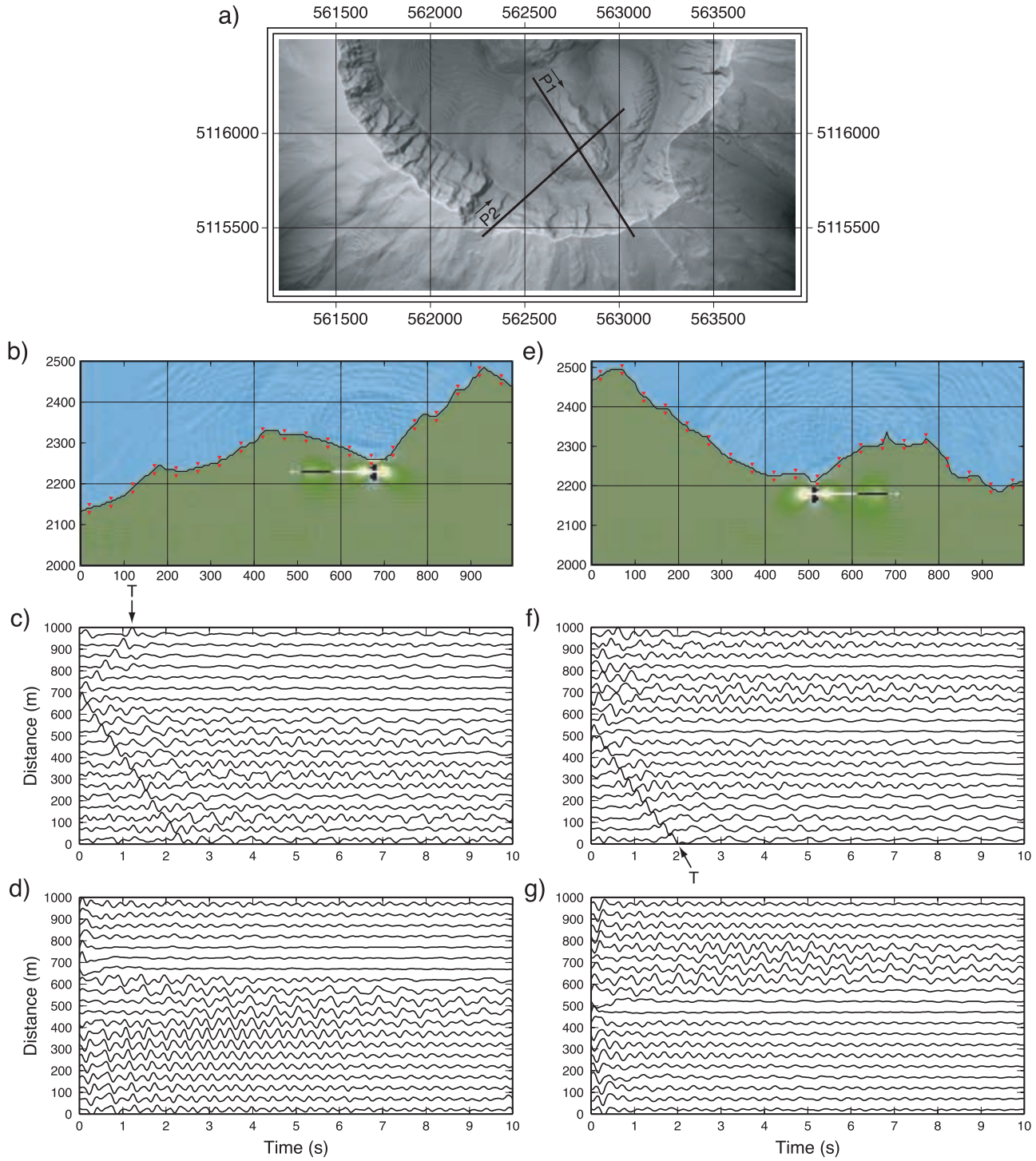

Figure 22. Seismo-acoustic wavefield from a fluid-filled crack buried shallow beneath variable crater topography. (a) Location of topography profiles within the crater of April 2005 [*Schilling et al.*, 2009]. Profile P1 runs approximately NW–SE along the 2005 lava dome, while profile P2 runs approximately SW–NE across the 2005 lava dome. In each case, the centerline y axis of the fluid-filled crack is oriented along the profile, with the trigger patch at the crack tip underneath the shallowest point in topography (Figures 22b and 22e). (b) Pressure wavefield snapshot at $t = 1$ s for a fluid-filled crack with trigger at the crack tip underneath topography profile P1. Red inverted triangles indicate position of synthetic sensors. (c) Acoustic pressure record section for profile P1. The acoustic arrival corresponding to the trigger is indicated by a "T." (d) Vertical component velocity record section for profile P1. (e–g) Same as Figures 22b–22d but for profile P2. In each case, the crack is located such that the trigger patch at the crack tip is the shallowest point on the crack, located 30 m below the surface. The remainder of the crack is buried beneath the deeper variable topography of the 2005 lava dome.

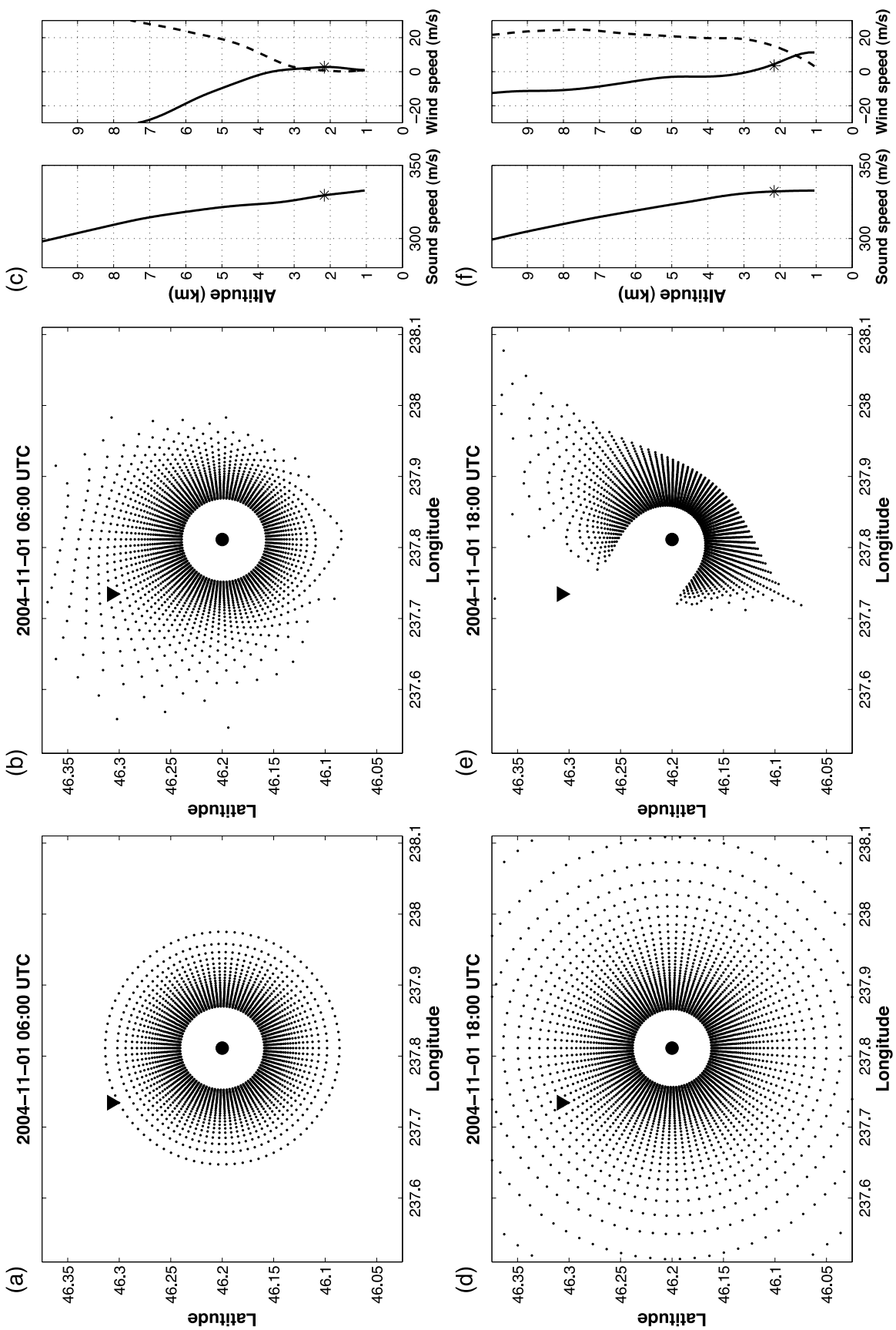
(a)
(b)
(c)
(d)
(e)
(f)
2004–11–01 06:00 UTC
2004–11–01 18:00 UTC
Latitude
Longitude
Altitude (km)
Sound speed (m/s)
Wind speed (m/s)

Figure 23

1977; *Larsson and Israelsson*, 1991; *Embleton*, 1996; *Ostashev*, 1997]. Fortunately, infrasonic propagation for the frequencies and range (13.4 km) we consider in this study is much simpler: absorption is negligible [*Sutherland and Bass*, 2004], the surface impedance is very large such that very little energy is lost to the ground surface [*Bass*, 1991], and turbulence is typically disregarded. Therefore, to a first order, infrasonic propagation is governed by horizontal stratification in temperature and wind, while turbulence may result in additional fluctuations in signal amplitude and phase. Temperature affects the adiabatic or static sound speed as

$$c = \sqrt{\frac{\gamma RT}{M}}, \tag{9}$$

where c is the sound speed, $\gamma = c_p/c_v$ the ratio of specific heats, R is the molar gas constant, T is the absolute temperature, and M is the molar mass of air. Wind advects the acoustic fluid (see equation (2)), resulting in spatially dependent changes in the propagation speed. The infrasonic propagation between MSH and CDWR is confined to the atmospheric boundary layer and is therefore controlled by mesoscale and microscale meteorology.

[62] Ray theory applied to temperature lapse or upwind propagation results in upward refraction and the formation of a shadow zone, while temperature inversion or downwind propagation result in downward refraction and clear signal reception [*Piercy et al.*, 1977]. Thus, ordinary lapse conditions or northwesterly winds would put CDWR in a shadow zone of MSH according to ray theory. However, ray theory is an infinitely high-frequency approximation and begins to fail for infrasonic frequencies where the wavelength approaches the scale lengths of the temperature and wind gradients. Refraction occurs but at much longer ranges [*Piercy et al.*, 1977], and diffraction (creeping waves) and scattering from turbulence fill in the shadow zones [*Bass*, 1991]. This said, *Fee and Garcés* [2007] reported diurnal variations in infrasonic tremor amplitude at a range of 12.5 km from Pu‘u O‘o, Hawaii, well correlated with the formation and break up of a nocturnal boundary layer. Although the variations are not dominantly diurnal in our data (Figure S3), nondiurnal boundary layer dynamics are the likely cause of signal intermittency. The amplitudes of the infrasonic LP signals we consider in this study (Figure 4) are comparable to the amplitudes of infrasonic tremor discussed by *Fee and Garcés* [2007] and are very low in comparison to other volcano-acoustic signals [*Garcés et al.*, 2008]. Thus atmospheric propagation effects are far more noticeable for LPs than for large-amplitude eruption signals that appear to fill in the shadow zones [*Garcés et al.*, 2008]. In this section, we briefly compare ray tracing and 2-D finite difference simulations of infrasonic propagation between MSH and CDWR. The finite difference approach gives a more complete description of wave propagation, enabling more accurate predictions of the sound field at low frequencies.

6.1. Ray Tracing

[63] We performed ray tracing using the approach of *Garcés et al.* [1998] using ground to space (G2S) semiempirical atmospheric specifications for the study region [*Drob et al.*, 2003]. The G2S profiles have a horizontal resolution of $\sim 1^\circ \times 1^\circ$, a vertical resolution of 200 m, and a temporal resolution of 6 h. They, therefore, lack the finer mesoscale structure required to fully resolve atmospheric propagation at this scale. Nevertheless, G2S does provide physically realizable wind and temperature profiles that are useful for assessing the effects of typical atmospheric variability.

[64] Movie S2 shows a plan view of tropospheric ray first-bounce points from a source just above the elevation of the LP source for the time period 1–16 November 2004. Rays are shot in 4° increments azimuthally and 0.25° increments for the grazing angle (angle from horizontal, positive upward). Topography has been neglected, but rays have been limited to a grazing angle of $>-15^\circ$, the approximate slope of the mountain along our profile (Figure 10). Multiple ground bounces are not permitted. Fluctuation in the spatial position of ray first-bounce points is seen. Ray bounce points extend to CDWR at certain times (e.g., 0600 UTC, 10 November 2004) predicting clear signal reception, and at other times do not (e.g., 1800 UTC, 1 November 2004), predicting CDWR is in a shadow zone and loss of signal reception. We note that these time predictions for signal loss do not match our data, indicating that the G2S atmospheric models are not sufficiently accurate at the 10 km lateral scale.

[65] The importance of wind for the ray predictions is illustrated in Figure 23. Here the spatial distribution of first-bounce points for two representative time periods are shown with and without including advection due to wind. In Figure 23a, ray coverage does not extend to CDWR when wind is neglected, but does when wind is included (Figure 23b). In Figure 23d, rays do extend to CDWR without wind, but form a clear shadow zone when wind is included (Figure 23e). This can be understood by reference to the wind profiles (Figures 23c and 23f). While relatively little difference exists in the static sound speed due to temperature, the winds for the case shown in Figure 23b have a southeasterly component at the source altitude (winds blowing from MSH toward CDWR) and for the case shown in Figure 23e have a strong northwesterly component (winds blowing from CDWR toward MSH), generating a shadow zone due to upwind propagation.

Figure 23. Coordinates of ray first-bounce points predicted with the G2S model. The source location (altitude 2.2 km, star in Figures 23c and 23f) at MSH is indicated by a solid dot; CDWR location is indicated by an inverted triangle. In the dotted area, clear direct signal reception is predicted, while other regions represent shadow zones where rays refract upward before reaching the ground. (a) G2S model for 0600 UTC, 1 November 2004 with effects of wind neglected. (b) Same as Figure 23a but wind included. (c) static sound speed and wind speed profiles for G2S model 0600 UTC, 1 November 2004; solid line, meridional winds (N–S); dashed line, zonal winds (E–W). (d) Model for 1800 UTC, 1 November 2004 without wind. (e) Same as Figure 23d but with wind. (f) Same as Figure 23c but for 1800 UTC, 1 November 2004. For a longer time sequence of ray predictions, see Movie S2.

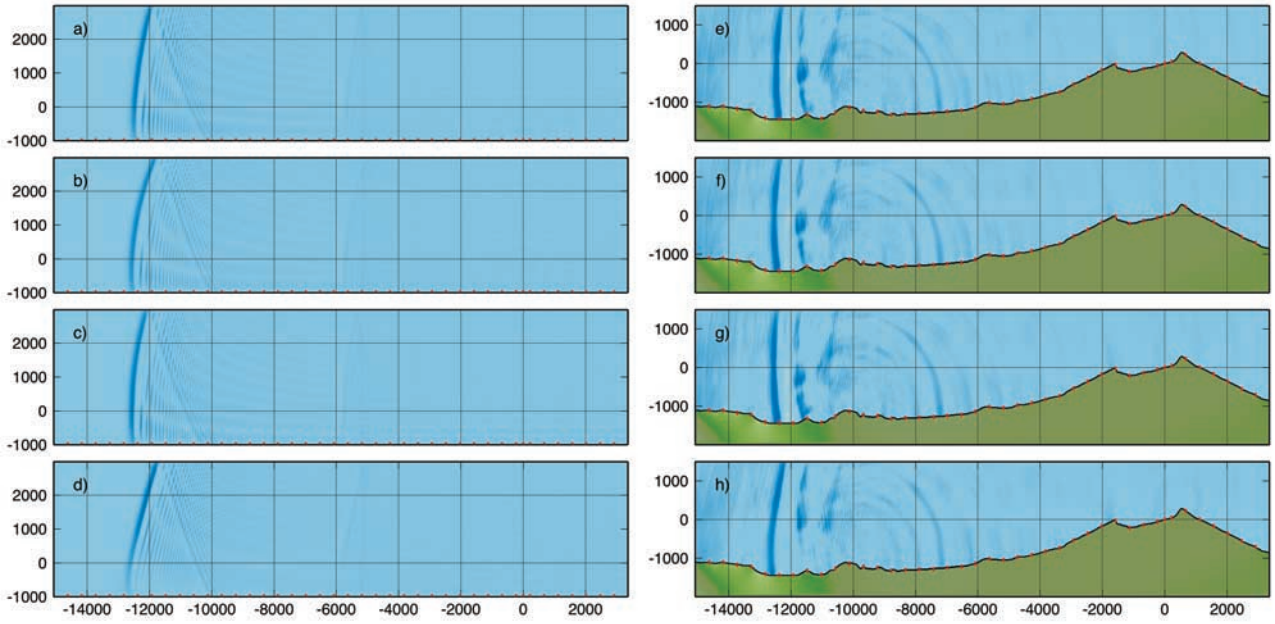

Figure 24. A 2-D FD simulation of the four atmospheric cases shown in Figure 23, with and without topography. All images are pressure wavefield snapshots at t = 38 s. (a) G2S model for 0600 UTC, 1 November 2004 with effects of wind neglected. (b) Same as Figure 24a but in-profile wind included. (c) G2S model for 1800 UTC, 1 November 2004 with effects of wind neglected. (d) Same as Figure 24c but in-profile wind included. (e)–(h) Same as Figures 24a–24d but source is buried at 60 m depth in elastic topography. Note the difference in vertical scales for Figures 24a–24d versus Figures 24e–24h. In all cases, the effects of wind and temperature gradients are less pronounced than in the infinite-frequency ray approximation, with only slight steepening and gradual refraction of wavefronts. In contrast, the ray results of Figure 23 predict a full shadow zone for the case shown here as Figures 24d and 24h. The effects of wind are evident as in Figure 24d, where upturning of the wavefront, and weaker amplitude near the base of the model are observed. However, the simulations (Figures 24e–24h) show less sensitivity to the atmospheric conditions, suggesting that scattering from topography may be important for filling in the infrasonic shadow zone.

6.2. Finite Differences

[66] Figure 24 shows the results of 2-D finite difference (FD) simulations for the four atmospheric cases shown in Figure 23, with and without elastic ground topography. Where topography is neglected (Figures 24a–24d), the source altitude is the same as in the ray simulations of Figure 23 and all boundary conditions are absorbing (no reflections from the ground), allowing for a direct comparison of ray tracing and FD methods. Where topography is included (Figures 24e–24h), the source is buried at a depth of 60 m within the volcano. In each case we also included a more realistic density profile for the atmosphere modeled as

$$\rho(z) = \rho_0 e^{-0.000146(z-z_0)}$$

where ρ_0 = 1.04 kg/m^3 at $z_0 = -1100$ m in our coordinate system. Although the 2-D geometry does not include the geometrical spreading loss, it models the wavefield structure, which is more directly comparable to the ray results of Figure 23.

[67] All simulations in Figure 24 show less pronounced effects of vertical wind and temperature gradients than the ray simulations of Figure 23. Rather than sharp refraction and the formation of clear shadow zones, the gradients result in a slight steepening and gradual upward turning of the wavefronts, with significant energy diffracting down into the ray shadow zones. The simulations neglecting wind (Figures 24a, 24c, 24e, and 24g) are barely distinguishable from one another, while the simulations including wind (Figures 24b, 24d, 24f, and 24h) show more pronounced differences. This is in agreement with the prediction of Figure 23 that wind has more significant effect on acoustic propagation at this scale than vertical temperature gradients. As in Figure 23e, the most significant effects are seen in Figure 24d, with the G2S model for 1800 UTC, 1 November 2004 with wind included. In Figure 23e a full shadow zone for CDWR is predicted, while in Figure 24d some weak upward refraction results in a predicted lower amplitude at CDWR (energy weaker along wavefront below z = 0 km), but not the complete loss of signal. Thus, the ray and FD results are in qualitative agreement about which are the more dominant atmospheric effects on propagation (i.e., winds blowing receiver-source), but rays are overly sensitive to these gradients and predict full signal loss where FD predicts significant energy.

[68] Further differences are seen in the simulations including elastic topography and a buried source (Figures 24e–24h). Here, the effects of refraction are even less pronounced than in the simulations without topography (Figures 24a–24d). In particular, the energy loss predicted at a ground-

based receiver at 13 km in Figure 24h is much lower than that seen in Figure 24d for the same atmospheric conditions. This suggests that scattering by topography may be important for diffracting energy into shadow zones at this scale. In a separate set of simulations, we experimented with adding a thin (400 m) temperature inversion layer mantling the topography. We found that this also had no effect on the predicted infrasonic wavefield, suggesting that wind and perhaps turbulence are the dominating factors.

7. Discussion

7.1. Source Process

[69] The measured lower bound on the modal amplitude ratio (P/V_z) of 1.3×10^4 Pa s/m at CDWR (Figure 4) cannot be reproduced by the simple elastodynamic processes we have considered. For the shallowest source possible in our modeling, the predicted P/V_z is an order of magnitude lower than this, while the predicted P/V_z ratios from the point source description and location from *Waite et al.* [2008] are lower still. The observed P/V_z of 5.3×10^3 Pa s/m at BLIS is also at odds with the numerical predictions from a buried source, as the P/V_z is found in the models to be higher closer to the source. We also found that the addition of a laterally continuous near-surface weathered layer with lower impedance cannot reproduce the amplitude ratio, as the seismic amplitude in the layer increases in proportion to the amplitude of the pressure wave. However, additional complexities not considered in our modeling may affect the amplitude ratio. As discussed in sections 4.1.2 and 6, energy focusing by a wind direction bias may lead to an increase in observed P/V_z. In addition, a low-impedance layer local to the source region would enhance infrasonic energy transmission in the vicinity of the source epicenter, without increasing seismic amplitudes at long range. Furthermore, our velocity-stress governing equations do not include nonlinear material effects such as tensile failure or spalling of near-surface layers that can be important for shallow buried sources [*Stump*, 1985], nor do they include the effects of porosity and permeability of the near-surface materials [*Sabatier et al.*, 1986; *Hickey and Sabatier*, 1997]. In particular, *Bass et al.* [1980] showed that the transmission coefficient at the ground surface for acoustic energy in the 20–300 Hz band cannot be fully described by the impedance ratio of the materials. The transmission coefficient can be at least an order of magnitude higher (up to 3 orders of magnitude higher) when permeability and airflow through pore volumes is considered. Allowing for the presence of fractures and loosely consolidated material [*Cashman et al.*, 2009; *Pallister et al.*, 2009], the permeability increases substantially. Therefore, on the basis of amplitude considerations alone, we can rule out the possibility of a deep source generating the infrasonic signals, but we cannot distinguish between a surface source venting directly to the atmosphere, and a shallow source (e.g., the ~200 m deep source of *Waite et al.* [2008]) buried in a near-surface layer of highly fractured, porous and permeable material. In addition, we find little evidence in our data for seismic-acoustic energy converted locally along the propagation path and arriving coincident on the microbarometer and seismic records (i.e., pressure waves in the atmosphere with seismic horizontal velocity). Our numerical results indicate that these should be a prominent feature for a source buried in a homogeneous elastic medium. By allowing for high permeability and low impedance of near-surface material above the source, the acoustic energy radiating from the source epicenter may potentially dominate in amplitude over the locally converted seismic energy at ranges of ~10 km. However, while the amplitude ratios are sensitive to several factors not included in our modeling, the observed characteristic differences in waveforms and spectra (Figures 2, 3, and 9) are more robust indicators of source properties.

[70] The observed waveforms and spectra (Figures 2 and 3) are very difficult to reconcile with a common source time function. The infrasonic signals are characterized by short-lived (~5–10 s) broadband pulses, while the seismic signals are characterized by ~5–10 s broadband pulses followed by a long-duration (>50 s) resonant coda. The resonant coda is not prominent in the infrasonic records, but a very weak long-duration signal is found to underlie the infrasonic records (Figure 9). Impulsive acoustic signals in the atmosphere are often observed to generate longer-duration seismic vibrations by air-ground coupling, and these can be modeled in terms of the seismic frequency response of a near-surface layered structure to the impulsive acoustic driving function [*Sabatier and Raspet*, 1988]. However, if a common source time function is assumed in our study, we have the opposite of this scenario, with a longer-duration resonant seismic source time function apparently producing an impulsive broadband acoustic signal in the atmosphere. Such a process is unlikely, and not supported by the results of sections 4.2.4 and 4.2.5.

[71] Putting this together, a more complex integrated source process is required: one consisting of an impulsive STF for the infrasound signal, and an impulsive signal plus resonance component for the seismic signal. In other words, the infrasound signal is a record of the impulsive pressure excitation mechanism or trigger mechanism of the long-period event, while the seismic signal consists of the superposition of the trigger and fluid response (crack waves). Since the broadband pulse has much stronger coupling to the atmosphere than the resonant coda, a mechanism is required for energy partitioning of the trigger and resonance components at the source.

[72] In section 5, we investigated whether variable crater topography above an extended fluid-filled crack source could provide a viable mechanism for partitioning of trigger and resonance components. We found that a trigger patch located <10 m below the topography surface, connected to an extended fluid-filled crack buried at greater depth below a mound of crater topography such as a lava dome, would result in atmospheric acoustic signals that are enriched in the trigger component relative to the resonance component. However, the source depth required for topography to be important is extremely shallow, and requires the trigger patch to be located effectively at the surface. The trigger component from a crack buried at ~200 m depth would not be isolated from the resonant component by the effect of topography alone. This leads to the conclusion that while crater topography may play a role for a very shallow crack source, the influence of porosity and permeability of the shallowest materials is inescapable. We note that strong coupling of the fluid-filled crack into the elastic solid is

required for effective seismic LP signal generation. Therefore, a very shallow, horizontal crack located near the surface exclusively in loosely consolidated material, is an unlikely source for the seismic LP signals. A buried crack that is well coupled to the elastic solid, but venting at its tip into loosely consolidated material, is a reasonable source for both seismic and infrasonic waveforms. Vertical and lateral heterogeneity in crater materials therefore seem necessary for separating the trigger and resonance components from an extended source.

[73] As proposed by *Waite et al.* [2008], the loss of pressure in a shallow hydrothermal crack is a feasible source for both infrasonic and seismic LP events at Mount St. Helens. Sudden, seismogenic loss of steam pressure requires a sudden opening of a pathway to allow the steam to escape. This opening is analogous to the opening of a valve, and the pressure signal resulting from this sudden pressure change, in addition to the rapid flow of gas accompanying this process, would be a significant source of infrasound. The jetting from such a source may be highly localized, perhaps involving a small patch of crack wall with a length scale of ~10 m on the 100 m × 200 m crack postulated by *Waite et al.* [2008], and in this case would result in higher-frequency signals than those recorded. However, although the jetting may not be the dominant source of infrasound for LPs, the gas velocity would increase the total gas volume flux, and enhance the amplitude of the resultant acoustic signal [*Lighthill*, 2001]. If gas vents into a network of open pathways within the dome material, efficient acoustic coupling into the atmosphere is possible. Conversely, crack vibration radiates elastic energy into the solid, so this component dominates the seismic waveforms.

[74] The periodic occurrence of drumbeat LPs can be explained conceptually by a cycle of pressure build up, the reaching of a critical pressure threshold for the valve, and the catastrophic opening of the valve which initiates rapid pressure loss (infrasound signal), collapse of the crack, and attendant resonant response of the fluid remaining in the crack (seismic LP signal). Once pressure is lost, lithostatic pressure reseals the valve and the next cycle of pressure recharge begins. A similar model was proposed by *Ohminato* [2006] to explain periodic VLP and high-frequency pulses associated with the hydrothermal system at Satsuma-Iwojima volcano, Japan. *Ohminato* [2006] also suggested that water contained in a crack in a superheated state might suddenly vaporize, providing an explanation for the sudden surge of pressure in the crack and the opening of the valve. However, in our case the pressure release valve is close enough to the surface to generate infrasound.

[75] Periodic, rapid discharge of gas in association with seismic LP and VLP activity has been observed at numerous other volcanoes [e.g., *Gil Cruz and Chouet*, 1997; *Neuberg et al.*, 2000; *Chouet et al.*, 2005], and has also been associated with infrasound radiation when infrasonic sensors were deployed [*Yamasato*, 1998; *Yamasato et al.*, 2002; *Petersen and McNutt*, 2007]. In the crater of Galeras volcano, Colombia, *Gil Cruz and Chouet* [1997] photographed explosive gas emissions along a crack bisecting the dome (120–150 m long and a few millimeters wide) that were correlated with recorded LP events. *Neuberg et al.* [2000] reported jets of steam and ash accompanying LP events at Soufrière Hills volcano, Montserrat, recorded on synchronized seismic and video data, suggesting that the LP source was somehow linked to gas venting.

[76] However, the 2004–2008 eruption of Mount St. Helens was characterized by low magmatic gas emissions [*Gerlach et al.*, 2009], with relatively low levels of steady steam effusion leaking from cracks and openings in the lava dome [*Vallance et al.*, 2009]. No periodic gas release was observed. The near-surface materials above the LP source most likely consisted of fractured blocks of dacite, loosely consolidated talus, and perhaps glacier ice [*Cashman et al.*, 2009; *Pallister et al.*, 2009; *Schilling et al.*, 2009; *Vallance et al.*, 2009], and so were likely to be acoustically permeable for infrasonic wavelengths. Slow diffusion, condensation, and buffering of steam through this material may result in relatively low levels of steam emissions at the surface, consistent with field observations. Darcy's law for fluid flow through a porous medium gives an approximate diffusion timescale for the steam:

$$\tau_d \sim \frac{\mu d^2}{\kappa \Delta P}, \tag{10}$$

where μ is the dynamic viscosity of steam, d the depth of the venting hydrothermal crack, κ the permeability of dome rock, and ΔP the pressure difference between the crack and the surface. For $\mu \sim 10^{-5}$ kg/ms, $d \sim 200$ m, $\kappa \sim 9 \times 10^{-13}$ m^2 corresponding to vesicular dacite at MSH [*Cashman et al.*, 2009], and ΔP given by lithostatic pressure ~5 MPa ($\Delta P \sim \rho g z$ for $\rho = 2650$ kg/m^3, $g = 9.8$ m/s^2, and $z = 200$ m), τ_d is ~24 h, providing adequate time for a periodic release of steam to be filtered to a steady surface effusion, and perhaps for a large portion of the steam to be condensed and buffered. Even if the flow of steam takes place through a dendritic network of cracks with values of effective permeability κ more than an order of magnitude higher, the requirement for τ_d to be more than tens of minutes could be satisfied, masking the periodic nature of the steam release and providing time for condensation.

[77] Finally, we note that the weak long-duration signal underlying the dominant pulse in the infrasonic records was identified only by waveform cross correlation of many repeating events (Figure 9) and was too low in amplitude to be identified in individual events by array processing. This energy has a P/V_z ratio an order of magnitude or more lower than the main pulse, so is consistent with seismic-acoustic converted energy from the region around the source as calculated in our numerical models. This agrees with our interpretation that crack waves coupling into the elastic solid and subsequently into the atmosphere at the ground surface form much weaker infrasonic signals than direct mass injection through clogged pathways to the atmosphere.

[78] The LP seismic events investigated in this study have alternatively been attributed to stick-slip motion and shear fracture of the extruding solid lava dome [e.g., *Iverson et al.*, 2006; *Harrington and Brodsky*, 2007; *Tuffen et al.*, 2008]. This shear-faulting source process was qualitatively suggested by the presence of fault gouge and breccia on the surface of the extruded lava spines [*Pallister et al.*, 2009], but these features may be generated aseismically. A shear-faulting (double-couple) source is inconsistent with the

all-dilatational first motions and volumetric source mechanism derived by *Waite et al.* [2008]. We note that although the drumbeat LP events at MSH have been classified as "hybrid" LP events on the basis of their broadband onsets [*Iverson et al.*, 2006; *Harrington and Brodsky*, 2007] (see Figure 5d), a hybrid LP event was originally defined as an event with resonance features characteristic of an LP event, but with mixed first motions characteristic of a double-couple (shear-faulting) source [*Lahr et al.*, 1994]. Since the MSH drumbeat events do not have mixed first motions, they are not hybrid events according to the definition of *Lahr et al.* [1994]. The observed broadband onsets of the MSH LP events are typical of LPs, and correspond to the higher modes of oscillation of a resonating source (see Figure 20), which dissipate more rapidly than the lower modes (leading to the long-period coda).

[79] Furthermore, a shear-faulting source mechanism predicts seismic moments and single forces that are much smaller than those observed. *Waite et al.* [2008] presented inversion results for a series of similar waveform LP events with estimated forces up to 8×10^9 N and moments up to 2×10^{13} N m. These values are 2–3 orders of magnitude larger than the force of $\sim 7 \times 10^7$ N (for slip of 5 mm) estimated by *Iverson et al.* [2006] and moments of 10^9–10^{10} N m estimated directly from fault surfaces on the lava spines [*Pallister et al.*, 2008]. A shear-faulting source is also difficult to reconcile with the results of this study. In principle, a shear-faulting source may generate infrasound by gas release associated with the rupture of gas-charged lava dome material [*Yamasato*, 1998], and it has also been proposed that gas-filled cracks resulting from fracture of silicic magma may sustain seismic LP resonance [*Tuffen and Dingwell*, 2005]. However, the gas-poor nature of the 2004–2008 MSH extrusion [*Gerlach et al.*, 2009] makes these scenarios implausible for MSH. A passive release of gas in response to shear fracture would also generate a much weaker infrasonic signal than the infrasonic source mechanism outlined above. The presence of steaming cracks in the 2004–2008 lava dome [*Vallance et al.*, 2009], as well as geoelectrical evidence for the presence and persistence of an active shallow hydrothermal system within ~200 m of the 1980s crater floor throughout the 2004–2008 MSH eruption [*Bedrosian et al.*, 2007, 2008], provide additional qualitative yet compelling evidence in favor of a shallow hydrothermal origin for the source of seismic and infrasonic LP events at MSH.

7.2. Signal Intermittency

[80] The infrasound signals accompanying LP events at Mount St. Helens are among the lowest-amplitude acoustic signals recorded from volcanoes at this range. Typical amplitudes were ~0.01 Pa at 13.4 km (Figure 4), which is 2 orders of magnitude lower than signals from phreatic explosive events and rockfalls (~1 Pa) recorded at the same array from Mount St. Helens [*Matoza et al.*, 2007; *Moran et al.*, 2008], and 3 orders of magnitude lower than signals recorded at the more open-vent system at Tungurahua volcano, Ecuador, at a greater range of 37 km (D. Fee et al., Characterization of explosion signals from Tungurahua volcano, paper presented at 2007 Infrasound Technology Workshop, Japan Weather Association, Tokyo, Japan, 13–16 November 2007). Therefore, it is not surprising that clear detection above noise of these signals depends on atmospheric propagation effects.

[81] Ray tracing for reasonable atmospheric specifications provided by G2S predicted strong variability in signal detection as a function of wind, and to a lesser extent, temperature gradients. However, the ray predictions do not agree with the more complete description of wave propagation given by finite differences. For vertical wind and temperature gradients where rays show sharp refraction and the formation of a shadow zone, finite difference results exhibit only gradual refraction, and significant diffraction of energy into ray shadow zones. The slow refraction in some instances (Figure 24d) may be enough to cause low-amplitude signals to fall below background noise levels, indicating that wind provides a viable mechanism for causing the observed intermittency in infrasonic LP signal detection. We note that the finite difference results are in agreement with predictions from normal mode theory, where frequencies of 1–5 Hz propagate as a single horizontally propagating "surface" mode for typical boundary layer wind and temperature gradients [*Waxler et al.*, 2006, 2008].

[82] The decorrelation, loss, and subsequent return of the same infrasonic waveform is a strong indicator of atmospheric effects. Furthermore, these changes in waveform appear to be correlated with measured changes in wind speed and direction at particular times (Figure 8). In addition, the observations of *Fee and Garcés* [2007] demonstrate propagation effects on the amplitude of weak (~0.01 Pa) infrasonic signals at ~13 km range. While the amplitude variation at Mount St. Helens is not dominantly diurnal, this suggests that mesoscale wind structure has an important effect on infrasonic propagation at these ranges.

[83] This said, atmospheric dynamics are clearly not the only cause of signal intermittency. Infrasonic detections are more likely when the amplitude at the source is higher (Figure 7), illustrating that clear signal reception requires a minimum amplitude at the source even under favorable atmospheric conditions. Hence, the signal intermittency is a superposition of a long-term trend associated with the changing source amplitude, and short-term variability due to atmospheric effects.

[84] Finally, we comment that the source process outlined in section 7.1 could in principle produce another source of signal intermittency via changes in the permeability of the materials overlying the LP source [*Matoza et al.*, 2007]. However, changes of this kind would be masked by the effects discussed above, and we do not have adequate data to examine this.

8. Conclusions

[85] During November 2004 to March 2005, the source process for a sustained sequence of repetitive seismic LP events at Mount St. Helens (drumbeats) also generated impulsive broadband pressure signals traveling through the atmosphere at acoustic velocity. Finite difference simulation of the seismo-acoustic wavefield indicates that the infrasonic signals could not result simply from seismic-acoustic coupling from a common source time function. The seismic LP event is typically modeled as an impulsive broadband pressure excitation mechanism followed by a

long-duration coda resulting from the resonant response of a fluid-filled cavity. The infrasonic signal associated with the LP may be considered a record of the broadband pressure excitation mechanism or trigger mechanism initiating the resonance, while the resonant component couples only weakly through the elastic solid to the overlying atmosphere. The preferential coupling of the trigger component to the atmosphere is consistent with periodic pressure release from a shallow buried hydrothermal crack into a near-surface layer of highly fractured dome rock, and loosely consolidated talus and glacier ice. If the crack is very shallow, variations in crater topography above the crack may also enhance the preferential coupling of the trigger component into the atmosphere. Pressure may build in a sealed hydrothermal crack due to heating from magmatic activity. Periodically, pressure in the crack exceeds the containment pressure, leading to the sudden opening of a "valve," the production of the impulsive infrasonic signal, and the venting of steam through a network of cracks in the near-surface permeable material. Such a porous, highly permeable layer may permit transmission of the infrasonic pressure signals while filtering a periodic steam release to a steady surface effusion. Meanwhile, the sudden loss of pressure in the crack causes the crack to collapse, and initiates resonance of the remaining fluid, generating the seismic LP event. After pressure is lost, lithostatic pressure may reseal the valve, closing a cycle of pressure recharge and collapse that may be responsible for the periodic occurrence of drumbeat LPs.

[86] Since the infrasonic signals were of relatively low amplitude, they were detected intermittently at an array 13.4 km to the NW of the volcano. We attribute the intermittency primarily to changes in amplitude at the source and time-varying atmospheric propagation effects. Waveform cross correlation and preliminary modeling using ray tracing and finite differences suggest that wind in the atmospheric boundary layer is the dominating atmospheric factor. However, more detailed information on the mesoscale meteorological structure is required to better understand the causes of amplitude spread and subtle waveform variability.

[87] **Acknowledgments.** Data for CDWR were collected by the Acoustic Surveillance for Hazardous Eruptions (ASHE) project [*McCormack et al.*, 2005]. CVO data were provided by Seth Moran, Wes Thelen, and IRIS. Thanks to Bob Parker for PSD, Steve Schilling for the DEM, Garth Ferber for the NWAC met data, Doug Drob for the G2S model, and Larry Baker for help with WETC3D. Documentation and publication of ASTAROTH is currently in preparation by LD. Cluster access was kindly provided by Debi Kilb and Atul Nayak (NSF grant ANI-0225642 and the ANF), as well as Sofia Akber and Steve Constable. RSM would like to thank Hank Bass, David Fee, David Green, Seth Moran, Jim Sabatier, and Roger Waxler for enlightening discussions. The manuscript was diligently reviewed by Seth Moran and John Power (USGS), and two anonymous referees. This work was funded by NSF grant EAR-0609669.

References

Bass, H. E. (1991), Atmospheric acoustics, in *Encyclopedia of Applied Physics*, vol. 2, pp. 145–179, VCH, New York.

Bass, H. E., L. N. Bolen, D. Cress, J. Lundien, and M. Flohr (1980), Coupling of airborne sound into the Earth: Frequency dependence, *J. Acoust. Soc. Am.*, *67*, 1502–1506, doi:10.1121/1.384312.

Bedrosian, P. A., M. J. Unsworth, and M. J. S. Johnston (2007), Hydrothermal circulation at Mount St. Helens determined by self-potential measurements, *J. Volcanol. Geotherm. Res.*, *160*, 137–146, doi:10.1016/j.jvolgeores.2006.09.003.

Bedrosian, P. A., M. Burgess, and A. Hotovec (2008), Groundwater Hydrology within the crater of Mount St. Helens from geophysical constraints, *Eos Trans. AGU*, *89*(53), Fall Meet. Suppl., Abstract V43E-2191.

Benioff, H., M. Ewing, and F. Press (1951), Sound waves in the atmosphere generated by a small earthquake, *Proc. Natl. Acad. Sci. U. S. A.*, *37*, 600–603.

Benz, H. M., B. A. Chouet, P. B. Dawson, J. C. Lahr, R. A. Page, and J. A. Hole (1996), Three-dimensional *P* and *S* wave velocity structure of Redoubt Volcano, Alaska, *J. Geophys. Res.*, *101*, 8111–8128, doi:10.1029/95JB03046.

Berenger, J. P. (1996), Three-dimensional perfectly matched layer for the absorption of electromagnetic waves, *J. Comput. Phys.*, *127*, 363–379, doi:10.1006/jcph.1996.0181.

Bolt, B. A. (1964), Seismic air waves from the great 1964 Alaskan earthquake, *Nature*, *202*, 1095–1096, doi:10.1038/2021095a0.

Brekhovskikh, L. M. (1980), *Waves in Layered Media*, 2nd ed., Academic, New York.

Cansi, Y. (1995), An automatic seismic event processing for detection and location: The P. M. C. C. method, *Geophys. Res. Lett.*, *22*, 1021–1024, doi:10.1029/95GL00468.

Caplan-Auerbach, J., and T. Petersen (2005), Repeating coupled earthquakes at Shishaldin Volcano, Alaska, *J. Volcanol. Geotherm. Res.*, *145*, 151–172, doi:10.1016/j.jvolgeores.2005.01.011.

Cashman, K. V., C. R. Thornber, and J. S. Pallister (2009), From dome to dust: Shallow crystallization and fragmentation of conduit magma during the 2004–2006 dome extrusion at Mount St. Helens, Washington, in *A Volcano Rekindled: The First Year of Renewed Eruptions at Mount St. Helens, 2004–2006*, edited by D. R. Sherrod, W. E. Scott, and P. H. Stauffer, *U.S. Geol. Surv. Prof. Pap.*, *1750*, in press.

Chouet, B. (1985), Excitation of a buried magmatic pipe: A seismic source model for volcanic tremor, *J. Geophys. Res.*, *90*, 1881–1893, doi:10.1029/JB090iB02p01881.

Chouet, B. (1986), Dynamics of a fluid-driven crack in three dimensions by the finite-difference method, *J. Geophys. Res.*, *91*, 13,967–13,992, doi:10.1029/JB091iB14p13967.

Chouet, B. (1988), Resonance of a fluid-driven crack: Radiation properties and implications for the source of long-period events and harmonic tremor, *J. Geophys. Res.*, *93*, 4375–4400, doi:10.1029/JB093iB05p04375.

Chouet, B. (1992), A seismic model for the source of long-period events and harmonic tremor, in *Volcanic Seismology*, edited by P. Gasparini, R. Scarpa, and K. Aki, *IAVCEI Proc. Volcanol.*, *3*, 133–156.

Chouet, B. A. (1996a), Long-period volcano seismicity: Its source and use in eruption forecasting, *Nature*, *380*, 309–316, doi:10.1038/380309a0.

Chouet, B. A. (1996b), New methods and future trends in seismological volcano monitoring, in *Monitoring and Mitigation of Volcano Hazards*, edited by R. Scarpa and R. Tilling, pp. 23–97, Springer, New York.

Chouet, B. (2003), Volcano seismology, *Pure Appl. Geophys.*, *160*, 739–788, doi:10.1007/PL00012556.

Chouet, B., P. Dawson, T. Ohminato, M. Martini, G. Saccorotti, F. Giudicepietro, G. De Luca, G. Milana, and R. Scarpa (2003), Source mechanisms of explosions at Stromboli Volcano, Italy, determined from moment-tensor inversions of very-long-period data, *J. Geophys. Res.*, *108*(B1), 2019, doi:10.1029/2002JB001919.

Chouet, B., P. Dawson, and A. Arciniega-Ceballos (2005), Source mechanism of Vulcanian degassing at Popocatépetl Volcano, Mexico, determined from waveform inversions of very long period signals, *J. Geophys. Res.*, *110*, B07301, doi:10.1029/2004JB003524.

D'Auria, L., and M. Martini (2007), 3-D finite difference modeling of the seismo-acoustic wave field, *Seismol. Res. Lett.*, *59*(2), 245.

DeFatta, D. J., J. G. Lucas, and W. S. Hodgkiss (1988), *Digital Signal Processing: A System Design Approach*, John Wiley, New York.

de Groot-Hedlin, C. (2004), Criteria for discretization of seafloor bathymetry when using a stairstep approximation: Application to computation of T-phase seismograms, *J. Acoust. Soc. Am.*, *115*, 1103–1113, doi:10.1121/1.1643361.

Drob, D. P., J. M. Picone, and M. Garcés (2003), Global morphology of infrasound propagation, *J. Geophys. Res.*, *108*(D21), 4680, doi:10.1029/2002JD003307.

Embleton, T. F. W. (1996), Tutorial on sound propagation outdoors, *J. Acoust. Soc. Am.*, *100*, 31–48, doi:10.1121/1.415879.

Fee, D., and M. Garcés (2007), Infrasonic tremor in the diffraction zone, *Geophys. Res. Lett.*, *34*, L16826, doi:10.1029/2007GL030616.

Ferrazzini, V., and K. Aki (1987), Slow waves trapped in a fluid-filled infinite crack: Implication for volcanic tremor, *J. Geophys. Res.*, *92*, 9215–9223, doi:10.1029/JB092iB09p09215.

Festa, G., and S. Nielsen (2003), PML absorbing boundaries, *Bull. Seismol. Soc. Am.*, *93*, 891–903, doi:10.1785/0120020098.

Garcés, M. (1997), On the volcanic waveguide, *J. Geophys. Res.*, *102*, 22,547–22,564, doi:10.1029/97JB01799.

Garcés, M. A., R. A. Hansen, and K. G. Lindquist (1998), Traveltimes for infrasonic waves propagating in a stratified atmosphere, *Geophys. J. Int.*, *135*, 255–263, doi:10.1046/j.1365-246X.1998.00618.x.

Garcés, M., M. Iguchi, K. Ishihara, M. Morrissey, Y. Sudo, and T. Tsutsui (1999), Infrasonic precursors to a Vulcanian eruption at Sakurajima Volcano, Japan, *Geophys. Res. Lett.*, *26*, 2537–2540, doi:10.1029/1998GL005327.

Garcés, M., D. Fee, D. McCormack, R. Servranckx, H. Bass, C. Hetzer, M. Hedlin, R. Matoza, and H. Yepes (2008), Prototype ASHE volcano monitoring system captures the acoustic fingerprint of stratospheric ash injection, *Eos Trans. AGU*, *89*, 377.

Gerlach, T. M., K. A. McGee, and M. P. Doukas (2009), Emission rates of CO_2, SO_2, and H_2S, scrubbing, and preeruption excess volatiles at Mount St. Helens, 2004–2005, in *A Volcano Rekindled: The First Year of Renewed Eruptions at Mount St. Helens, 2004–2006*, edited by D. R. Sherrod, W. E. Scott, and P. H. Stauffer, *U.S. Geol. Surv. Prof. Pap.*, *1750*, in press.

Gil Cruz, F., and B. A. Chouet (1997), Long-period events, the most characteristic seismicity accompanying the emplacement and extrusion of a lava dome in Galeras Volcano, Colombia, in 1991, *J. Volcanol. Geotherm. Res.*, *77*, 121–158, doi:10.1016/S0377-0273(96)00091-1.

Graves, R. W. (1996), Simulating seismic wave propagation in 3D elastic media using staggered-grid finite-differences, *Bull. Seismol. Soc. Am.*, *86*, 1091–1106.

Green, D. N., and J. Neuberg (2006), Waveform classification of volcanic low-frequency earthquake swarms and its implication at Soufriere Hills Volcano, Montserrat, *J. Volcanol. Geotherm. Res.*, *153*, 51–63, doi:10.1016/j.jvolgeores.2005.08.003.

Harrington, R. M., and E. E. Brodsky (2007), Volcanic hybrid earthquakes that are brittle-failure events, *Geophys. Res. Lett.*, *34*, L06308, doi:10.1029/2006GL028714.

Hedlin, M. A. H., B. Alcoverro, and G. D'Spain (2003), Evaluation of rosette infrasonic noise-reducing spatial filters, *J. Acoust. Soc. Am.*, *114*, 1807–1820, doi:10.1121/1.1603763.

Hickey, C. J., and J. M. Sabatier (1997), Measurements of two types of dilatational waves in an air-filled unconsolidated sand, *J. Acoust. Soc. Am.*, *102*, 128–136, doi:10.1121/1.419770.

Iguchi, M., and K. Ishihara (1990), Comparison of earthquakes and airshocks accompanied with explosive eruptions at Sakurajima and Suwanosejima volcanoes (in Japanese), *Annu. Disas. Prev. Res. Inst. Kyoto Univ.*, *33B-1*, 1–11.

Iverson, R. M., et al. (2006), Dynamics of seismogenic volcanic extrusion at Mount St. Helens in 2004–05, *Nature*, *444*, 439–443, doi:10.1038/nature05322.

Kitov, I. O., J. R. Murphy, O. P. Kusnetsov, B. W. Barker, and N. I. Nedoshivin (1997), An analysis of seismic and acoustic signals measured from a series of atmospheric and near-surface explosions, *Bull. Seismol. Soc. Am.*, *87*, 1553–1562.

Kumagai, H., and B. A. Chouet (2000), Acoustic properties of a crack containing magmatic or hydrothermal fluids, *J. Geophys. Res.*, *105*, 25,493–25,512, doi:10.1029/2000JB900273.

Kumagai, H., B. A. Chouet, and P. B. Dawson (2005), Source process of a long-period event at Kilauea volcano, Hawaii, *Geophys. J. Int.*, *161*, 243–254, doi:10.1111/j.1365-246X.2005.02502.x.

Lahr, J. C., B. A. Chouet, C. D. Stephens, J. A. Power, and R. A. Page (1994), Earthquake classification, location, and error analysis in a volcanic environment: Implications for the magmatic system of the 1989–1990 eruptions of Redoubt Volcano, Alaska, *J. Volcanol. Geotherm. Res.*, *62*, 137–151, doi:10.1016/0377-0273(94)90031-0.

Landau, L. D., and E. M. Lifshitz (1987), *Fluid Mechanics*, 2nd ed., Pergamon, New York.

Larsson, C., and S. Israelsson (1991), Effects of meteorological conditions and source height on sound propagation near the ground, *Appl. Acoust.*, *33*, 109–121, doi:10.1016/0003-682X(91)90068-P.

Leet, R. C. (1988), Saturated and subcooled hydrothermal boiling in groundwater-flow channels as a source of harmonic tremor, *J. Geophys. Res.*, *93*, 4835–4849, doi:10.1029/JB093iB05p04835.

Leighton, T. G. (1994), *The Acoustic Bubble*, Academic, New York.

Le Pichon, A., J. Guilbert, A. Vega, M. Garcés, and N. Brachet (2002), Ground-coupled air waves and diffracted infrasound from the Arequipa earthquake of June 23, 2001, *Geophys. Res. Lett.*, *29*(18), 1886, doi:10.1029/2002GL015052.

Le Pichon, A., J. Guilbert, M. Vallée, J. X. Dessa, and M. Ulziibat (2003), Infrasonic imaging of the Kunlun Mountains for the great 2001 China earthquake, *Geophys. Res. Lett.*, *30*(15), 1814, doi:10.1029/2003GL017581.

Le Pichon, A., P. Mialle, J. Guilbert, and J. Vergoz (2006), Multistation infrasonic observations of the Chilean earthquake of 2005 June 13, *Geophys. J. Int.*, *167*, 838–844, doi:10.1111/j.1365-246X.2006.03190.x.

Lighthill, M. J. (2001), *Waves in Fluids*, Cambridge Univ. Press, Cambridge, U. K.

Matoza, R. S., M. A. H. Hedlin, and M. A. Garcés (2007), An infrasound array study of Mount St. Helens, *J. Volcanol. Geotherm. Res.*, *160*, 249–262, doi:10.1016/j.jvolgeores.2006.10.006.

McChesney, P. J., M. R. Couchman, S. C. Moran, A. B. Lockhart, K. J. Swinford, and R. G. La Husen (2009), Seismic monitoring changes and the remote deployment of seismic stations (Seismic Spider) at Mount St. Helens, 2004–2005, in *A Volcano Rekindled: The First Year of Renewed Eruptions at Mount St. Helens, 2004–2006*, edited by D. R. Sherrod, W. E. Scott, and P. H. Stauffer, *U.S. Geol. Surv. Prof. Pap.*, *1750*, in press.

McCormack, D., H. Bass, M. Garcés, and H. Yepes (2005), Acoustic surveillance for hazardous eruptions (ASHE), *J. Acoust. Soc. Am.*, *117*, 2419.

Mikumo, T. (1968), Atmospheric pressure waves and tectonic deformation associate with the Alaskan earthquake of March 28, 1964, *J. Geophys. Res.*, *73*, 2009–2025, doi:10.1029/JB073i006p02009.

Moran, S. C., R. S. Matoza, M. A. Garcés, M. A. H. Hedlin, D. Bowers, W. E. Scott, D. R. Sherrod, and J. W. Vallance (2008), Seismic and acoustic recordings of an unusually large rockfall at Mount St. Helens, Washington, *Geophys. Res. Lett.*, *35*, L19302, doi:10.1029/2008GL035176.

Moran, S. C., S. D. Malone, A. I. Qamar, W. Thelen, A. K. Wright, and J. Caplan-Auerback (2009a), 2004–2005 seismicity associated with the renewed dome-building eruption of Mount St. Helens, in *A Volcano Rekindled: The First Year of Renewed Eruptions at Mount St. Helens, 2004–2006*, edited by D. R. Sherrod, W. E. Scott, and P. H. Stauffer, *U.S. Geol. Surv. Prof. Pap.*, *1750*, in press.

Moran, S. C., P. J. McChesney, and A. B. Lockhart (2009b), Seismicity and Infrasound Associated with Explosions at Mount St. Helens, 2004–2005, in *A Volcano Rekindled: The First Year of Renewed Eruptions at Mount St. Helens, 2004–2006*, edited by D. R. Sherrod, W. E. Scott, and P. H. Stauffer, *U.S. Geol. Surv. Prof. Pap.*, *1750*, in press.

Mutschlecner, J. P., and R. W. Whitaker (2005), Infrasound from earthquakes, *J. Geophys. Res.*, *110*, D01108, doi:10.1029/2004JD005067.

Neuberg, J., and T. Pointer (2000), Effects of volcano topography on seismic broadband waveforms, *Geophys. J. Int.*, *143*, 239–248, doi:10.1046/j.1365-246x.2000.00251.x.

Neuberg, J., R. Luckett, B. Baptie, and K. Olsen (2000), Models of tremor and low-frequency earthquake swarms on Montserrat, *J. Volcanol. Geotherm. Res.*, *101*, 83–104, doi:10.1016/S0377-0273(00)00169-4.

Ohminato, T. (2006), Characteristics and source modeling of broadband seismic signals associated with the hydrothermal system at Satsuma-Iwojima volcano, Japan, *J. Volcanol. Geotherm. Res.*, *158*, 467–490, doi:10.1016/j.jvolgeores.2006.08.004.

Ohminato, T., and B. A. Chouet (1997), A free-surface boundary condition for including 3D topography in the finite-difference method, *Bull. Seismol. Soc. Am.*, *87*, 494–515.

Ostashev, V. E. (1997), *Acoustics in Moving Inhomogeneous Media*, E & FN SPON, London.

Pallister, J. S., K. V. Cashman, and J. T. Hagstrum (2008), Conduit-margin faulting at Mount St. Helens—A seismogenic process?, *Eos Trans. AGU*, *89*(53), Fall Meet. Suppl., Abstract V43E-2186.

Pallister, J. S., C. R. Thornber, K. V. Cashman, M. A. Clynne, H. A. Lowers, C. W. Mandeville, I. K. Brownfield, and G. P. Meeker (2009), Petrology of the 2004–2006 Mount St. Helens lava dome-implications for magmatic plumbing and eruption triggering, in *A Volcano Rekindled: The First Year of Renewed Eruptions at Mount St. Helens, 2004–2006*, edited by D. R. Sherrod, W. E. Scott, and P. H. Stauffer, *U.S. Geol. Surv. Prof. Pap.*, *1750*, in press.

Petersen, T. (2007), Swarms of repeating long-period earthquakes at Shishaldin Volcano, Alaska, 2001–2004, *J. Volcanol. Geotherm. Res.*, *166*, 177–192, doi:10.1016/j.jvolgeores.2007.07.014.

Petersen, T., and S. R. McNutt (2007), Seismo-acoustic signals associated with degassing explosions recorded at Shishaldin Volcano, Alaska, 2003–2004, *Bull. Volcanol.*, *69*, 527–536, doi:10.1007/s00445-006-0088-z.

Piercy, J. E., T. F. W. Embleton, and L. C. Sutherland (1977), Review of noise propagation in the atmosphere, *J. Acoust. Soc. Am.*, *61*, 1403–1418, doi:10.1121/1.381455.

Press, F., and M. Ewing (1951), Ground roll coupling to atmospheric compressional waves, *Geophysics*, *16*, 416–438, doi:10.1190/1.1437684.

Reynolds, O. (1873), On the refraction of sound by the atmosphere, *Proc. R. Soc. London*, *22*, 531–548, doi:10.1098/rspl.1873.0095.

Rice, J. A. (1995), *Mathematical Statistics and Data Analysis*, 2nd ed., Duxbury, Belmont, Calif.

Riedel, K. S., and A. Sidorenko (1995), Minimum bias multiple taper spectral estimation, *IEEE Trans. Signal Process.*, *43*, 188–195, doi:10.1109/78.365298.

Sabatier, J. M., and R. Raspet (1988), Investigation of possibility of damage from the acoustically coupled seismic waveform from blast and artillery, *J. Acoust. Soc. Am.*, *84*, 1478–1482, doi:10.1121/1.396593.

Sabatier, J. M., H. E. Bass, L. N. Bolen, and K. Attenborough (1986), Acoustically induced seismic waves, *J. Acoust. Soc. Am.*, *80*, 646–649, doi:10.1121/1.394058.

Scheu, B., H. Kern, O. Spieler, and D. B. Dingwell (2006), Temperature dependence of elastic P- and S-wave velocities in porous Mt. Unzen dacite, *J. Volcanol. Geotherm. Res.*, *153*, 136–147, doi:10.1016/j.jvolgeores.2005.08.007.

Schilling, S. P., R. A. Thompson, J. A. Messerich, and E. Y. Iwatsubo (2009), Use of digital aerophotogrammetry to determine rates of lava dome growth, Mount St. Helens, 2004–2005, in *A Volcano Rekindled: The First Year of Renewed Eruptions at Mount St. Helens, 2004–2006*, edited by D. R. Sherrod, W. E. Scott, and P. H. Stauffer, *U.S. Geol. Surv. Prof. Pap.*, *1750*, in press.

Stephens, C. D., and B. A. Chouet (2001), Evolution of the December 14, 1989 precursory long-period event swarm at Redoubt Volcano, Alaska, *J. Volcanol. Geotherm. Res.*, *109*, 133–148, doi:10.1016/S0377-0273(00)00308-5.

Stump, B. W. (1985), Constraints on explosive sources with spall from near-source waveforms, *Bull. Seismol. Soc. Am.*, *75*, 361–377.

Sutherland, L. C., and H. E. Bass (2004), Atmospheric absorption in the atmosphere up to 160 km, *J. Acoust. Soc. Am.*, *115*, 1012–1032, doi:10.1121/1.1631937.

Sylvander, M., C. Ponsolles, S. Benahmed, and J. F. Fels (2007), Seismoacoustic recordings of small earthquakes in the Pyrenees: Experimental results, *Bull. Seismol. Soc. Am.*, *97*, 294–304, doi:10.1785/0120060009.

Thelen, W. A., R. S. Crosson, and K. C. Creager (2009), Absolute and relative locations of earthquakes at Mount St. Helens, Washington using continuous data: Implications for magmatic processes, in *A Volcano Rekindled: The First Year of Renewed Eruptions at Mount St. Helens, 2004–2006*, edited by D. R. Sherrod, W. E. Scott, and P. H. Stauffer, *U.S. Geol. Surv. Prof. Pap.*, *1750*, in press.

Tuffen, H., and D. Dingwell (2005), Fault textures in volcanic conduits: Evidence for seismic trigger mechanisms during silicic eruptions, *Bull. Volcanol.*, *67*, 370–387, doi:10.1007/s00445-004-0383-5.

Tuffen, H., R. Smith, and P. R. Sammonds (2008), Evidence for seismogenic fracture of silicic magma, *Nature*, *453*, 511–514, doi:10.1038/nature06989.

Vallance, J. W., D. J. Schneider, and S. P. Schilling (2009), Growth of the 2004–2006 lava-dome complex at Mount St. Helens, in *A Volcano Rekindled: The First Year of Renewed Eruptions at Mount St. Helens, 2004–2006*, edited by D. R. Sherrod, W. E. Scott, and P. H. Stauffer, *U.S. Geol. Surv. Prof. Pap.*, *1750*, in press.

van Vossen, R., J. O. A. Robertsson, and C. H. Chapman (2002), Finite-difference modeling of wave propagation in a fluid-solid configuration, *Geophysics*, *67*, 618–624, doi:10.1190/1.1468623.

Viktorov, I. A. (1967), *Rayleigh and Lamb Waves: Physical Theory and Applications*, Plenum, New York.

Virieux, J. (1986), *P-SV* wave propagation in heterogeneous media: Velocity-stress finite-difference method, *Geophysics*, *51*, 889–901, doi:10.1190/1.1442147.

Waite, G. P., and S. C. Moran (2006), Crustal *P* wave speed structure under Mount St. Helens from local earthquake tomography, *Eos Trans. AGU*, *87*, Fall Meet. Suppl., Abstract V11B-0578.

Waite, G. P., B. A. Chouet, and P. B. Dawson (2008), Eruption dynamics at Mount St. Helens imaged from broadband seismic waveforms: Interaction of the shallow magmatic and hydrothermal systems, *J. Geophys. Res.*, *113*, B02305, doi:10.1029/2007JB005259.

Waxler, R., C. L. Talmadge, S. Dravida, and K. E. Gilbert (2006), The near-ground structure of the nocturnal sound field, *J. Acoust. Soc. Am.*, *119*, 86–95, doi:10.1121/1.2139654.

Waxler, R., K. E. Gilbert, and C. L. Talmadge (2008), A theoretical treatment of the long range propagation of impulsive signals under strongly ducted nocturnal conditions, *J. Acoust. Soc. Am.*, *124*, 2742–2754, doi:10.1121/1.2980520.

Yamasato, H. (1998), Nature of infrasonic pulse accompanying low frequency earthquake at Unzen Volcano, Japan, *Bull. Volcanol. Soc. Jpn.*, *43*, 1–13.

Yamasato, H., J. Miyamura, H. Mori, Y. Usui, K. Sakuma, A. Watanabe, J. Sato, Y. Takahashi, and T. Sakai (2002), Eruptive activity inferred from infrasound associated with the 2000 eruption of Usu Volcano (in Japanese, English abstract), *Bull. Volcanol. Soc. Jpn.*, *47*, 255–262.

B. A. Chouet, U.S. Geological Survey, 345 Middlefield Road, MS 910, Menlo Park, CA 94025, USA.

L. D'Auria, Istituto Nazionale di Geofisica e Vulcanologia, Osservatorio Vesuviano, Via Diocleziano, 328, I-80124 Naples, Italy.

C. De Groot-Hedlin, M. A. H. Hedlin, and R. S. Matoza, Laboratory for Atmospheric Acoustics, Institute of Geophysics and Planetary Physics, Scripps Institution of Oceanography, University of California, San Diego IGPP 0225, La Jolla, CA 92093-0225, USA. (rmatoza@ucsd.edu)

M. A. Garcés, Infrasound Laboratory, Hawai'i Institute of Geophysics and Planetology, University of Hawai'i at Manoa, Kailua-Kona, HI 96740-2638, USA.

G. P. Waite, Department of Geological and Mining Engineering and Sciences, Michigan Technological University, 1400 Townsend Drive, Houghton, MI 49931-0000, USA.